Characterization of a Laser Doping Process for Crystalline Silicon Solar Cells

Von der Fakultät Informatik, Elektrotechnik und Informationstechnik der
Universität Stuttgart zur Erlangung der Würde eines Doktor-Ingenieurs (Dr.Ing.)
genehmigte Abhandlung

Vorgelegt von

Mawuli Francis Ametowobla

Geboren am 20. April 1978 in Lahn-Gießen

Hauptberichter: Prof. Dr. rer. nat. habil. Jürgen H. Werner
Mitberichter: Prof. Dr.-Ing. Joachim Burghartz

Tag der mündlichen Prüfung: 09.06.2010

Institut für Physikalische Elektronik der Universität Stuttgart
2010

Contents

Abstract

This thesis characterizes a process for the laser based formation of highly doped layers on crystalline silicon, which was developed at Institut für Physikalische Elektronik (*ipe*), University of Stuttgart. A first step analyzes silicon, which is laser irradiated without being doped at the same time. This approach allows for separating the effects of the laser process itself from the influence of employed doping precursors. The irradiation leads to a significant reduction of the minority carrier lifetime in the processed silicon. A thorough characterization of suchlike treated samples shows the incorporation of the impurities oxygen, carbon and nitrogen, up to concentration levels of $C \approx 10^{19}$ cm^{-3}. At the same time, an n-type doping occurs within the irradiated surface layers. The doping concentrations are in the range $N_D \approx 10^{17}$ cm^{-3}. In spite of the numerously employed characterization methods, a complete identification of the mechanism, which causes the lifetime reduction, is not achieved. However, there exists the strong indication that the incorporated impurities, which lead to the n-type doping, are at the same time responsible for the lifetime degradation. Due to the low thickness $d < 500$ nm of the laser melted layers, defect induced local lifetimes $\tau_{SRH} < 10$ ns are required to explain the measured effective lifetimes.

The examination of laser irradiated high efficiency n-type emitters on p-type silicon substrates, the emitters being pre-fabricated by phosphorous furnace diffusion, yields information about the lifetime τ_{SRH} of laser induced defects inside the emitters. The values found for τ_{SRH} are in the range of 3 ns $< \tau_{SRH} <$ 7 ns. These values are in accordance to the results found for irradiated, undiffused samples. The use of optimized laser parameters allows for obtaining very low emitter saturation current densities $J_{0e} \approx 45$ fAcm^{-2} after the irradiation. An experimental overview over various liquid and sputtered phosphorous precursors reveals strongly differing J_{0e} values of samples, fabricated with different precursors. Considering the laser induced defects allows for predicting the potential for J_{0e} and the open circuit voltage V_{oc} of solar cells, fabricated with the best precursor, to $J_{0e} < 100$ fAcm^{-2} and $V_{oc} \approx 680$ mV. This prediction points out that in the vast majority of cases, the defects, induced by the laser treatment itself, do not limit the performance of emitters, fabricated with the *ipe* process. Solar cells, which were produced in the course of this work, exhibit significantly lower open circuit voltages of maximum $V_{oc} \approx 635$ mV. In addition, these cells often exhibit low fill factors $FF < 70$ % and efficiencies $\eta < 15$ %. However, this lower performance is not in contrast to the predicted V_{oc} potential. An analysis shows that mainly technological problems, leading to doping inhomogeneities, cause the lower efficiencies.

An additional characterization of aluminium as a precursor material for p-type emitters on n-type silicon substrates shows exceptionally high doping concentrations $N_D > 10^{21}$ cm^{-3}. Corresponding emitter saturation current densities reach extremely high values of $J_{0e} > 10^{-11}$ Acm^{-2}. Consequently, the open circuit voltage V_{oc} of solar cells, fabricated with aluminium doped emitters, is limited to $V_{oc} \approx 550$ mV and their efficiency to $\eta \approx 7$ %.

Zusammenfassung

Die vorliegende Arbeit untersucht einen am Institut für Physikalische Elektronik (*ipe*), Universität Stuttgart, entwickelten Prozess zur lasergestützen Erzeugung hoch dotierter Schichten auf kristallinem Silizium. Um die Einflüsse des Prozesses als solchem von denen der dabei eingesetzten Dotierstoffe zu trennen, erfolgt in einem ersten Schritt die Untersuchung von laserbestrahltem Silizium, ohne gleichzeitige Dotierung. Es stellt sich heraus, dass die Laserbestrahlung an sich zu einer deutlichen Reduktion der Minoritätsladungsträgerlebensdauer im prozessierten Silizium führt. Eine ausführliche Charakterisierung von derart behandelten Proben zeigt den Einbau der Fremdatome Sauerstoff, Kohlenstoff und Stickstoff, mit Konzentrationen bis zu $C = 10^{19}$ cm^{-3}. Es tritt eine laserinduzierte n-Typ Dotierung innerhalb der bestrahlten Oberflächenschichten auf, mit Dotierkonzentrationen bis zu $N_D \approx 10^{17}$ cm^{-3}. Trotz der Vielzahl der eingesetzten Analysemethoden gelingt die Identifikation des für den Lebensdauerrückgang verantwortlichen Mechanismus nicht vollständig. Es besteht jedoch die begründete Vermutung, dass die eingebrachten Verunreinigungen, welche die n-Typ Dotierung hervorrufen, gleichzeitig die Ursache für den Lebensdauerrückgang sind. Aufgrund der geringen Dicke $d < 500$ nm der durch den Laser aufgeschmolzenen Schichten, sind defektinduzierte lokale Lebensdauern $\tau_{SRH} < 10$ ns innerhalb dieser Schichten notwendig, um die gemessenen effektiven Lebensdauern zu erklären.

Die Charakterisierung von zuvor ofendiffundierten n-Typ Hocheffizienzemittern auf p-Typ Substraten, welche zusätzlich mit dem Laser bestrahlt wurden, ergibt Werte für die Lebensdauer τ_{SRH} laserinduzierter Defekte innerhalb der Emitter. Die ermittelten Werte liegen im Bereich von 3 ns $< \tau_{SRH} <$ 7 ns, ähnlich den laserbestrahlten, undiffundierten Proben. Die Verwendung optimierter Laserparameter erlaubt es, sehr geringe Emittersättigungsstromdichten $J_{0e} \approx 45$ fAcm^{-2} nach der Bestrahlung zu erreichen. Ein experimenteller Überblick über unterschiedliche flüssige und gesputterte Phosphor-Dotierstoffe stellt für die unterschiedlichen Phos-

phorquellen deutliche Unterschiede in den resultierenden Werten für J_{0e} heraus. Für J_{0e} und die Leerlaufspannung von Solarzellen, welche mit dem besten Prekursor hergestellt werden, lässt sich, unter Berücksichtigung der laserinduzierten Defekte, ein Potential von $J_{0e} < 100$ fAcm^{-2} und $V_{oc} \approx 680$ mV vorhersagen. Daraus folgt, dass in der großen Mehrzahl der Fälle laserinduzierte Defekte die Leistungsfähigkeit von mit dem *ipe*-Verfahren laserdotierten Emittern nicht begrenzen. Solarzellen, welche im Verlauf der Arbeit mit den unterschiedlichen Prekursoren hergestellt wurden, weisen deutlich schlechtere Leerlaufspannungen von maximal $V_{oc} \approx 635$ mV auf. Zusätzlich erreichen sie meistens nur geringe Füllfaktoren von $FF < 70$ % und Effizienzen von $\eta < 15$ %. Diese schlechten Leistungswerte stehen jedoch nicht im Widerspruch zum vorhergesagten V_{oc} Potential. Eine Analyse stellt nämlich heraus, dass hauptsächlich technologisch bedingte Dotierinhomogenitäten für die geringeren Wirkungsgrade verantwortlich sind.

Eine zusätzlich durchgeführte Untersuchung von Aluminium als Prekursormaterial für p-Typ Emitter auf n-Typ Substraten zeigt außergewöhnlich hohe Dotierkonzentrationen von $N_A > 10^{21}$ cm^{-3}. Zugehörige Emittersättigungsstromdichten erreichen sehr hohe Werte von $J_{0e} > 10^{-11}$ Acm^{-2}. Aus diesem Grund bleiben die Leerlaufspannungen V_{oc} von ebenfalls hergestellten Solarzellen mit Aluminium dotiertem Emitter auf $V_{oc} \approx 550$ mV, sowie ihre Wirkungsgrade auf $\eta \approx 7$ % beschränkt.

Chapter 1

Introduction

1.1 Thesis Motivation

Within just a couple of years, photovoltaics has developed from an exotic niche technology to a mature industry, and there are prospects that it will begin to challenge conventional energy generation, soon. The photovoltaic (PV) market is projected to grow up to 22 GW in 2013 [1]. Although the world wide economical crisis of the year 2009 indeed has brought some of the PV manufacturers to or across the verge of insolvency, it could, on the long run, even help making photovoltaic power generation independent from subsidies earlier, by leading to a massive price drop. One of the key factors that has enabled the unmatched growth so far, were the continuous research and development efforts, that optimized production processes and increased cell efficiencies.

However, for taking the step to a self-sustaining market, another significant reduction of production costs is of paramount importance. Crystalline silicon (cSi) is still dominating the market by more than 85 %, and numerous predictions that it would be replaced by thin film photovoltaics have not come true yet. One reason for this persistence certainly is the successful implementation of mass production. Turn-key factory suppliers are now enabling even technological outsiders to invest their capital into solar cell or module factories. Still, manufacturers are in strong need of new technologies that help them raising the efficiency of their solar cells further and thereby reducing the "Euro per Watt".

One candidate for being such a new technology is a laser doping process, developed at *ipe*, allowing for the selective fabrication of solar cell emitters without the need for a high temperature diffusion step. For doing so, it uses the radiation from a pulsed, green solid state laser, instead [2]. Characteristic for this process is a special line focus, which avoids the formation of crystal defects in the suchlike produced emitter layers [3]. Although the process was initially thought of as an alternative to conventional furnace diffusion, the research at *ipe* during the time of this work, as well as the developments in the PV industry have shown, that its first area of implementation will most probably be the selective "overdoping" of pre-diffused areas on the front side of crystalline silicon solar cells [4]. This kind of structure is also the development goal of other groups, working on similar processes, like combined selective laser doping and opening of the anti reflective layer [5,6] or "Laser Chemical Processing" [7,8].

This thesis examines the formation of laser induced defects and their impact on the performance of solar cell emitters fabricated with this process. In doing so, it helps to disperse doubts regarding the general applicability of the process for the solar cell production. Furthermore, it lays open the factors that influence the recombination inside laser doped emitter layers and predicts their maximum achievable performance. In addition to that, it gives an overview about the suitability of various precursor materials for the use in laser doping.

1.2 Thesis outline

Chapter 2 gives an overview about the most important properties of silicon, as well as the fundamentals of charge carrier recombination in the material. It lays the theoretical basis for the experimental characterization of important parameters and introduces an analytical approach to model emitters, containing defects. Furthermore it presents the most important basic information about cSi solar cells. The chapter concludes with a short glance at laser technology and optics.

Chapter 3 gives a short introduction to some of the most important characterization methods used in this thesis, and provides reference for further study. Among these methods, the lifetime measurement technique "Quasi Steady State Photoconductive Decay" is presented with more detail.

Chapter 4 presents the state of research regarding laser doping and points out the most important associated physical phenomena. It describes the laser processing setup at *ipe*, which was used during this thesis and elaborates on the characterization of the laser focus. Finally, it discusses some of the problems of the technology.

Chapter 5 gives an overview about different, liquid and sputtered phosphorous precursor materials for the formation of n-type emitters, as well as aluminium for the formation of p-type doped layers. It presents sheet resistance data and doping profiles, as well as measurement results from solar cells, fabricated with these precursors.

Chapter 6 dedicates itself to the thorough analysis of the laser induced reduction of the effective minority carrier lifetime in virgin silicon. It presents results from Secondary Ion Mass Spectrometry (SIMS), Electrochemical Capacitance Voltage (ECV), defect etching, Fourier Transformed Infrared Spectroscopy (FTIR), Photoluminescence (PL) and X-Ray Topography (XT) analysis and assesses different mechanisms for impurity incorporation into silicon.

Chapter 7 analyzes the impact of laser irradiation on high efficiency furnace diffused n-type emitters. An optimization of laser parameters allows for obtaining low emitter saturation current densities $J_{0e} \approx 45$ fAcm^{-2} after irradiation, compared to reference values of $J_{0e} = 25$ fAcm^{-2}. It further compares the saturation current densities of laser doped emitters with the phosphorous precursor materials introduced in Chapter 5. The J_{0e}-values found in this comparison differentiate strongly, depending on the type of employed precursor. The results for J_{0e} are linked to quantum efficiency measurements of corresponding solar cells. Furthermore, the chapter assesses the optimum emitter profile in the presence of defects and predicts the maximum open circuit voltage for laser doped solar cells to $V_{oc} \approx 680$ mV. In addition, it characterizes p-type emitters fabricated with an aluminium precursor and shows that they are limiting the efficiency of corresponding solar cells to $\eta \approx 7$ %, due to very high $J_{0e} > 10^{-11}$ Acm^{-2}.

Chapter 8 concludes this thesis with a short summary and an outlook on the potentials of the *ipe* laser doping process.

Chapter 2

Theory

2.1 Silicon

2.1.1 Electronical Properties

The electronical properties of silicon have been studied for decades, and virtually all characteristics thoroughly analyzed. Textbooks, such as e.g. Sze [9], or Green [10] give excellent reference for all values relevant to the operation of semiconductor devices and solar cells. Therefore, the well compiled information will not be repeated here, apart from an overview about a selection of special topics that are relevant to the calculations in chapters 2.2.5 and 7. These topics are the so called bandgap narrowing and the carrier mobility.

Carrier Mobility

The mobility of charge carriers depends on both temperature and dopant density, due to scattering of the charge carriers at vibrating lattice atoms and ionized impurities. The determination of a correct value of the charge carrier mobility, above all of minority carriers, has been subject of numerous studies in the last decades and has yielded values with a significant amount of scatter. A comprehensive overview of the different studies, together with the latest values can be found e.g. in Altermatt et.al. [11] who also discuss bandgap narrowing. They use a parametrization developed by Klaasen [12], which is also used by Cuevas [13], determining the (room temperature) hole minority carrier mobility μ_p in highly n-type doped silicon to

$$\mu_p = 155\ cm^2V^{-1}s^{-1} + \frac{315}{1+(N_D/10^{17})^{0.9}}\ cm^2V^{-1}s^{-1}, \tag{2.1}$$

with the doping density N_D in [cm^{-3}]. This model is also implemented in the latest version of the widespread device simulator PC1D [14] and will be used throughout this thesis. For the electron majority carrier mobility

$$\mu_n = 60 + \frac{1357}{1 + (N_D/9.64 \times 10^{16})^{0.664}} \; cm^2V^{-1}s^{-1} \tag{2.2}$$

also the PC1D model is used. For highly doped p-type silicon, a parametrization was e.g. performed by Swirhun et.al. [15].

Bandgap Narrowing

In heavily doped silicon the intrinsic carrier density n_i increases above its common value, a phenomenon referred to as bandgap narrowing (BGN). First investigations were performed by Lindholm et.al. [16], with a number of further studies following. As pointed out in Ref. [11], most of these studies actually only determined the so called "apparent bandgap narrowing" ΔE_g^{app}, which allows for modeling the heavy doping effects using Boltzmann statistics instead of the more complicated Fermi-Dirac statistics. The parametrizations for BGN are of a form

$$\Delta E_g^{app}(N_D) = K_1 ln\left(\frac{N_D}{K_2}\right) \tag{2.3}$$

with K_1 determining the slope and K_2 the onset of BGN [13]. This value in turn yields a corresponding effective intrinsic carrier density

$$n_{ie} = n_{i0} exp\left(\frac{\Delta E_g^{app}}{kT}\right) \tag{2.4}$$

with $n_{i0} = 1.0 \times 10^{10}$ cm^{-3} the intrinsic carrier density. This value of n_{i0} is widely accepted and thus used throughout this thesis in spite of a slightly different value of $n_{i0} = 9.65 \times 10^9$ cm^{-3} postulated by Altermatt et.al. [11]. Currently accepted parameters for calculating BGN are $K_1 = 14$ meV and $K_2 = 1.4 \times 10^{17}$ cm^{-3}, as published in Ref. [13].

2.1.2 Optical Properties

When light impinges on the silicon surface, it is partially reflected due to the reflectivity R_{Si}. The transmitted part penetrates into the material, where it is attenuated due to absorption. The rate of absorption is determined by the absorption law of Lambert-Beer, which characterizes the intensity

$$I(x) = (1 - R_{Si})e^{(-\alpha_{eff}x)}I_0 \tag{2.5}$$

of a light beam that has traveled a distance x inside a material with effective absorption coefficient α_{eff}, relative to an incident intensity I_0. The absorbed photons either lose their energy by generating electron/hole pairs, with a rate $G = 1/t_e$ (optical generation), t_e being the excitation time constant, or by exciting already existing carriers (Free Carrier Absorption, FCA). The excited carriers eventually thermalize and transfer their energy as heat to the lattice by carrier/lattice collisions. The optically generated electron/hole pairs eventually recombine radiatively, or likewise produce heat by non-radiative recombination, unless they are extracted out of the material in a solar cell configuration. The time constant for recombination is denoted by the carrier lifetime τ. The different recombination mechanisms will be treated in detail in the next section.

The generated heat in turn leads to the excitation of additional carriers (thermal excitation), thus inducing a kind of self coupling mechanism. The most important quantities and dependencies of the energy transfer of light to silicon will be briefly described in the following.

Absorption by optical generation of charge carriers

In semiconductors, the generation of electron/hole pairs occurs for incident photons with energies $h\nu > E_g$. The generation rate $G = I\sigma_{opt}/h\nu$, with I being the absorbed intensity, σ_{opt} the optical absorption cross section and $h\nu$ the photon energy. For silicon, the photon energies required for optical generation are $h\nu > E_g = 1.12$ eV (corresponding to $\lambda = 1107$ nm). However, silicon is an indirect band gap semiconductor, as the energy maximum of the valence band and the energy minimum of the conduction band are located at different values of crystal momentum [17]. Therefore the absorption of a photon additionally requires an interaction with the crystal lattice (phonon absorption or emission), which leads to a strong dependence of the band-to-band absorption coefficient α_0 on λ. Only for photon energies $h\nu >$ 3.4 eV ($\lambda = 365$ nm), corresponding to the direct band gap of silicon, the absorption coefficient saturates around $\alpha_0 \approx 10^6$ cm^{-1}. Figure 2.1 depicts α_0 as well as the corresponding penetration depth L_α in the range 250 nm $< \lambda <$ 1300 nm [18]. Both quantities cover a range of almost 8 orders of magnitude. For the radiation

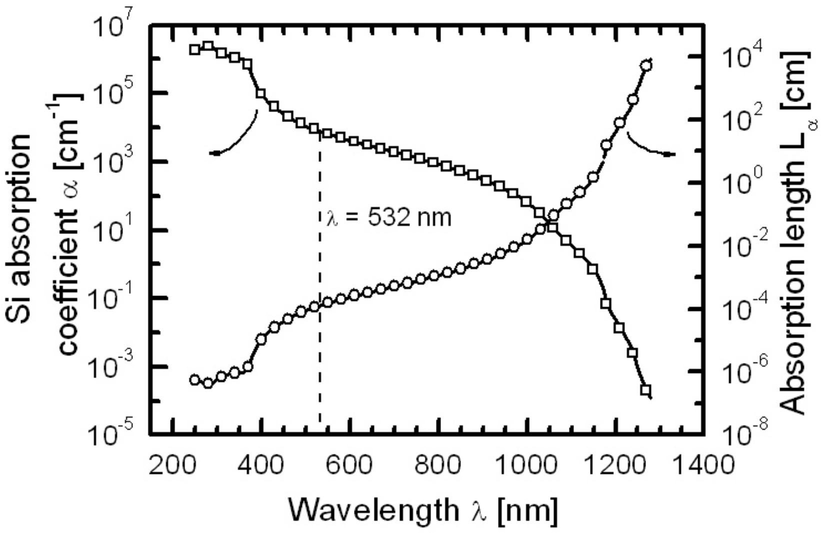

Fig. 2.1: In the wavelength regime 300 nm < λ < 1200 nm, which is relevant to silicon solar cell operation, the absorption coefficient α_0 and correspondingly the absorption length L_α of silicon strongly depend on wavelength.

of frequency-doubled solid state lasers ($\lambda = 532$ nm), as used throughout this work, the corresponding values are $\alpha_0 = 8.24 \times 10^3$ cm^{-1} and $L_\alpha = 1.2$ μm [18].

Absorption by free charge carriers

The band-to-band absorption coefficient α_0 can be significantly increased by the presence of a large number of free charge carriers N_{fcc} due to FCA. In such a case an effective absorption coefficient $\alpha_{eff} = \alpha_0 + N_{fcc}\sigma_{FC}$ holds, with σ_{FC} being the FCA cross section. As σ_{FC} increases approximately with λ^2, FCA predominantly plays a role for infrared light [19] and is therefore relatively unimportant in normal solar cell operation, being only noticeable for highly doped emitters. Relevant data is also found e.g. in Refs. [20] or [21].

Generation of free carriers. As mentioned above, free carriers are either created optically or, alternatively, by doping or heating, due to the dependence of the intrinsic carrier density n_i on the temperature according to

$$n_i\left(T\right) = \sqrt{N_C N_V} e^{(-E_g/2kT)} \tag{2.6}$$

with N_C and N_V being the effective densities of states for conduction and valence band, respectively. These quantities are in turn temperature dependent. Considering all dependencies, n_i increases exponentially with T above the so called "intrinsic temperature" T_i, which marks the temperature where the number of thermally generated carriers equals the number of carriers due to doping [22]. Figures 2.2 and 2.3 show the dependencies of α_{eff} on both temperature and doping versus the photon wavelength. With increasing temperature (Fig. 2.2) the absorption coefficient of intrinsic silicon rises for photon energies smaller than the direct band gap, and reaches values as high as $\alpha_{eff} = \alpha \approx 10^3$ cm^{-1} for $T \approx 1000$ K. Looking a the doping dependency of the absorption coefficient (Fig. 2.3) it is seen that α is greatly enhanced due to FCA for doping densities $N_D > 10^{18}$ cm^{-3}, that are typical for solar cell emitters.

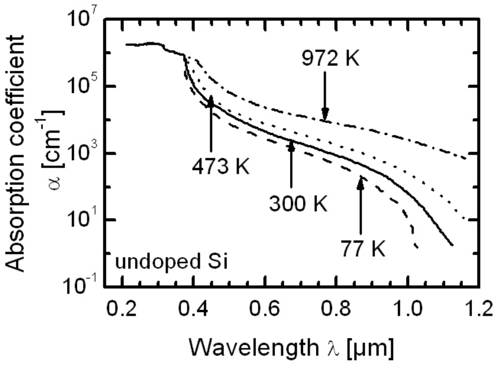

Fig. 2.2: With increasing temperature the absorption coefficient α for photon energies smaller than the direct band gap of silicon continuously increases from $T = 77$ K to $T \approx 1000$ K due to the temperature induced increase in n_i and therefore N_{fcc}. Because of the wavelength dependence of FCA the absorption coefficient is increased stronger for longer wavelengths (figure reproduced from [10]).

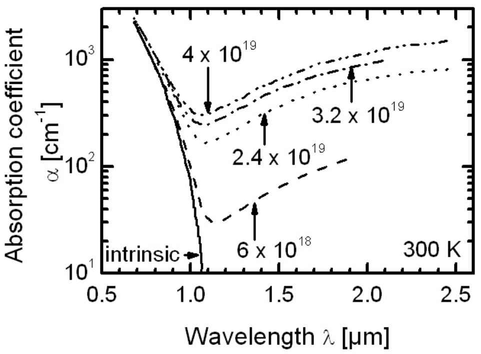

Fig. 2.3: A high doping density $N_D > 10^{18}$ cm^{-3} increases the absorption coefficient for long wavelengths due to FCA, as the carrier density increases due to the doping. Regardless of the doping density, all curves for highly doped Si exhibit an absorption minimum around $\lambda \approx 1100$ nm (figure reproduced from [10]).

2.1.3 Thermal Properties

Decisive parameters for the thermal behavior during laser doping are mainly the thermal conductivity $\kappa_{Si}(T)$, the specific heat $c_p(T)$, the thermal diffusivity $D_{therm}(T)$, the density ρ_{Si}, the absorption length L_α and the laser pulse duration τ_p. Typical values at $T = 300$ K are [23]: $D_{therm} = 0.85$ cm^{2}s^{-1}, $\kappa_{Si} = 1.5$ Wcm^{-1}K^{-1}, $c_p = 0.71$ Jg^{-1}K^{-1}, $\rho_{Si} = 2.32$ gcm^{-3}.
For the description of silicon melting, also the melting temperature $T_m = 1690$ K, the evaporation temperature $T_b = 2654$ K and the latent heat are necessary. Dassow [24] further presented parametrizations for the temperature dependence of c_p and κ_{Si}.

In analogy to the charge carrier diffusion length L, the thermal diffusivity together with the laser pulse duration determine a thermal diffusion length or thermal penetration depth

$$L_{therm} = \sqrt{D_{therm}\tau_p}. \tag{2.7}$$

A qualitative sketch of L_{therm}, depending on the pulse duration, together with the optical penetration depths of some representative laser beam wavelengths is depicted in Fig. 2.4. It shows that already the three main wavelengths of commercially available Nd:YAG lasers range between $L_\alpha \approx 10$ nm ($\lambda = 355$ nm) and $L_\alpha \approx 900$ μm ($\lambda = 1064$ nm, intrinsic Si). The corresponding laser pulse durations for $L_{therm} = L_\alpha$ extend from the ps to the ms range.

In reality, upon laser irradiation, both optical and thermal penetration depths are smaller than the depicted values, due to the increase of α with T and N_{fcc}, as well as the decrease of D_{therm} with temperature T. Further, as soon as the silicon melts at the surface, its absorption changes to metallic behavior and thus $L_\alpha \approx 10$ nm, regardless of wavelength. The strongly nonlinear dependencies of all relevant parameters therefore require numerical simulation for an exact determination of the temperature distribution inside laser irradiated silicon. However, some "rules of thumb" can already be extracted from the relationships depicted in Fig. 2.4:

- As L_{therm} increases with τ_p, longer laser pulses require higher pulse energies for melting the silicon surface, as more heat diffuses away from the illuminated region already during the pulse. Because of the same reason, longer pulses allow for a deeper melting of the silicon without surface evaporation.
- Shorter wavelengths deposit the laser pulse energy in a much smaller volume. Therefore, the threshold for melting and evaporation are lower than for longer

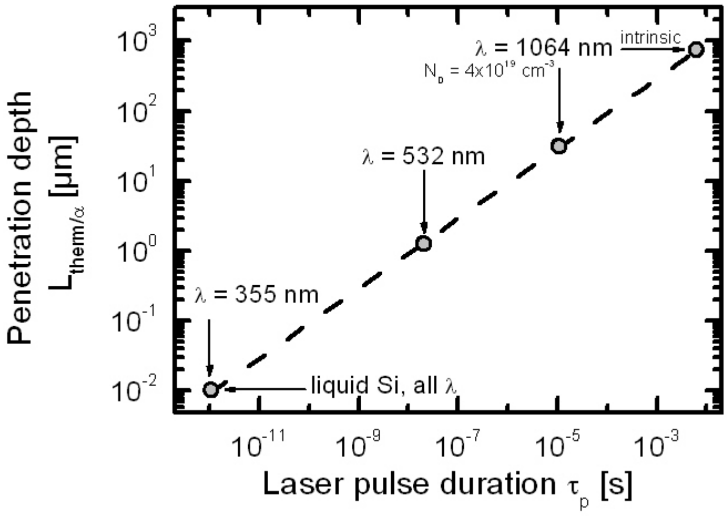

Fig. 2.4: The thermal penetration depth L_{therm} in silicon is strongly dependent on the duration of the corresponding laser pulse. For ultrashort ps-pulses, $L_{therm} \approx$ 10 nm, whereas for the range of 10 ns $< \tau_p <$ 1 μs, typical for standard solid state lasers, the penetration depth is in the μm-range. For comparison the optical penetration depths for the three main wavelengths of industrial solid state lasers $\lambda = 1064, 532, 355$ nm are included.

wavelengths (given equal τ_p).

- As soon as the silicon surface is molten, the impact of the wavelength virtually vanishes.

2.2 Recombination in Silicon

The total number of charge carriers in a semiconductor is at any time governed by the competing processes of generation and recombination. Generation thereby describes the excitation of an electron from the valence to the conduction band, leaving behind a hole - an electron-hole pair is created. Recombination denotes the opposite process, when an excited electron from the conduction band falls back into a hole in the valence band - the two carriers recombine. Strictly speaking there accordingly exist both a generation as well as a recombination lifetime [25]. However, when talking about lifetimes in the context of solar cells, most often the recombination lifetime is meant. Therefore lifetime throughout this work always refers to the recombination lifetime.

Optical generation of electron/hole pairs takes place by the absorption of photons inside the semiconductor, so

$$G = \frac{\alpha_0}{\alpha_{eff}} N_{p0} e^{-\alpha_{eff}/z} \tag{2.8}$$

with N_{p0} the number of photons incident on the semiconductor surface and z the distance from the surface. Generation is a non-equilibrium process because it creates excess charge carriers, with the corresponding excess carrier densities Δn for electrons and Δp for holes. If no carrier trapping or degeneracy effects are present inside the semiconductor, normally $\Delta n = \Delta p$ holds.

The process directly inverse to optical generation is radiative recombination. It is an intrinsic process, meaning that it can by no means be avoided. Its theory bases on the detailed balance, developed by van Roosebroeck and Shockley [26]. Another intrinsic recombination process is Auger recombination. In contrast, often the most effective recombination process is the so called Shockley-Read-Hall (SRH) recombination, which is extrinsic, i.e. due to irregularities in the semiconductor. The time light-generated excess carriers need to decay due to recombination is defined as the carrier lifetime

$$\tau = \frac{\Delta n}{U} \tag{2.9}$$

with the recombination rate U.

Instead of distinguishing between intrinsic and extrinsic recombination, a different possibility of categorizing the different processes is sorting them, according to the location where they occur. Carriers that decay deep inside the material, away from its surfaces, are subject to bulk recombination, whereas others are lost due to surface recombination. In the context of solar cells also often emitter recombination plays a role, i.e. carriers decaying in a diffused region of the solar cell. In principle, however, emitter recombination is a combination of bulk and surface recombination.

2.2.1 Bulk Recombination

Three different mechanisms contribute to bulk recombination, namely radiative, Auger and SRH recombination. Their individual rates add up to a total bulk recombination rate. As the lifetime is inversely proportional to the recombination rate, the inverse bulk lifetime

$$\frac{1}{\tau_b} = \frac{1}{\tau_{rad}} + \frac{1}{\tau_{Aug}} + \frac{1}{\tau_{SRH}} \tag{2.10}$$

is the sum of the inverse radiative lifetime τ_{rad}, Auger lifetime τ_{Aug} and SRH lifetime τ_{SRH}.

Radiative Recombination

Radiative recombination creates a photon from an electron falling back from the conduction band into a hole in the valence band. The radiative recombination rate is

$$U_{rad} = B(np - n_i^2) \tag{2.11}$$

with B the radiative recombination coefficient. Its value has been calculated to $B = 2 \times 10^{-15}$ cm^{-3}s^{-1}, but experimentally observed values are higher. A commonly accepted value is $B = 9.5 \times 10^{-15}$ cm^{-3}s^{-1} [27]. With Eq. 2.11 the radiative minority carrier lifetime in p-type silicon becomes

$$\tau_{rad} = \frac{1}{B(n_0 + p0 + \Delta n)} \tag{2.12}$$

As silicon is an indirect bandgap semiconductor, radiative recombination is rather unlikely. Thus it plays a significant role only in devices that have a very high nonradiative lifetime, i.e. an exceptional material quality.

Auger recombination

Auger Recombination is a three particle process. It takes place either in the conduction band, where an excited electron falls down to the valence band, giving away its excess energy to a second electron (eeh-process), with a rate $U_{eeh} = C_n n^2 p$, or in the valence band, where an energetic hole recombines with an electron from the conduction band, ridding its energy to a second hole (ehh-process), with a rate $U_{ehh} = C_p n p^2$. C_n and C_p are the Auger coefficients for electrons and holes. Commonly accepted values are $C_n = 2.8 \times 10^{-31}$ cm^{6}s^{-1}, $C_p = 0.99 \times 10^{-31}$ cm^{6}s-1 [28]. Depending on the doping type one of these processes is always dominant over the other, so for low-level (li) and high-level (hi) injection the Auger lifetimes are

$$\tau_{Aug,li} = \frac{1}{C_n N_D^2}, \ \tau_{Aug,hi} = \frac{1}{(C_n + C_p)\Delta p^2} \tag{2.13}$$

for n-type silicon and

$$\tau_{Aug,li} = \frac{1}{C_p N_A^2}, \; \tau_{Aug,hi} = \frac{1}{(C_n + C_p)\Delta n^2} \tag{2.14}$$

for p-type silicon.

This classical view of the Auger recombination implies that the involved particles do not exert any influence on each other. Further research has, however, shown that the concept of free particles cannot be sustained. Hangleiter and Häcker [29] postulated a Coulombic interaction between free electrons and holes, leading to the formation of excitons and thus to a so called Coulombic enhancement of the Auger recombination rate in low to medium injection.

Altermatt et.al. [30] studied Auger recombination further and found a parametrization for the Coulomb enhancement factors introduced by Hangleiter et.al. They also found that the ambipolar Auger coefficient is likewise injection dependent. A number of other authors worked on the Auger recombination, proposing different parametrizations for the injection dependency. Among them were Glunz [31] and Kerr [32]. Their parametrizations are cited in Appendix A. In this work, I will calculate the Auger recombination according to Glunz.

Shockley-Read-Hall Recombination

In many cases, SRH recombination dominates the minority carrier lifetime in silicon. As stated above, SRH recombination is caused by extrinsic irregularities introduced into the crystal, such as impurities or imperfections in the crystal structure, which induce electronical states in the forbidden energy gap, acting as recombination centers. The theory to this recombination process was first developed by Shockley, Read and Hall [33, 34]. According to them, the recombination rate due to a single energetic level in the middle of the forbidden gap is

$$U_{SRH} = \frac{np - n_i^2}{\tau_{p0}(n_0 + \Delta n + n_1) + \tau_{n0}(p_0 + \Delta p + p_1)} \tag{2.15}$$

with $\tau_{p0} = (\sigma_p v_{th} N_t)^{-1}$ and $\tau_{n0} = (\sigma_n v_{th} N_t)^{-1}$ the fundamental lifetimes of electrons and holes. They depend on the concentration of defect states N_t, their corresponding capture cross sections for electrons and holes σ_n and σ_p and the thermal velocity of charge carriers v_{th}. The terms n_1 and p_1 are defined as

$$n_1 = n_i exp\left(\frac{E_t - E_i}{kT}\right), \; p_1 = n_i exp\left(\frac{E_i - E_t}{kT}\right) \tag{2.16}$$

Thereby E_t denotes the energetic position of the trap and E_i the intrinsic energy level. With Eq. 2.9 the SRH lifetime becomes

$$\tau_{SRH} = \frac{\tau_{p0}(n_0 + n1 + \Delta n) + \tau_{n0}(p_0 + p_1 + \Delta n)}{p_0 + n_0 + \Delta n} \tag{2.17}$$

For low injection Eq. 2.17 can be simplified to

$$\tau_{SRH} = \tau_{n0}\left(\frac{p_1}{n_0}\right) + \tau_{p0}\left(1 + \frac{n_1}{n_0}\right) \tag{2.18}$$

for n-type silicon and

$$\tau_{SRH} = \tau_{p0}\left(\frac{n_1}{p_0}\right) + \tau_{n0}\left(1 + \frac{p_1}{p_0}\right) \tag{2.19}$$

for p-type silicon.

2.2.2 Surface Recombination

The surface terminates the periodicity of the crystal lattice. Therefore it severely distorts the electronic structure, generating a multitude of localized electronic levels. Early considerations towards the electronic structure of surfaces can be found in the work of Shockley [35]. Illustrative explanations are given in [36]. The general idea is that, as the atoms located directly at the surface do not have corresponding counterparts to saturate all their valence electrons, they are left with so called dangling bonds. These dangling bonds are statistically disordered, thus leading to the formation of interface states, which take various energetical positions in the forbidden gap, and thus act as effective recombination centers. An interface trap density $D_{it}(E)$ per surface energy interval can be assigned to these states. The dependency of D_{it} on the energy expresses the continuous distribution of the traps over the bandgap.

Surface recombination can be seen as a special case of SRH recombination. Thus, the same formalism holds. However, as there exists not a single energy level but a continuous distribution, an integration is necessary to yield the recombination rate at the surface

$$U_s = (n_s p_s - n_i^2) \int_{E_V}^{E_C} \frac{v_{th} D_{it}(E) dE}{\sigma_p^{-1}(E)(n_s + n_1(E)) + \sigma_n^{-1}(p_s + p_1(E))} \tag{2.20}$$

with n_s, p_s the carrier concentrations at the surface. As can be seen, the defect related parameters are energy dependent. A common quantity to describe the recombination at the surface is the surface recombination velocity (SRV) S, which corresponds to the surface recombination rate and the excess carrier density at the surface according to

$$S(\Delta n_s,\ n_0,\ p_0) = \frac{U_s(\Delta n_s,\ n_0,\ p_0)}{\Delta n_s} \tag{2.21}$$

It is possible to define a surface lifetime τ_s as

$$\tau_s = \frac{\Delta n_s}{U_s} \tag{2.22}$$

In the flatband case, i.e. when no band bending towards the surface exists, the carrier densities at the surface are equal to those in the bulk and the actual surface recombination velocity is given by Eq. 2.21. In reality however, this case seldom holds. Most often there does exist a band bending, due to differences in the work function of silicon and e.g. a contact metal or charged states at the interface or inside a dielectric layer. The second situation occurs for most dielectric films deposited onto the silicon surface for passivation or antireflection reasons, such as silicon nitride (SiN_x) or silicon dioxide (SiO_2). They contain fixed positive charges, that induce a band bending inside the silicon (see also chapter 2.2.6). For a high number of positive charges, the surface of *p*-type silicon is inverted and a space-charge region forms. In these cases it is easier to define an effective surface recombination velocity

$$S_{eff} = \frac{U_s}{\Delta n_b} \tag{2.23}$$

which relates the recombination at the actual surface to the experimentally easier accessible carrier concentration in the bulk.

2.2.3 Emitter Recombination

Speaking of emitter recombination usually refers to carrier decay inside the emitter region, as well as at its surface. These regions are most often heavily doped and the minority carrier lifetime is fairly low, due to the high Auger recombination. Normally the heavy doping is achieved by diffusion processes, which cause a spatial variation in dopant density and, consequently, in carrier concentrations, mobilities and lifetimes. Furthermore, heavy doping effects, such as bandgap narrowing, degeneracy or free-carrier absorption can be present. These variations hamper the modeling of the recombination. On the other hand, due to the heavy doping normally the carrier injection level is low and Auger recombination prevails [37]. Thus, the emitter lifetime is constant and independent of the injection level [38]. According to classical diode theory, the recombination current J_{rec}, injected from the base across the space-charge region into the emitter is

$$J_{rec} = J_{0e} exp\left(\frac{qV}{kT} - 1\right) \tag{2.24}$$

with J_{0e} the emitter saturation current density and V the applied voltage. As V corresponds to the separation of the Quasi Fermi Niveaus (QFN) [39] $np = n_i^2 exp(qV/kT)$. Thus, Eq. 2.24 can be rearranged to

$$J_{rec} = J_{0e}\left(\frac{np - n_i^2}{n_i^2}\right) \approx J_{0e}\left(\frac{np}{n_i^2}\right) \tag{2.25}$$

relating the recombination current to the excess carrier densities at the base side of the junction [38]. Following Kerr and Cuevas [40,41] the emitter recombination rate can be related to the total width W of the sample

$$U_{emitter} = J_{0e}\frac{np}{qWn_i^2} \approx J_{0e}\frac{N_{dop} + \Delta n}{qWn_i^2} \tag{2.26}$$

yielding an emitter lifetime

$$\tau_{emitter} = \frac{qWn_i^2}{J_{0e}(N_{dop} + \Delta n)} \tag{2.27}$$

for low and high injection respecively. Thereby N_{dop} denotes the dopant concentration of the respective material (p- or n-type). The situation when an emitter is present has similarities to the situation when there exists an inverted surface due to positive surface charges, as described in the last section. Thus, defining a virtual surface at the base side of the emitter space charge junction, allows for assigning an effective surface recombination velocity $S_{eff,emitter}$ according to

$$U_{emitter} = S_{eff,emitter}\Delta n = \frac{J_{rec}}{q} = J_{0e}\frac{N_{dop} + \Delta n}{qn_i^2} \tag{2.28}$$

This emitter surface recombination velocity comprises both, the recombination in the bulk of the emitter, as well as at its surface, as stated at the beginning of this section. Likewise it is the quantity which influences the effective minority carrier lifetime, which will be introduced in the next section.

2.2.4 Effective Lifetime

The effective minority carrier lifetime τ_{eff} is influenced by all recombination processes inside the solar cell. As their individual rates add up we obtain

$$\frac{1}{\tau_{eff}} = \frac{1}{\tau_b} + \frac{1}{\tau_s} + \frac{1}{\tau_{emitter}} \tag{2.29}$$

with the bulk lifetime from 2.10. Measurement techniques always access the effective lifetime. Thus, in many cases it is difficult to separate the effect of interest, e.g. surface recombination velocity, from the other quantities, e.g. bulk lifetime.

Accessing the Surface Recombination

This problem has been treated by Sproul [42] for the surface recombination velocity. He analyzed the problem of separating recombination at the front and back surface of a silicon sample from the bulk recombination, using transient photoconductance measurements. In the general case, the recombination velocities at the front, S_f, and the back surface, S_b, differ and the surface lifetime is given by

$$\frac{1}{\tau_s} = \alpha_s^2 D \tag{2.30}$$

where D is the minority carrier diffusion constant and it holds

$$\tan(\alpha_s W) = \frac{S_f + S_b}{\alpha_s D - \frac{S_f S_b}{\alpha_s D}}. \tag{2.31}$$

For equal front and back surface recombination velocities, $S_f = S_b = S_{eff}$, one obtains for the effective surface recombination velocity

$$S_{eff} = \sqrt{D_n \left(\frac{1}{\tau_{eff}} - \frac{1}{\tau_b} \right)} \tan \left(\frac{W}{2} \sqrt{\frac{1}{D_n} \left(\frac{1}{\tau_{eff}} - \frac{1}{\tau_b} \right)} \right) \tag{2.32}$$

If $S_f \neq S_b$, but one (e.g. S_f) of the two is known, then an extraction of the other value is also possible according to

$$S_b = \frac{D_n \left(\frac{1}{\tau_{eff}} - \frac{1}{\tau_b} \right) \, tan \left[W \sqrt{\frac{1}{D_n} \left(\frac{1}{\tau_{eff}} - \frac{1}{\tau_b} \right)} \, \right] - S_f \sqrt{D_n \left(\frac{1}{\tau_{eff}} - \frac{1}{\tau_b} \right)}}{\sqrt{D_n \left(\frac{1}{\tau_{eff}} - \frac{1}{\tau_b} \right)} + S_f tan \left[W \sqrt{\frac{1}{D_n} \left(\frac{1}{\tau_{eff}} - \frac{1}{\tau_b} \right)} \, \right]} \tag{2.33}$$

Sproul [42] suggested an approximation for the surface lifetime

$$\tau_s \approx \frac{W}{2S_{eff}} + \frac{1}{D_n}\left(\frac{W}{\pi}\right)^2 \tag{2.34}$$

which approximates τ_s within 5 % for all values of S_{eff} and

$$\tau_s \approx \frac{W}{2S_{eff}} \tag{2.35}$$

for $S_{eff}W/D < 1/4$.

In principle, these equations are only valid for the case of transient measurements of the effective lifetime. When τ_{eff} is obtained from a steady-state measurement, the equations for extracting the surface recombination velocity are much more complicated [43]. However, Nagel et.al. [44] showed that for a homogeneous carrier distribution inside the wafer, the steady-state and transient equations can be used likewise up to comparably high values of S_{eff}, without too large an error.

Accessing Emitter Recombination

Similar to the assessment of different passivation layers, measurements of the effective minority carrier lifetime are useful for comparing and optimizing solar cell emitters. Equation 2.29 illustrates the dependence of τ_{eff} on the bulk, surface and emitter lifetime. Kane and Swanson [38] proposed an approach to extract the emitter lifetime and consequently the emitter saturation current density (Eq. 2.27). They used a special sample structure, comprising a lowly doped substrate, with the emitter of interest on one side, and a well passivated surface on the other side. Alternatively, a symmetric structure, where the emitter is processed equally on both sides of the sample is even more straightforward, as shown by Cuevas [40]. When measuring the effective lifetime, the lowly doped base enters into high-injection, while the higly doped emitter remains in low-injection. In high-injection, the SRH lifetime is approximately constant and the Auger lifetime can be modeled to a reasonable degree of accuracy (see section 2.2.1). Thus, by subtracting the Auger contribution from τ_b and neglecting radiative recombination there remains

$$\frac{1}{\tau_{eff}} = \overbrace{\frac{1}{\tau_{SRH}}}^{\approx const.} + \overbrace{\frac{1}{\tau_s}}^{\approx const.} + J_{0e}\frac{N_{dop} + \Delta n}{qWn_i^2} \tag{2.36}$$

Using the approach of Cuevas [40] instead, the surface recombination term drops out and $2J_{0e}$ instead of J_{0e} enters into the last term. Plotting $1/\tau_{eff}$ versus Δn the value of J_{0e} can be determined from the slope of the curve. This approach has been used throughout this work to extract the emitter saturation current densities.

2.2.5 Emitter Recombination Models

As pointed out in section 2.2.3, modeling the emitter recombination is usually difficult because the material parameters inside the emitter are position dependent. In earlier days, many authors developed analytical or semi-analytical models to describe the recombination inside heavily diffused regions. These models give an insight into the pyhsical background of emitter recombination, even if some of them are already very complex. A fine compilation of a number of these models is given by Cuevas et.al. [45, 46], analyzing former models from del Alamo [47], Shibib [48], Fossum [37], Bisschop [49] and Park [50]. With computer power being abundant nowadays, numerical device simulators like the widespread PC1D [14] are readily used and yield precise results, so that the analytical expressions are limited to cases which are not covered by the device simulators. In this thesis one of these cases occurs, as the package PC1D does not provide for free adjustments to the minority carrier lifetime of diffusion profiles. In contrast to that it calculates the resulting carrier lifetime by using Auger recombination. While this method possibly holds for the vast majority of diffusion profiles, it cannot appropriately model situations in which additional recombination centers enter together with the dopant species. This, however, is the case for laser irradiated silicon as will be shown in chapter 6. Therefore in this work I use the so called first order approximation from Park et.al. [50] to desrcibe the emitter recombination in the presence of SRH recombination in addition to the high Auger recombination inside the emitter. According to [46] it is a lower bound on the exact numerical solution but already provides a significant degree of accuracy without being too complex. This approximation yields the emitter saturation current density J_{oe}^{1st} to

$$J_{oe}^{1st} = \left(qSp_0(w) + q\int_0^w \frac{p_0(z)}{\tau_p(z)}dz \right) \left[1 + Sp_0(w)A(w) + \int_0^w \frac{p_0(z)}{\tau_p(z)}A(z)dz \right]^{-1} \tag{2.37}$$

with

$$A(z) = \int_0^z \frac{dz}{p_0(z)D_p(z)} \tag{2.38}$$

and S the recombination velocity at the emitter surface, w the emitter width with the surface located at $z = w$, $D_p(z)$ the minority carrier diffusion constant, $\tau_p(z)$

the minority carrier lifetime and $p_0(z) = n_{ie}^2/N_D$ the minority carrier concentration in the presence of bandgap narrowing, all quantities being position dependent. This model now allows for introducing SRH recombination in addition to Auger recombination into an emitter, and for analyzing the influence of the SRH recombination on the saturation current density, by modifying the minority carrier lifetime to

$$\tau_p(z) = \frac{\tau_{Aug}(z)\tau_{SRH}(z)}{\tau_{Aug}(z) + \tau_{SRH}(z)} \tag{2.39}$$

This possibility will be used in chapter 7.

2.2.6 Surface Passivation

As explained in section 2.2.2, the energy states created by dangling bonds at the silicon surface lead to a strong recombination. Suppressing this recombination activity and thus increasing the device performance is usually referred to as surface passivation. In principle two different possible ways lead to lowered surface recombination:

Reduction of D_{it}. In the numerator of Eq. 2.20 the interface trap density D_{it} determines the value of the surface recombination rate U_s. The reduction of D_{it} is achieved by depositing a dielectric layer onto the silicon surface, which saturates the dangling bonds. To date, the lowest interface state densities are achieved by growing a layer of thermal silicon dioxide, which is additionally annealed in forming gas, best with a thin aluminium film on top of it. With alnealed (aluminium annealed) SiO_2 films D_{it} values below 10^{10} cm^{-2} have been achieved [51]. Also other dielectric layers as silicon nitride (SiN_x), silicon carbide (SiC), or also amorphous silicon reduce the interface state density, however not as far as SiO_2. Values of $D_{it} = 10^{11}$ cm^{-2} for SiN_x and SiC were reported in literature [52].

Minimizing n_s or p_s. The SRH recombination process requires electrons as well as holes. Thus, assuming equal capture cross sections $\sigma_{n,p}$, the recombination is maximum if the concentrations for electrons and holes are equal. Thus, recombination is minimized by minimizing the number of one carrier species. At the surface, this e.g. is achieved by bringing charges into or onto a deposited dielectric film. Silicon nitride and to some extent also silicon dioxide contain fixed electric charges, which cause a band bending towards the surface. The exceptional passivation quality of certain nitride films on silicon is mainly attributed to this phenomenon of depleting the surface of minority carrier holes (n-type silicon) or inverting the surface (p-type silicon). A different possibility is to deposit external charges, e.g. by using the corona charge method [53].

2.3 Silicon Solar Cells

2.3.1 Introduction

Solar cells, or correctly spoken, photovoltaic cells, made from crystalline silicon are still dominating the photovoltaic market, even if alternative thin film materials like amorphous silicon (a-Si), cadmium telluride (CdTe), or the chalcopyrite materials copper indium (gallium) selenide (CIGS) or sulfide (CIS), etc. are increasingly gaining market share. All these materials are classical semiconductors, unlike e.g. the compounds used for dye-sensitized or organic solar cells. Accordingly, the basic working principle and the problems that need to be solved in order to optimize them with respect to solar cell operation are similar. All of them rely on the internal photoeffect for the generation of electron hole pairs (compare 2.1.2). In addition, they use an internal electrical field for the separation of the generated carriers, which is established due to a pn-junction. An excellent overview about the working principles of solar cells is e.g. found in [10], or [54]. The following explanations of important solar cell key quantities are basing on silicon as solar cell material.

2.3.2 Equivalent Circuit

Standard Model

The classical equivalent circuit for a silicon solar cell comprises a diode with a saturation current density J_{01} and a diode ideality n_1, which models the actual pn-junction. For an ideal diode in low injection $n_1 = 1$ holds. The diode is bridged by a parallel resistance r_p, incorporating all resistive shunt elements. Both are connected to a series resistance r_s, incorporating resistive losses. Throughout this thesis, I will only use the area-independent units [Ωcm^2] for parallel and series resistance. Upon illumination the cell generates a photocurrent, which is accounted for by an additional current source J_L, connected in parallel to r_p. Standard models feature an additional diode with a saturation current density J_{02} and ideality factor n_2, modeling the recombination inside the space-charge region of the diode. The textbook value for n_2 is $n_2 = 2$. This commonly accepted equivalent circuit model for a solar cell is depicted in figure 2.5.

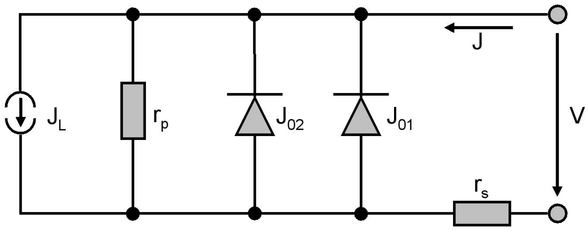

Fig. 2.5: The standard equivalent circuit of a solar cell includes two diodes with saturation current densities J_{01} and J_{02} and ideality factors n_1, n_2. Parallel connected are the shunt resistance r_p, as well as the source producing the photocurrent J_L upon illumination. Resistive losses are incorporated into the series resistance r_s.

Current/Voltage-Curve

The expression for the current/voltage dependence, according to Fig. 2.5 renders the solar cell current density

$$J(V) = J_{01}\, exp\left(\frac{V - Jr_s}{V_T} - 1\right) + J_{02}\, exp\left(\frac{V - Jr_s}{2V_T} - 1\right) + \frac{V - Jr_s}{r_p} \tag{2.40}$$

in the dark and

$$J(V) = J_{01}\, exp\left(\frac{V + Jr_s}{V_T} - 1\right) + J_{02}\, exp\left(\frac{V + Jr_s}{2V_T} - 1\right) + \frac{V + Jr_s}{r_p} - I_L \tag{2.41}$$

in the illuminated case against the terminal voltage V. Here $V_T = kT/q$ denotes the thermal voltage, with $k = 1.38 \times 10^{-23}$ J/K Boltzmann´s constant, T the absolute temperature and $q = 1.602 \times 10^{-19}$ As the elementary charge. At room temperature (T = 300 K), V_T = 25.9 mV. Note that in Eq. 2.41 the sign in the numerator of the exponential term changes from "−" to "+". The reason for the change is that upon illumination the current is generated inside the cell, so the potential across the diode is higher than at the terminals. In the dark, the current is applied from outside, so the potential at the terminals is higher than across the diode [55].

Extended Models

Unfortunately often "real" solar cells cannot be described sufficiently well with the equivalent circuit of Fig. 2.5. A number of authors therefore investigated different types of irregularities. Breitenstein et.al. [56, 57] holds local shunts, e.g. caused by mechanical damage, responsible for ideality factors $n > 2$ and claim multi-step recombination at the damaged sites as origin of the effects.

Esturo-Bretón [58] modifies the 2-diode model by assigning different series resistance values to the two diodes in Eq. 2.40 and 2.41. Accordingly she modifies the numerator in the first exponential in Eq. 2.40 to $V - J\, r_{s1}$ and in the second exponential to $V - J\, r_{s2}$. With the second series resistance she models undoped emitter regions, which are contacted by the front grid and behave like resistively coupled Schottky contacts.

The most comprehensive discussion of unusual solar cell IV-characteristics is found in the thesis of McIntosh [59]. He shows that recombination in the space charge region, which is usually identified with $n_2 = 2$ in reality rather yields $1.6 < n < 1.8$ [60]. Further, he explains higher ideality factors, leading to "humps" in the IV-characteristics by adding a third diode with saturation current density J_{0H}, ideality n_H and series resistance r_H to the standard model. Thus, he accounted for resistance limited recombination like local Schottky contacts or edge recombination, similar to Esturo-Bretón.

The solar cells fabricated in this thesis, however, are not completely described by either of the extended circuits. Reasonable fits can indeed be obtained, however there remains uncertainty about the physical reasons for the chosen fit parameters. It is very probable that in laser doped solar cells different factors like local shunts, Schottky contacts and increased space charge recombination coincide, which would require more complex models. Therefore I limit the analysis in chapters 5 and 7 to the analysis of the IV characteristics and the quantum efficiency.

For the characterization of current/voltage curves, McIntosh used the "local ideality factor"

$$n_{loc} = \frac{1}{V_T}\left[\frac{dV}{d(ln\, I)}\right] = \frac{I}{V_T}\frac{dV}{dI} \tag{2.42}$$

which displays the voltage dependent slope of the IV-curve. Although it does not have a direct physical meaning it is a valuable quantity for the characterization of current voltage curves, as it reveals irregularities more readily than the inspection of an IV-curve alone. The concept of n_{loc} has similarities to the so called "Plot C" for diode analysis, published by Werner [61]. He uses a plot of $dV/d(\ln\, J)$ versus J to obtain the series resistance as well as the ideality factor of Schottky diodes.

2.3.3 Solar cell characterization

Current Voltage Data

Measuring the illuminated current voltage curve of a solar cell, yields the most important values that characterize the cell. The open circuit voltage V_{oc} measured without applied load is dependent on the separation of the QFNs at the edge of the space charge region, and can therefore be seen as a measure of the overall recombination inside the cell.

The short circuit current density J_{sc} measured at $V = 0$, provides information about the optical quality of a cell (e.g. light trapping), as well as its electrical quality (collection efficiency). For an ideal solar cell ($n = 1$) the open circuit voltage depends on J_{sc} approximately according to

$$V_{oc} = V_T \, \ln\left(\frac{J_{sc}}{J_0} + 1\right) \tag{2.43}$$

The Fill Factor

$$FF = \frac{V_{mpp} \, J_{mpp}}{V_{oc} \, J_{sc}} \tag{2.44}$$

describes the shape of the illuminated IV-curve. The values V_{mpp} and J_{mpp} are the voltage and current at the "Maximum Power Point" (MPP). The higher the Fill Factor, the more "rectangular" the illuminated IV-curve and the higher the efficiency

$$\eta = \frac{V_{oc} \, J_{sc} \, FF}{P_{in}} \tag{2.45}$$

with P_{in} denoting the power of the incident light. The theoretical maximum of the Fill Factor FF_0 is dependent on V_{oc} according to

$$FF_0 = \frac{v_{oc} - \ln(v_{oc} + 0.72)}{v_{oc} + 1} \tag{2.46}$$

with $v_{oc} = V_{oc}/n \, V_T$ the normalized open circuit voltage [62]. This definition of v_{oc} shows that the Fill Factor is degraded if $n > 1$ at or close to $V = V_{oc}$ (especially also for $V = V_{mpp}$). High space charge recombination, edge recombination, local shunts, etc. therefore influence both, open circuit voltage and Fill Factor.

The value of FF_0 is reduced by the influence of the series resistance according to

$$FF_s = FF_0 \, (1 - \widetilde{r}_s) \tag{2.47}$$

with $\widetilde{r_s} = r_s/r_{ch}$ the normalized series resistance and $r_{ch} = V_{oc}/J_{sc}$ the characteristic resistance of the solar cell.

Finally, a low parallel resistance further reduces FF_s to

$$FF_p = FF_s \left[1 - \frac{v_{oc} + 0.7}{v_{oc}} \frac{FF_s}{\widetilde{r_p}} \right] \tag{2.48}$$

with $\widetilde{r_p} = r_p/r_{ch}$ the normalized parallel resistance.

While V_{oc}, J_{sc} and FF are easily accessible from the IV-measurement, the extraction of r_p and especially r_s requires more effort to avoid obtaining non-realistic values. The parallel resistance is usually obtained by a fit to the IV-curve in the reverse regime. From Eq. 2.40 follows $J(V) \approx (V/r_p)$ for negative voltages and any reasonable values for r_s and r_p.

For the correct determination of the series resistance there exists a multitude of approaches. A nice comparison is found in [63], from which a method which uses the illuminated IV-curve and the dark curve, shifted by J_{sc} is chosen as most convenient for the use within this work. It was first published by Aberle [64] and determines the series resistance

$$r_{s,light,dark} = \frac{(V_{dark,mpp} - V_{rs,dark}) - V_{mpp}}{|j_{mpp}|} \tag{2.49}$$

with $V_{dark,mpp}$ the voltage at the theoretical MPP of the shifted dark IV-curve, and $V_{rs,dark} = |J_{sc} - J_{mpp}|\ r_{s,dark}$ [65] and further $r_{s,dark} = (V_{dark,jsc} - V_{oc})/\,|j_{sc}|$ [66]. The quantity $V_{dark,jsc}$ thereby denotes the voltage for which $J = 0$ holds in the shifted dark IV-curve.

Quantum Efficiency

Following I/V-characterization, the wavelength dependent measurement of the External (EQE) and Internal (IQE) Quantum Efficiency allows a deeper insight into a solar cells characteristics. The External Quantum Efficiency is thereby defined as

$$EQE(\lambda) = \frac{J_{sc}(\lambda)}{q\,\Phi(\lambda)} \tag{2.50}$$

where $\Phi(\lambda)$ denotes the flux of incident photons at a given wavelength λ.
The Internal Quantum Efficiency arises from the EQE by additionally regarding the reflectance $R(\lambda)$ as

$$IQE(\lambda) = \frac{EQE}{1 - R(\lambda)} \tag{2.51}$$

According to Eq.2.50 and 2.51 the IQE therefore bears information about the collection efficiency of the solar cell for different wavelengths. Due to the dependence of the penetration depth of the incident light on λ, the wavelength dependence of IQE corresponds to different depths in the solar cell. The EQE additionally provides information about the optical quality of the cell. From the EQE the short circuit current density is calculated as

$$J_{sc} = \frac{q}{h\, c_0} \int \lambda\, EQE(\lambda)\, \Phi_{AM1.5}(\lambda)\, d\lambda \tag{2.52}$$

with $h = 6.63 \times 10^{-34}$ Js Planck´s constant, c_0 the speed of light and $\Phi_{AM1.5}$ the photon flux corresponding to the standard AM1.5G solar spectrum. The long wavelength regime of the IQE allows for the extraction of the effective diffusion length inside the bulk of the solar cell, according to [67]

$$IQE^{-1} = 1 + \frac{\cos\theta}{L_{eff}} L_\alpha \tag{2.53}$$

with θ the angle of the incident light. Further, according to Ref. [68] the short wavelength regime bears information about the surface recombination velocity S_E of the emitter, as apparent from the equation

$$(L_\alpha) = \frac{D_E + S_E\, L_\alpha}{D_E + S_E\, d_E} \tag{2.54}$$

with D_E the diffusion coefficient in the emitter and d_E the emitter depth. For $\lambda < 350$ nm the absorption length $L_\alpha \approx 10$ nm and the IQE approaches a constant value.

2.4 Laser

2.4.1 Overview

Since their first appearance in the 1960, lasers have conquered a tremendous number of application fields in the industrial world, as well as in medicine and daily life. Their ability to precisely apply energy in a very localized manner makes them valuable tools. Despite the large variety of different laser types, nowadays mostly solid state lasers have established themselves in photovoltaic industry. Here, the most standard application is laser edge isolation for cSi solar cells [69]. Furthermore, laser ablation for patterning purposes [70], laser drilling [71] or laser doping [72] are other promising applications. For thin film solar cells, the standard patterning process during the module fabrication is laser scribing.

Solid state lasers are the workhorses in the semiconductor and photovoltaic industry. Most often, as also used in this work, diode pumped rod or slab lasers, mostly using Neodymium (Nd) as laser active medium and emitting a ground wavelength $\lambda = 1064$ nm are found. Further, also fibre and disc lasers, using Ytterbium and emitting at $\lambda = 1030$ nm increasingly serve as tools. Depending on the laser medium and the design on the laser, a wide range of operating parameters is accessible. Standard DPSS lasers feature pulse repetition frequencies range from several Hz up to and exceeding $f_p = 200$ kHz. The laser pulse energies E_p usually range from the μJ to the mJ regime and the pulse durations from the low ns to the μs regime. Increasingly also ultra short pulse lasers with τ_p in the ps regime enter the industry.

In the following, a basic compilation of important equations regarding the propagation and shaping of laser light is presented. For a detailed overview about different laser types the reader is referred to the numerously existing literature, such as [73, 74].

2.4.2 Beam Propagation and Optics

In the ideal case, a laser source, operating in the ground or TEM00 mode, emits its radiation as a Gaussian beam [75]. This implies diffraction limited propagation and a radial symmetric, Gaussian intensity distribution, perpendicular to the propagation direction z inside the beam. Thus, the intensity distribution $I(r)$ perpendicular to z is given by

$$I(r) = I_0 \, exp\left(-\frac{2r^2}{w^2}\right) \tag{2.55}$$

with $w(z)$ the beam radius depending on the axial position z, w_0 the minimum beam radius at the beam waist and

$$I_0 = \frac{2P}{\pi \, w_0^2} \tag{2.56}$$

the maximum intensity. Here, P denotes the laser power. Figure 2.6 shows a sketch of a Gaussian beam close to the beam waist. For $z = 0$, $w = w_0$ holds. At the position $z = z_0$, the so called Raleigh length, the beam radius increases to $w = \sqrt{2}\, w_0$, which implies a duplication of beam area. The Raleigh length depends on the wavelength and the beam waist according to

$$z_0 = \frac{\pi w_0^2}{\lambda} \tag{2.57}$$

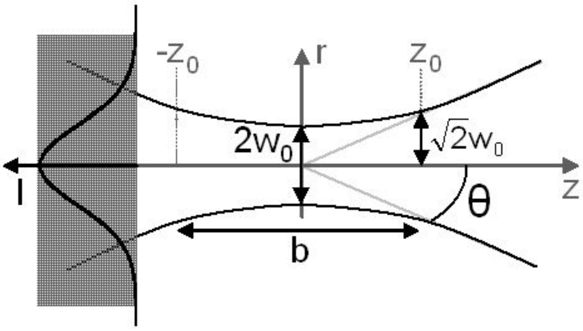

Fig. 2.6: A Gaussian beam has at least one beam waist with minimum beam radius $w(z=0) = w_0$. The Raleigh length z_0 denotes the position where the beam radius has increased to $w(z_0) = \sqrt{2}w_0$, the confocal parameter $b = 2z_0$. The divergence angle $\theta = w_0/z_0$ characterizes the propagation of the beam in z-direction. The grey inset on the left side shows a sketch of the radial intensity distribution $I(r)$.

The divergence angle or divergence

$$\theta_{div} = \frac{w_0}{z_0} = \frac{\lambda}{\pi\, w_0} \tag{2.58}$$

provides information about how the beam diameter expands for large z-values. Generally, a small divergence is a principal attribute of laser radiation. However, Eq. 2.58 shows that a strongly focused beam (which implies a small w_0) entails a large divergence away from the focal point.

Another important parameter for the propagation of laser radiation in optical systems is the Beam Parameter Product (BPP)

$$BPP = \theta\, w_0 = M^2 \frac{\lambda}{\pi} \tag{2.59}$$

with M^2 the so called beam quality factor, which denotes the ratio of the BPP of a real laser beam to the BPP of an ideal Gaussian beam, which has an $M^2 = 1$. Highly brilliant laser sources can reach M^2-values very close to one. The BPP remains constant when the beam passes through optical lenses.

For a rough estimation of lenses for the focusing of collimated (i.e. low divergence) laser beams in optical systems (radius of the collimated beam w_0) there exists a "rule of thumb" [73] for the minimum achievable beam radius

$$w_f = M^2 \frac{\lambda\, f}{\pi\, w_0} \tag{2.60}$$

in the focal point of a lens with focal length f. The depth of focus

$$\Delta z = \pm \frac{\pi\, w_f^2}{\lambda} \sqrt{\left(\frac{w_{tol}}{w_f}\right)^2 - 1} \tag{2.61}$$

describes the axial position in which the beam radius stays below a maximum tolerable w_{tol}. From Eqs. 2.60 and 2.61 it follows that for a given wavelength λ a small focus diameter requires either large beam radii or short focal lengths of the respective lenses.

Chapter 3

Characterization Methods

For the characterization of laser doped silicon and laser diffused emitters, a number of measurement techniques have been employed during this thesis. Most of them are described extensively in the literature. Therefore I will limit their introduction here to a short sketch. Only the Quasi Steady State Photoconductive Decay (QSSPC) technique will be discussed a little more in detail, as it is the main measurement technique of this work.

3.1 Quasi Steady State Photoconductive Decay

Sinton and Cuevas [76] first published the QSSPC technique as a contactless method to determine the effective minority carrier lifetime τ_{eff} of silicon samples. The technique has become one of the standard characterization methods and is also used for the lifetime measurements in this thesis. Figure 3.1 shows a sketch of the measurement setup. The QSSPC measurement setup consists of an inductive coil, forming part of a measurement bridge. The sample is inductively coupled to that bridge. A flash from the light source generates excess carriers inside the sample, thus increasing its conductivity. The higher sample conductivity changes the coil inductivity and thus de-tunes the measurement bridge. The change is picked up by the oscilloscope. The reference cell provides information about the intensity of the light pulse. Both signals are finally analyzed via a PC. According to [76] the change in the sample conductivity

$$\Delta\sigma = \Delta n_{av} q(\mu_n + \mu_p)W \tag{3.1}$$

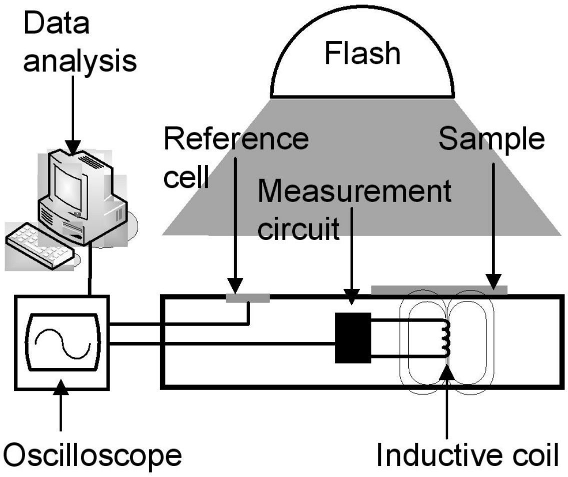

Fig. 3.1: The QSSPC measurement setup consists of an inductive coil, which is connected to a measurement bridge. By inductive coupling, the sample forms part of that bridge. Upon carrier generation inside the sample by a pulse from the light source, the sample conductivity and thus the inductivity of the coil changes, changing the bridge tuning. This change is picked up by the oscilloscope. The reference cell provides information about the intensity of the light pulse. Both signals are finally analyzed via a PC.

with Δn_{av} to optically generated excess carrier density, averaged over the sample thickness W. As the conductivity change $\Delta\sigma$ is detected by the circuit, the excess carrier density Δn_{av} can be determined, when W and the doping density of the sample, and thus the mobilities are known. Nagel et.al. [77] published a definition for the effective lifetime

$$\tau_{eff} = \frac{\Delta n_{av}(t)}{G_{av}(t)\,\frac{\partial \Delta n_{av}(t)}{\partial t}} \tag{3.2}$$

which is independent of the temporal shape of the generation profile G_t for the majority of cases. According to Brody et.al. [78], the average generation $G_{av}(t)$ is thereby determined as

$$G_{av}(t) = SUNS \times EOT \times SCF \times (38\ mAcm^{-2})/(q\,W) \tag{3.3}$$

The value for $SUNS$ stems from the reference solar cell. The value for the "Effective Optical Transmission" EOT considers the acutal photon absorption inside the sample. For sufficiently thick samples, EOT can be approximately determined by measuring the sample reflectivity. An additional correction by the "Spectral Correction Factor"

$$SCF = \frac{\int n_{AM1.5}(\lambda)\; EQE(\lambda) d\lambda}{\int n_{spec}(\lambda)\; EQE(\lambda)\; d\lambda} \tag{3.4}$$

becomes necessary, when the illumination differs from a standard AM1.5G spectrum, or if the sample is coated with wavelength selective layers. In Eq. 3.4 $n_{AM1.5}(\lambda)$ denotes the number of photons in the $AM1.5G$ spectrum at a given wavelength, while n_{spec} denotes the same quantity in the used spectrum. In addition, the Quantum Efficiency of the reference solar cell needs to be known. In this thesis, all measurements are performed with a red filter, which causes a more homogeneous carrier generation inside the sample. This deviating spectrum still allows to use $SCF = 1$.

3.2 Other Characterization Methods

3.2.1 Secondary Ion Mass Spectrometry

Secondary Ion Mass Spectrometry (SIMS) uses different species of ions to destructively analyze the atomic composition of materials. At *ipe* an Atomika 6500 setup serves for the analysis of doping profiles. A detailed description of the SIMS working principle is found in [79].

3.2.2 Sheet Resistance Measurement

The standard technique for sheet resistance determination is the "Four Point Probe" method. According to the name, four sample tips, aligned in a row, with a specific probe distance, touch the sample surface. A defined current is imposed through the two outer tips and the voltage drop, corresponding to the sample resistivity, is measured at the two inner tips with high resistance. Thus, the influence of the metal-semiconductor contact resistance is minimized. A fine explication of this measurement technique is e.g. found in Schroder [80].

3.2.3 Fourier Transformed Infrared Spectrometry

The Fourier Transformed Infrared Spectrometry (FTIR) is an optical characterization method, mostly working in the wavelength regime 2 μm $< \lambda <$ 50 μm. In that regime, characteristic molecular vibrations bands are excited, which provide information about the content of the associated species. In silicon, FTIR is often used for analyzing the content of impurities like Oxygen, Carbon, Nitrogen (as in this thesis), but also dopants, etc. At *ipe* a Bruker IFS 48 setup is used. Further reference on FTIR is e.g. found in [81].

Chapter 4

Laser Doping

4.1 Introduction

Processing semiconductors, using focused laser radiation, has been known for more than 30 years. A first phase of strong research interest spanned the late 1970s and the 1980s, with a tremendous number of publications establishing a theoretical and experimental base for the understanding of the process. White et.al. [82–84] and Wood et.al. [85–87] were among the key researchers. A fine compilation of most results is found in [88] or [89]. The majority of these fundamental experiments was conducted with ion-implanted silicon layers, which were annealed by laser irradiation. Thus, the experiments were not about "real" laser doping. Nevertheless, they produced a number of valuable findings:

- Laser melting of the silicon surface leads to an epitaxial regrowth of the silicon on the underlying substrate.
- The implanted impurity atoms are incorporated into substitutional lattice sites during the recrystallization with,
- their concentrations C_L significantly exceeding the equilibrium solubility limit C_0 as well as,
- their segregation coefficients k_L exceeding the equilibrium values k_0.
- The values of C_L and k_L depend on the recrystallization velocity v_{cryst}.
- The recrystallization velocities are in the range of several m/s.

At the same time to, or following the fundamental research, a number of authors reported results from "real" laser doping experiments, using different types of precursors and laser systems. The most important results from these studies are:

- There exists a threshold laser fluence for the onset of laser doping. This threshold coincides with the silicon melting threshold [90, 91].
- The depth of the laser diffused layers increases linearly with the laser fluence [92, 93].
- Using a high number of repeated laser pulses leads to a rectangular doping profile, with the doping depth corresponding to the melting depth [90, 93–96].
- Infinite dopant sources can be realized using gaseous precursors [90, 91, 96, 97], while
- deposited precursors mostly act as exhaustive sources, leading to a decrease of the maximum doping concentration upon multiple irradiation [94, 95].

In spite of the vast scientific effort spent on characterizing the laser doping process at that time, and first solar cells that were produced [92, 98], no real development of laser doping for photovoltaics was reported until the beginning the 21st century, when the solar industry commenced its incredible growth, and the search for cheaper solar cell production processes intensified. At that time *ipe* started examining laser doping for full area silicon solar cell emitters [2, 99–101], as well as selective emitters [4, 102, 103]. Several groups are also working on selective emitter formation from a phosphorous glass layer (*ipe*), from predeposited dopant layers [5, 6], or from a liquid, dopant containing jet [7].

4.2 The Laser Doping Process

The following section describes the laser doping process, using predeposited precursor layers as employed during this thesis. The fundamental working principle is identical to most of the other known laser doping processes. The main difference lies in the application and structure of the doping precursor, which is performed prior to the process itself.

In this work I use either phosphorous containing liquids, applied by a spin-coating procedure, solid red phosphorous, deposited by sputtering, or aluminium, coated by electron-gun evaporation. The layers are always directly in touch with the silicon substrate, without any interlayers in between. A more detailed description of the complete process is found in chapter 5.

After the precursor deposition, the laser doping process itself starts. Based on the extensive research on laser melting and doping of semiconductors presented above, as well as the experience gathered in the course of this work, the laser doping process is hypothesized to consist of the following stages. These stages are depicted in Fig.4.1.

- a) The laser irradiation heats up the precursor layer and the underlying silicon. Either due to direct light absorption or, depending on the transparency of the precursor layer, due to heat transfer from the underlying silicon, the precursor evaporates and forms a dense vapor phase above the illuminated area.
- b) The silicon surface melts and the melt front advances into the substrate. As soon as the silicon is molten, a liquid state diffusion process of dopant atoms starts.
- c) When the energy supply from the laser pulse ceases, the melt front reverses and the molten silicon recrystallizes epitaxially.
- d) A several 100 nm thick, doped area remains.

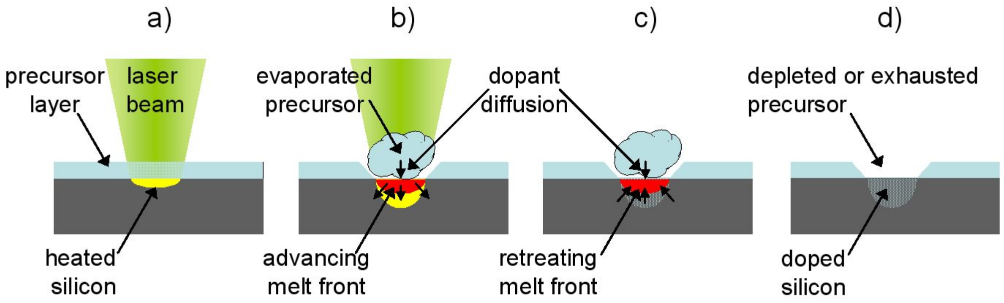

Fig. 4.1: The laser process, employing predeposited dopant precursor layers, consists of several steps. **a)** The impinging laser pulse simultaneously heats up the precursor and the silicon. **b)** The precursor (partially) evaporates and the silicon melts. Dopant atoms diffuse into the melt. **c)** The laser pulse ceases and the melt front retreats. The liquid silicon recrystallizes epitaxially. **d)** A doped silicon layer remains at the surface. The precursor is either partially or completely exhausted.

The size of the doped area depends on the size of the laser focus on the substrate surface. The *ipe* laser doping process uses a line shaped focus in order to avoid the formation of crystal defects, which were detected after laser doping with a circular laser spot [3]. In order to process larger areas, single laser spots are placed next to one another, as described in detail in section 4.4.

4.3 Doping Mechanism

The pulse length of a solid state laser, typically used for laser doping, is in the range of several tens of ns. The time scale in which such a pulse has an impact on the silicon only lasts a few 100 ns maximum (as e.g. shown by modeling in [88] or [104]). During that extremely short time, the impurity incorporation reaches depths of several 100 nm. This fact leaves no doubt that laser doping is a liquid state diffusion process. The diffusion constant of e.g. phosphorous in the solid phase at $T = 1400$ °C of only $D_{P,s} \approx 10^{-10}$ cm^{2}s^{-1} [105] would never allow for such deep an incorporation. In contrast to that, the liquid phase diffusion constant $D_{P,l} \approx 10^{-4}$ cm^{2}s^{-1} [106] does. Apart from that, the laser induced melting of silicon has been studied by several authors using reflectance measurements [90, 107].

What remains less clear, however, is the question of how the incorporation of the dopant atoms from the precursor into the silicon takes place. Bentini et.al. [108] hypothesize due to their doping experiments with gaseous phosphorous precursors that incorporation only occurs for these atoms that are adsorbed at the silicon surface prior to a laser pulse (adsorption model). They consider the direct incorporation of atoms impinging on the molten surface (impingement model) less probable. However, in their publication they only consider low pressure ranges $p < 100$ mbar. In contrast to that, they do not rule out the impingement model for oxygen in gallium arsenide at pressures $p > 1$ *bar* in an earlier publication [109]. Furthermore, some results in chapter 6 as well as the fact that dopant incorporation was detected in cases that the precursor was applied on top of a silicon nitride layer seem to be in favor of the impingement model (also [104]). However, a definite proof, which model matches reality is still to be done.

4.4 Laser Doping at *ipe*

4.4.1 Laser Processing Setups

During the course of this work three different laser processing setups were available at *ipe*. The first setup bases on a processing stage previously used for laser crystallization of amorphous silicon [24]. This setup was modified in order to handle larger samples and to improve the processing stability. The modified setup, which served for processing nearly all of the experiments in this thesis will be referred to as "old setup" in the following. In order to allow for faster processing of large samples a "new setup" with more powerful lasers was established towards the end of this thesis. Only a limited number of experiments was performed with this new setup. Unless otherwise stated, all presented experimental results imply processing on the old setup.

Old Setup

Figure 4.2 depicts a sketch of the laser setup used for the majority of experiments in this thesis. It consists of an Nd:YVO_4 laser, with a maximum output power of $P_{max,old} = 1100$ mW at a laser pulse repetition frequency of $f_p = 20$ kHz and a pulse duration of 10 ns $< \tau_{p,old} <$ 40 ns. Further a simple optical setup comprising a cylindrical lens, an adjustable slit and a commercial photography lens with a focus length $f = 200$ mm form part of the equipment. An xy-gantry, equipped with a vacuum chuck supports the samples during processing. The optics of this system is adjusted to focus the beam into a highly eccentrical ellipsis with a long axis (semimajor) of $l \approx 300$ μm and a short axis (semiminor) of $s \approx 5$ μm, yielding a maximum laser fluence of $D_p \approx 3$ Jcm^{-2} in the center of the focused area. The maximum processing speed with this setup (i.e. maximum area processed per second) amounts to 0.2 cm^{2}s^{-1}.

New Setup

The low processing speed of the old laser setup indeed enables thorough process characterization and the examination of the physical phenomena linked to the laser doping process, but not a proof of concept for an industrial process. Therefore a new laser processing setup was designed, which comprises an increased laser power to $P_{max,new} \approx 35$ W at a pulse duration of 40 ns $< \tau_{p,new} <$ 150 ns. The maximum

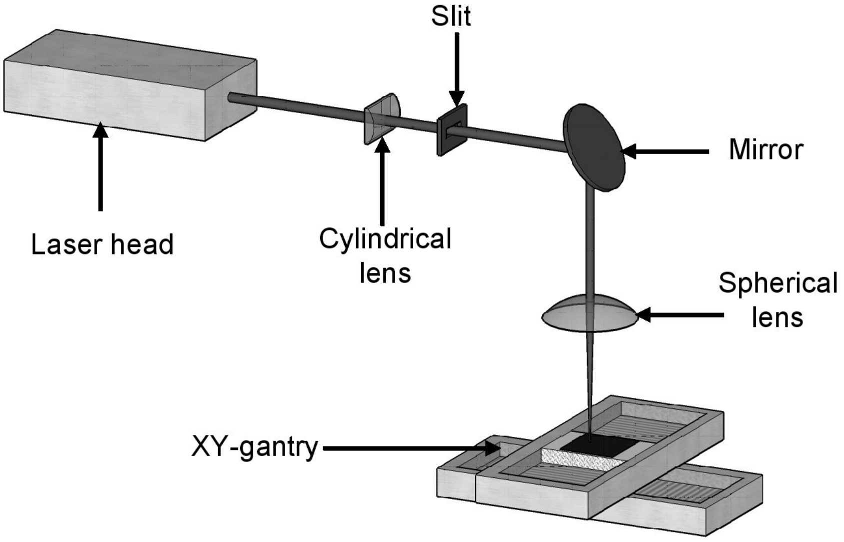

Fig. 4.2: Old laser processing setup. The beam of an Nd:YVO$_4$ laser passes through a cylindrical lens, which transforms the circular into an elliptical beam. An optional slit blocks the outer parts of the beam. After being deflected by a mirror and focused by a camera lens, the beam hits the sample, which rests on an xy-gantry equipped with a vacuum chuck. The gantry provides the scanning movement during the process.

processing speed with this setup approximately reaches 2 cm^{2}s^{-1}.

4.4.2 Processing Sequence

The processing setups work as follows: Each laser pulse melts the silicon surface in the focused area, setting off a local diffusion process every time. The xy-gantry translates the sample with a constant velocity v_{trans}, along the semiminor of the laser focus (y-direction), thus creating a column of laser spots on the surface. Depending on the translation velocity and the pulse frequency of the laser the distance between the single laser pulses is $\Delta y = v_{trans}/f_p$. For the irradiation of larger areas, an additional lateral translation is necessary. After the irradiation of each column the xy-gantry translates the sample along the semimajor (x-direction) by a distance Δx. Consequently the y-movement reverses, scanning the next column. Figure 4.3 shows a sketch of the processing motion.

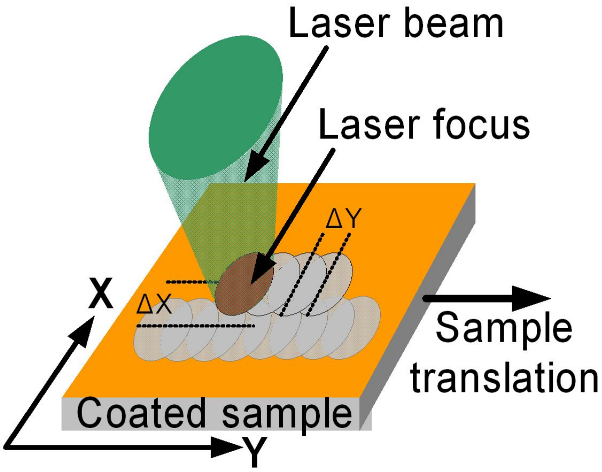

Fig. 4.3: By translating the sample along the semiminor of the focus (y-direction) a column of pulses is scanned onto the sample surface. At the end of the column the sample translates along the semimajor of the focus (x-direction) by a distance Δx. Consequently the y-motion reverses, scanning the next column.

4.4.3 Processing Parameters

To ensure a complete diffusion, the single pulses need to overlap. This pulse overlap

$$O_p = 1 - \frac{v_{trans}}{s f_p} = 1 - \frac{\Delta y}{s} \tag{4.1}$$

is one important parameter, as it defines, how closely the single pulses are spaced on the surface. A close pulse spacing corresponds to a higher number of melt repetitions, each surface element undergoes during the process. In order to irradiate connected areas, single columns are aligned next to each other, additionally translating the sample by Δx at the end of each line scan. Again, a certain part of the columns overlaps, defining the column overlap $O_c = 1 - \Delta x / l$. A more intuitive way of characterizing the pulse and column overlaps is to calculate the number of melting cycles

$$N_{melt} = \frac{s}{\Delta y} \frac{l}{\Delta x} \tag{4.2}$$

which will mainly be used throughout the remainder of this work. The control of both, laser and xy-gantry is performed by a standard PC, equipped with a Digital Signal Processor (DSP)-control card for the gantry. The communication between PC and laser works by an RS-232 connection for both setups.

4.5 Characterization of the beam profile

As the laser diffusion is localized to below 10 μm in one dimension, a precise control and characterization of the energy distribution inside the treated area is required. Fluctuations of the energy density can lead to inhomogeneous doping or even the formation of totally undoped areas [110]. During the time of this work it was shown that above all the outer regions of the focus area, where the local energy density is low, have a crucial effect on the doping results. An overview of the effects influencing the doping homogeneity will be given at the end of this chapter. In the following a method to characterize the energy distribution inside the focus area is described. A similar approach was already used by Dassow [24].

4.5.1 Energy Density Distribution

The beam from the ground mode (TEM00) of a laser has a circular Gaussian energy density distribution

$$D_{p,circ} = \frac{\sqrt{2}E}{\sqrt{\pi}w}\, exp\left(-\frac{2x^2}{w^2}\right) \tag{4.3}$$

with $E = P_{laser}/f_p$ the energy per emitted pulse. Shaping the beam by optical elements like the cylindrical lenses used in the optical setup for laser doping, in first approximation corresponds to a linear operation [75]. Thus the setup conserves the Gaussian energy distribution. However, due to the semimajor and the semiminor of an ellipsis, the cylindrical lens creates two separate beam widths w_x and w_y that originate from the single w of a circular beam. Therefore the energy density distribution $D_{p,ell}$ in the elliptical focus area is given by

$$D_{p,ell} = \frac{2E}{\pi w_x w_y}\, exp\left(-\frac{2x^2}{w_x^2}\right) exp\left(-\frac{2y^2}{w_y^2}\right) \tag{4.4}$$

Figure 4.4 shows a graphical representation of the local laser fluence for a pulse energy of $E = 50$ μJ and beam widths $w_x = 280$ μm and $w_y = 5.0$ μm, as determined for the Nd:YVO$_4$ laser from the old processing setup, operating at $f_p = 5$ kHz.

As the pulse energy can be easily calculated from the measured laser power P and the adjusted repetition frequency f_p, the main difficulty lies in specifying w_x and w_y in order to characterize the pulse energy density. This in turn is a basic prerequisite for characterizing the laser doping process. If we assume that the threshold energy density D_{th} for the melting of silicon is independent from the laser fluence, then

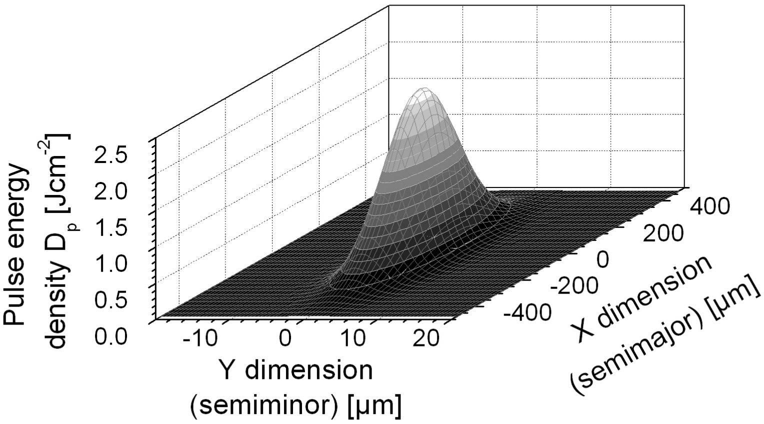

Fig. 4.4: The local laser fluence of a pulse with $E = 50\ \mu$J, $w_x = 280\ \mu$m, $w_y = 5.0\ \mu$m. The maximum fluence in the center of the pulse is $D_{p,max} = 2.3$ Jcm^{-2}.

$$D_{th} = \frac{2E_1}{\pi w_x w_y}\ exp\left(-\frac{2x_{th,1}^2}{w_x^2}\right) = \frac{2E_2}{\pi w_x w_y}\ exp\left(-\frac{2x_{th,2}^2}{w_x^2}\right) \tag{4.5}$$

holds for the energy density along the semimajor of two laser spots (i.e. $y = 0$), irradiated with different pulse energies $E_1 < E_2$, with $x_{th,1} < x_{th,2}$ designating the half width of the melted silicon in the laser focus. Rearranging and taking the natural logarithm yields

$$\ln E_1 - \ln E_2 = \frac{2x_{th,1}^2}{w_x^2} - \frac{2x_{th,2}^2}{w_x^2} \tag{4.6}$$

and finally, letting $l_{th} = 2x_{th}$ be the measured with of the laser irradiated ellipses

$$w_x = \sqrt{\frac{1}{2}\frac{l_{th,2}^2 - l_{th,1}^2}{\ln E_2 - \ln E_1}} \tag{4.7}$$

The determination of w_y is carried out similarly, considering the energy density along the semiminors of the laser spots (i.e. $x = 0$). Thereby the coordinates x_{th} and y_{th} can be determined by irradiating a test sample with different laser parameters and examining the laser pulses via a microscope. Taking values from more than

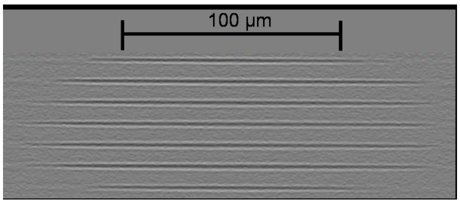

Fig. 4.5: Laser ellipses at $E = 32\ \mu$J. The significant fluctuation in the length of the pulses results from instabilities in the emitted laser power.

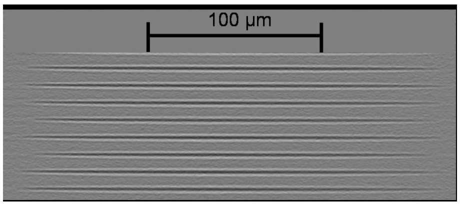

Fig. 4.6: Laser ellipses at $E = 40\ \mu$J. The fluctuation is not as strong as for the lower pulse energy because the laser operates closer to its rated power.

two different pulse energies allows for obtaining multiple values and thus a better accuracy by averaging. This is strongly recommendable, as laser pulse energies are subject to fluctuations as is the measurement of x_{th} and y_{th}. Figures 4.5 and 4.6 show single laser pulses on a bare silicon wafer, scanned with $E_1 = 32\ \mu$J and $E_2 = 40\ \mu$J. From the pictures it is visible that a change in surface relief occurs upon laser irradiation, albeit only slightly at these laser pulse energies. However, there is a large fluctuation in the sizes of the single pulses, resulting from energy variations of the emitted pulses. Additionally the fact that the texture is only a few nm high complicates the exact determination of x_{th} and y_{th} because distinguishing between untreated and recrystallized silicon is difficult. This directly reflects in the accuracy of the determined distribution parameters.

By measuring the lengths l_{th} and the widths $s_{th} = 2y_{th}$ of the melted areas (semimajors and semiminors of the ellipses) the beam widths of the lasers are determined. Having determined the beam parameters it is possible to obtain the threshold energy density D_{th} with an additional set of l and s, by substituting them into Eq.4.5.

4.5.2 Influence of Laser Parameters on Focus

With all these parameters acquired, a simulation of the energy density distribution for a given laser power is possible. Rearranging (4.5) we obtain the coordinates x_{th} and y_{th} for which $D_p = D_{th,x=x_{th}}$ holds as

$$x_{th} = \frac{1}{\sqrt{2}} w_x \sqrt{\ln(2E) - \ln\left(\pi w_x w_y D_{th}\right)} \tag{4.8}$$

.

Figure 4.7 depicts the evaluation of the expected length of the laser melted area versus the total pulse energy for different assumed values of D_{th}. The shape of

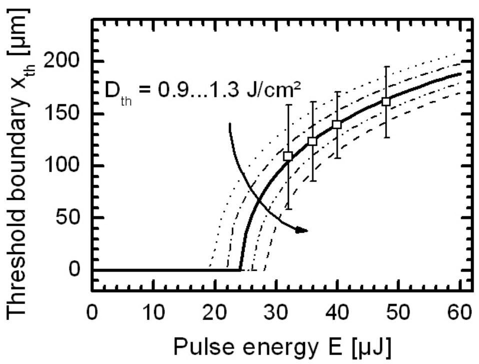

Fig. 4.7: The coordinate x_{th} of the boundary of the laser treated area along the semimajor of the ellipsis exhibits a square root dependence on the employed laser pulse energy E. Varying the threshold energy density 0.9 $\text{Jcm}^{-2} < D_{th} < 1.3$ Jcm^{-2} translates the curves to higher E values, without changing their shape. A fit to the measured x_{th} (solid line) yields $D_{th} = 1.1$ Jcm^{-2} for the old laser setup. The large error bars indicate the difficulties in the determination of the pulse dimensions.

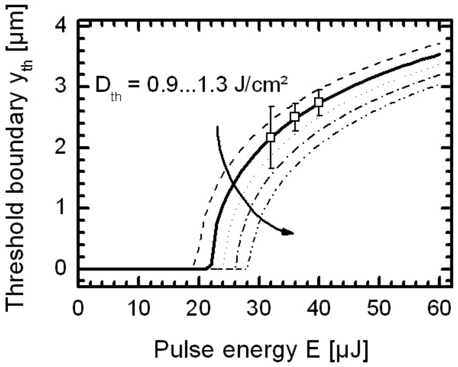

Fig. 4.8: The coordinate y_{th} of the boundary of the laser treated area along the semiminor of the ellipsis exhibits a similar square root dependence on the employed laser pulse energy E, as well as a similar behaviour towards changes in D_{th} as does x_{th}. From a fit to the measured data $D_{th} = 1.0$ Jcm^{-2} is determined.

the curves reflects the $\sqrt{\ln}$ dependence of x_{th} on E. A change in D_{th} corresponds to a parallel translation of the curves along the x-axis without changes in their shape. Just above the threshold pulse energy, the slope of the curves is steep. Therefore already small fluctuations of E lead to a strong variation of the boundary of the laser treated area. Additionally the measured x_{th} of the Nd:YVO$_4$ laser is included in the figure. The measured values follow the course of the simulated curves well, however the error bars indicate the difficulties in measuring the laser pulse dimensions. Fitting the measured x_{th} data results in $D_{th} = 1.1$ Jcm^{-2}. Figure 4.8 shows the same relationship for the small axis of the ellipsis. Again, simulated and measured curves align well, however at a slightly lower value of $D_{th} = 1.0$ Jcm^{-2}, which is inside the uncertainty range.

Figures 4.9 and 4.10 show the evaluation of x_{th} and y_{th} for a variation of the

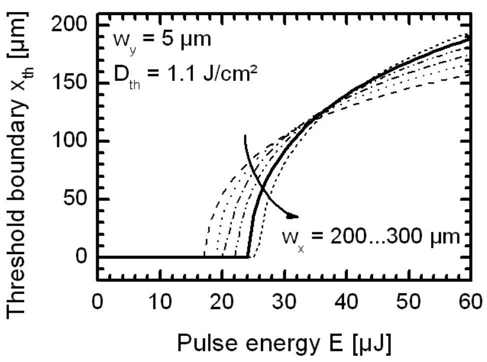

Fig. 4.9: Changing w_x from 200 μm to 300 μm influences the shape of the x_{th} vs. E curve. For a larger w_x the slope increases, as does the threshold.

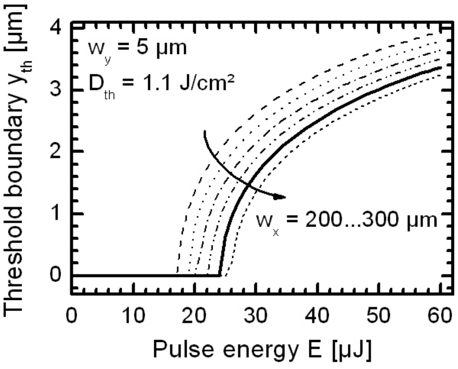

Fig. 4.10: Changing w_x from 200 μm to 300 μm does not influence the shape of the y_{th} vs. E curve. A larger w_x corresponds to an increase in the effective threshold energy density.

beam width w_x and constant D_{th}. The beam width w_x is changed between 200 μm and 300 μm, whereas $w_y = 5$ μm is held constant. With increasing w_x the threshold pulse energy rises in figure 4.9. At the same time, the slope of the curves increases. Figure 4.10 depicts the effect of changing w_x on y_{th}. Here, no change in the shape occurs, only a translation along the x-axis. A change of the beam width of the semimajor (w_x) only changes the effective area of the laser pulse, not the beam width of the semiminor (w_y). Looking at y_{th} such a change therefore has the same effect as a differing D_{th} and is accordingly expressed by the parallel translation of the curves in figure 4.10. Looking at x_{th} the situation is more complicated, as the change in beam width also changes the slope of the Gaussian beam profile. This behavior is illustrated in the figures 4.11 and 4.12, where two sets of gaussian pulse shapes with low $w_x = 100$ (figure 4.11), and high $w_x = 150$ are shown (figure 4.12). The pulse energies $E_{p1,2}$ are equal in both figures. Whereas for the low pulse energy the maximum of the curve with the low beam width already significantly exceeds the threshold energy density in the center, the maximum of curve with the high beam width is just slightly above threshold. Accordingly, the threshold energy density is higher for a larger w_x. This fact is also apparent from figure 4.9. For the high pulse energy the curve with the lower beam width indeed has a much higher maximum pulse energy density in the center, however its width is lower than that of the curve with $w_x = 150$, which corresponds to the higher slope in figure 4.9: for a higher beam width, the threshold coordinate of the beam rises more strongly with E_p.

Leaving all laser parameters apart from the pulse energy fixed, it is possible to calculate important values:

- The maximum pulse energy density $D_{p,max}$ in the center of the laser focus

$$D_{p,max} = D_p = \frac{2E}{\pi w_x w_y} \tag{4.9}$$

- The effective average pulse energy density

$$D_{p,avg} = \frac{1}{l_{th} s_{th}} \int_{-x_{th}}^{x_{th}} \int_{-y_{th}}^{y_{th}} D_p(x,y)\ dxdy \tag{4.10}$$

  defined as the pulse energy integrated over the area in which the local energy density exceeds D_{th}.

- The fraction of effective pulse energy $D_{part} = D_{p,avg} l_{th} s_{th}/E$.

Figure 4.13 depicts these three parameters for $w_x = 280\ \mu$m, $w_y = 5.0\ \mu$m and $D_{th} = 1.1$ Jcm^{-2}, as determined for the old processing setup versus pulse energy. The peak energy density as well as the average energy density increase virtually linear with the pulse energy, however with a different slope. The fraction of effective pulse energy however has a square root dependence on E. For low values of E, $D_p > D_{th}$ holds only in a small part of the focus area. With increasing pulse energy the area, where the threshold is exceeded grows, as visible in figure 4.13 and also in figures 4.11 and

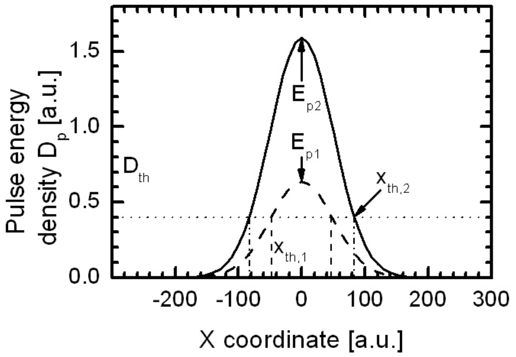

Fig. 4.11: For a beam width $w_x = 100$ the pulse at E_{p1} already exceeds the threshold pulse energy density D_{th} between $-x_{th,1} < x < x_{th,1}$. Increasing the pulse energy to E_{p2} results in a strong rise in the maximum pulse energy density in the center, as well as to an increase of the pulse boundary to $x_{th,2}$.

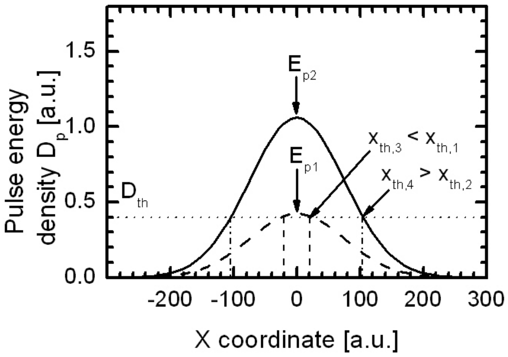

Fig. 4.12: For $w_x = 150$ the pulse at E_{p1} merely exceeds the threshold energy density. Thus the corresponding pulse width is very low, stretching between $-x_{th,3} < x < x_{th,3}$ with $x_{th,3} < x_{th,1}$. The situation is different for E_{p2}, where the maximum D_p is much lower than for $w_x = 100$, but the pulse width is now larger since $x_{th,4} > x_{th,3}$. This corresponds to the later onset and higher slope of the curve in figure 4.9.

4.6 Importance of the beam shape for laser doping

In the previous section the parameters influencing the laser energy density distribution inside the areas irradiated during laser doping were introduced and their mutual dependencies illustrated. This section gives an overview over the influence of the energy density distribution on the homogeneity of laser doped emitters and thus on solar cells. As shown in figure 4.13 a significant part of the total pulse energy is not used for laser doping because it falls in areas, where $D_p < D_{th}$. In these areas the silicon is therefore not melted and no diffusion takes place. However, as the silicon is coated with a doping precursor layer, there exists the possibility that the laser energy outside the active area is still sufficient to alter the properties of this precursor up to its ablation. The resulting problem is depicted in figure 4.14. When

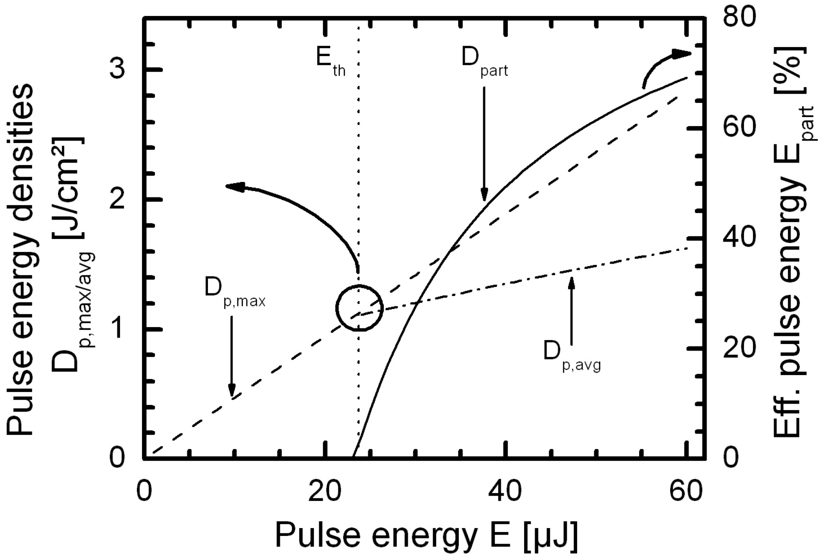

Fig. 4.13: The maximum pulse energy density grows linearly with increasing pulse energy, as does the effective average pulse energy density. However, $D_{p,max}$ increases faster than $D_{p,avg}$. The fraction of effective pulse energy shows a square root dependence on E

the precursor threshold energy density $D_{th,prec}$ is lower than the silicon threshold energy density $D_{th,Si} = D_{th}$, a region of ablated or altered precursor can form next to a scanned column, in the areas where $D_{th,prec} < D_p < D_{th,Si}$ holds. When the scan advances to the next column, the regions with previously altered precursor are in turn melted, leading to a doping profile differing from the profile of the first column (or a totally undoped area) and thus to an inhomogeneous emitter. This phenomenon was published by Esturo-Bretón [110]. She examined the IV curves from diode structures and solar cells laser doped with different pulse energy density profiles. It showed that, using the full Gaussian profile the IV-curves exhibited unexpectedly high values for diode idealities $n_{1,2}$ and could very often not be fitted with standard diode theory at all. Further, the suchlike produced solar cells suffered from low fill factors.

Modifying the energy density profile with a slit that blocked the outer parts of the semimajor of the elliptical laser focus significantly improved the IV-curves and the fill factors of the solar cells. These results are a clear indication that doping inhomo-

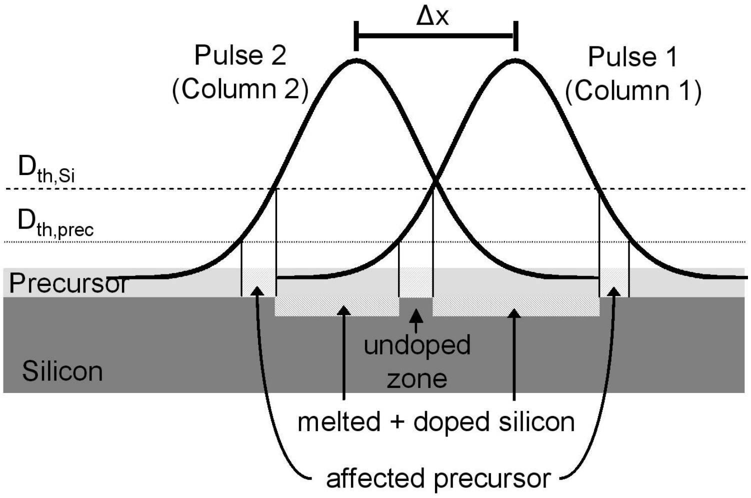

Fig. 4.14: If the doping precursor has a lower threshold energy density $D_{th,prec}$ than the underlying silicon ($D_{th,Si}$) the stacking of irradiated columns for the doping of larger areas is problematic. In the outer parts of one Gaussian pulse (pulse 1), where $D_{th,prec} < D_p < D_{th,Si}$ holds, the precursor is altered or ablated. When the next column is scanned overlapping the first (pulse 2) the regions of ablated precursor are melted, but since the precursor has been ablated by the previous scan the underlying silicon remains undoped and thus introduces inhomogeneities into the emitter.

geneities are introduced by the non-constant energy density profile inside the laser focus. Studies that are not part of this work suggest that Schottky contacts form on lowly or undoped parts of the emitter, severely deteriorating the performance of the device. These results indicate that producing homogeneously laser doped emitters requires a precise control of the energy density profile of the laser pulse and the processing parameters at the same time. Similar effects show on uneven or textured surfaces. Röder [111] examined the IV-characteristics of laser doped solar cells on wafers textured with random pyramids. A complete melting and thus destruction of the pyramidal texture was necessary to obtain reasonable fill-factors. In this case the inhomogeneities are introduced by the uneven surface, not primarily by the laser beam profile. The effects, however, are supposed to be the same.

Chapter 5

Doping Precursors - a Survey

5.1 Introduction

In the course of this work, different materials have been characterized regarding their applicability as doping precursor for the fabrication of both n and p-type emitters. As p-type silicon is the predominant material for solar cell production, the focus of this survey lies on phosphorous precursors. There exist a variety of phosphorous containing liquids on the market, often in a ”spin-on glass” composition, containing phosphorous oxide in a mixture with silicates and solvents. In industrial production lines featuring inline diffusion furnaces, also diluted phosphorous acid is often used as a dopant precursor layer. Out of the available materials, two liquids (Filmtronics P508 and Merck Siodop P250) have been selected for the characterization. In addition to these liquid doping precursors also the use of directly sputtered phosphorous layers is studied. For that purpose red phosphorous is used as precursor because of its feasibility and hygienic harmlessness. The Target to Intermediate Target (TIT) method [112] enables the deposition as well as the tuning of the layer composition.

One candidate for the fabrication of p-type emitters on n-type substrates, or back surface fields on p-type substrates is aluminium. The aluminium layers are deposited by electron-beam evaporation of bulk aluminium. This survey examines the applicability of all the above mentioned precursors characterizing the sheet resistance resulting after laser irradiation. Further, doping profiles are determined by SIMS. All precursors are additionally used to fabricate solar cells.

As the focus of this work does not lie on solar cell optimization, the fabricated solar cells mostly suffer from reduced Fill Factors due to emitter inhomogeneities, local shunts or local Schottky contacts, as mentioned in chapter 4.6. Still the fabricated cells characterize the principal feasibility of all examined doping materials, as well as differences in their potentials. A closeup on the key characteristics of the emitters, disregarding the technological problem of doping homogeneity, is the content of chapter 7. An assessment of the laser doping process towards its implementation in an industrial environment will be given in chapter 8.

5.2 Phosphorous

5.2.1 Experimental

For the sheet resistance characterization, polished p-type Cz and FZ samples are used. The samples undergo the coating step on a laboratory spin-coater followed by a bakeout step on a hotplate at a temperature $T = 300\ ^{\circ}\mathrm{C}$ for a time $t = 12$ min. After the bakeout, the layer thickness for the $P250$ samples amounts to $d_{P250} \approx 100$ nm, whereas $P508$ layers reach $d_{P508} \approx 400$ nm due to their higher viscosity. Following the bakeout the samples are ready for laser irradiation. The range of the laser pulse energy densities extends from $0.7\ \mathrm{Jcm}^{-2} < D_p < 2.1\ \mathrm{Jcm}^{-2}$, with different values for N_{melt}. In order to avoid sample to sample fluctuation, every sample carries multiple areas irradiated with the varying laser parameters. After the laser process, a cleaning step in diluted Hydrofluoric Acid (5 % HF) removes the residues of the precursors and cleans the samples.

The sputtered phosphorous layers are prepared with the TIT-method. By changing the deposition time, the thickness of the phosphorous layers is adjusted between $2\ \mathrm{nm} < d_P < 30\ \mathrm{nm}$. After coating, the samples directly receive the laser irradiation with $0.8\ \mathrm{Jcm}^{-2} < D_p < 2.5\ \mathrm{Jcm}^{-2}$, without any necessary annealing step. The cleaning of the residual phosphorous requires a full RCA cycle, instead of only an HF-dip as in the case of the liquid precursors. After cleaning, the sheet resistance data for both precursor types is measured with a 4-point probe setup. For every laser parameter five individual measurements are averaged across the irradiated area. Selected samples subsequently serve for the determination of their doping profile by SIMS. In the following only data for $N_{melt} = 2$ is presented, as a higher number of melt repetitions does not change the doping behavior significantly, but is less beneficial with regard to implementation. Further, the results in chapter 6 show that a higher number of melt repetitions degrades the minority carrier lifetime.

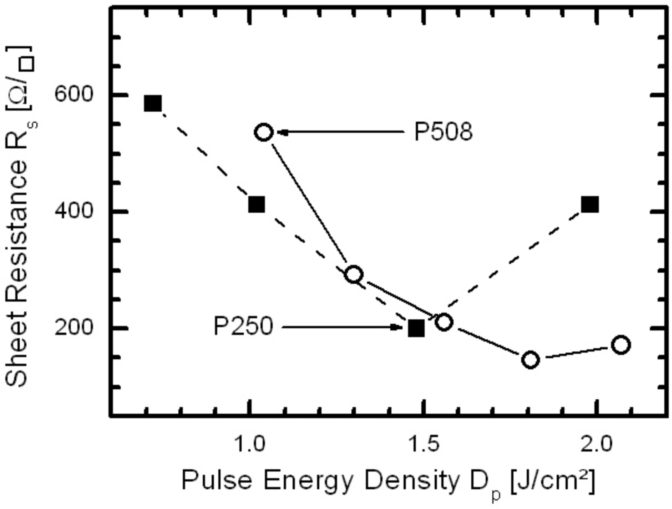

Fig. 5.1: The dependence of sheet resistance on laser pulse energy density is similar for both tested doping precursors. Low pulse energy densities result in high values of $\rho_s = 537\ \Omega/\Box$ at $D_p = 1.0$ Jcm^{-2} and $\rho_s = 586\ \Omega/\Box$ at $D_p = 0.7$ Jcm^{-2} for P508 and P250 respectively. The higher minimum D_p for P508 results from the higher precursor thickness. The minimum achieved sheet resistance lies at $\rho_s = 149\ \Omega/\Box$ with $D_p = 1.8$ Jcm^{-2} for P508 and $\rho_s = 200\ \Omega/\Box$ with $D_p = 1.5$ Jcm^{-2} for P250. For both precursors ρ_s increases again towards high values of D_p, which is caused by partial surface evaporation.

5.2.2 Sheet Resistance

Figure 5.1 depicts the dependence of the sheet resistance for the two precursors P508 and P250 on the laser pulse energy density for $N_{melt} = 2$. Both curves exhibit similar characteristics of a strong decrease from values of $\rho_s \approx 600\ \Omega/\Box$ at low pulse energy densities to $\rho_s < 200\ \Omega/\Box$ at intermediate D_p-values. For high pulse energy densities the sheet resistances increase again for both precursors. For P508 the minimum lies at $\rho_s = 149\ \Omega/\Box$ at $D_p = 1.8$ Jcm^{-2}, whereas P250 reaches $\rho_s = 200\ \Omega/\Box$ at $D_p = 1.5$ Jcm^{-2}. The increase of the sheet resistance at high pulse energy densities comes along with a strongly visible roughening of the silicon surface. This roughness is a sign of silicon ablation, which in turn explains the increase in sheet resistance.

For the sputtered phosphorous precursor, three different layer thicknesses of $d_P = 2,\ 10$ and 30 nm are characterized. Figure 5.2 depicts the corresponding results.

There exists an apparent difference between $d_P = 2$ nm and the two higher precursor thicknesses. Whereas the latter curves exhibit a very rapid drop of ρ_s with D_p, the decrease of the sheet resistance with rising D_p is much slower for $d_P = 2$ nm. This points to changes in the dopant incorporation behavior with increasing layer thickness. The absolute ρ_s-values strictly follow the succession of layer thicknesses, as well as pulse energy densities, with $d_P = 30$ nm corresponding to the lowest $\rho_s = 28\ \Omega/\Box$ at $D_p = 2.5$ Jcm^{-2}. The layer thicknesses $d_P = 10$ and 2 nm yield minimum values of $\rho_s = 39$ and 130 $\Omega/\Box$ respectively at the same pulse energy density. Comparing the pulse energy densities of figure 5.2 with the corresponding values of figure 5.1 one notices that in the case of the sputtered precursors no increase of ρ_s for high values of $D_p = 2.5$ Jcm^{-2} is seen. In contrast to that the sheet resistance for the liquid precursors already increases again for $D_p = 2.1$ Jcm^{-2}, accompanied by a visible surface roughening.

The reason for the higher sensitivity of the liquid precursors is not perfectly clear. One possible explanation could be better coupling of the laser light due to an anti reflective effect of the coated layer in the case of the liquid precursors.

5.2.3 Doping profiles

Figure 5.3 shows the doping profiles of selected samples from the series with the P250 precursor and $D_p = 0.7,\ 1.0$ and 1.5 Jcm^{-2}. Corresponding to the increasing pulse energy density the emitter depth d_e increases from $d_e \approx 100$ nm to $d_e \approx 220$ nm for 0.7 Jcm^{-2} $< D_p <$ 1.5 Jcm^{-2}, as the irradiated silicon melts up to a higher depth when receiving more laser energy. At the same time the maximum surface concentration increases from $C_s = 2.5\times10^{19}$ cm^{-3} to $C_s = 6\times10^{19}$ cm^{-3}. The doping profiles for P508 and 1.4 Jcm^{-2} $< D_p <$ 1.7 Jcm^{-2} are presented in figure 5.4. Here the emitter depth reaches values of $d_e \approx 250$ nm at the maximum D_p due to the larger pulse energy density compared to the P250 samples. The maximum concentration is higher than that in figure 5.3, reaching values of $C_s \approx 1 \times 10^{20}$ cm^{-3}. These values correspond to the lower sheet resistances measured for P508 when compared to P250. Regardless of the slightly higher phosphorous concentration in the case of P508, there is no significant difference in the behavior of the two precursors regarding their doping profiles. This points out that the incorporation mechanism for the phosphorous atoms is similar. As the doping profiles of figure 5.3 and 5.4 will be used for the calculation of emitter saturation current densities in chapter 7, they are linearly scaled from the original SIMS data in order to match the measured

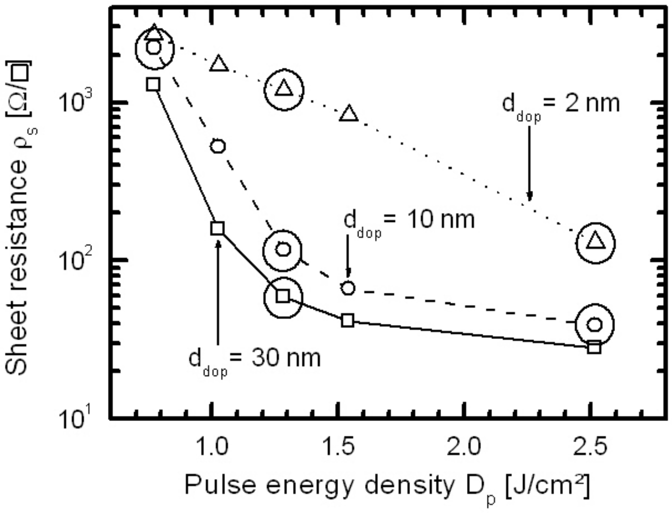

Fig. 5.2: The sheet resistance of sputtered doping precursors is strongly dependent on the thickness of the dopant layer, as well as the laser pulse energy density. The series with $d_P = 10$ and 30 nm exhibit similar courses with a steep decline of the sheet resistance from $\rho_s > 1000\ \Omega/\square$ at $D_p = 0.8\ \mathrm{Jcm}^{-2}$ down to $\rho_s = 39\ \Omega/\square$ ($d_P = 10$ nm) and $\rho_s = 28\ \Omega/\square$ ($d_P = 30\ nm$) at $D_p = 2.5\ \mathrm{Jcm}^{-2}$. The series with the lowest precursor thickness $d_P = 2$ nm shows a different behavior with a much lower slope of the sheet resistance decrease. Accordingly the minimum ρ_s for this low precursor thickness is only $\rho_s = 130\ \Omega/\square$ at the maximum pulse energy density. The circles mark the samples that are additionally characterized by SIMS.

sheet resistances: Using the majority carrier mobility from Eq. (2.2), the expected sheet resistance ρ_{calc} is calculated from the original SIMS data, assuming complete activation of the detected phosphorous. Using ρ_{calc}, a scaling factor A is iteratively determined until $\rho_{calc} = \rho_s$. This scaling factor can also be interpreted as the fraction of activated phosphorous inside the emitters. For P508 the scaling factor ranges between $0.6 < A < 0.8$, whereas P250 reaches lower values of $0.4 < A < 0.6$. All other presented doping profiles are unscaled. The corresponding activation factors are given separately.

For the sputtered doping precursors, the three different layer thicknesses as well as three different pulse energy densities are characterized by SIMS. Figure 5.5 depicts the behavior of the profiles with varying precursor layer thickness at a pulse energy

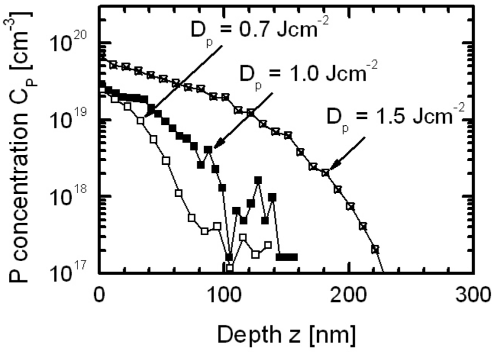

Fig. 5.3: The samples doped with P250 precursor exhibit emitter depths increasing from $d_e = 100$ nm to $d_e = 220$ nm as well as surface concentration rising from $C_s = 2.5 \times 10^{19}$ cm^{-3} to $C_s = 6 \times 10^{19}$ cm^{-3} for 0.7 Jcm^{-2} $< D_p <$ 1.5 Jcm^{-2}.

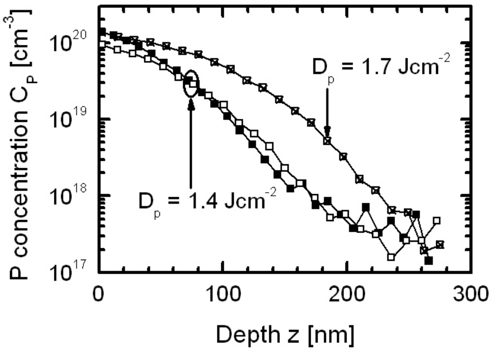

Fig. 5.4: In comparison with the P250 samples, the samples doped with P508 precursor exhibit comparable emitter depths around $d_e \approx 250$ nm and slightly higher surface concentration values of $C_s \approx 1 \times 10^{20}$ cm^{-3} for $D_p = 1.4$ and 1.7 Jcm^{-2} respectively.

density of D_p = 1.3 Jcm^{-2}. Clearly the maximum doping concentration at the surface increases almost linearly from $C_s = 1 \times 10^{19}$ cm^{-3} for $d_P = 2$ nm to $C_s \approx 1.5 \times 10^{20}$ and 5×10^{20} cm^{-3} for d_P = 10 and 30 nm respectively. The profile depth also increases, albeit less pronounced from $d_e \approx 100$ nm to $d_e \approx 200$ nm. The corresponding activation factors show an opposite behavior. Whereas $A = 0.85$ for $d_P = 2$ nm, the activation drops to $A = 0.53$ and $A = 0.33$ for $d_P = 10$ nm and 30 nm respectively. Obviously the excessively available phosphorous from the thicker precursor layers is not incorporated efficiently into electrically active sites in the silicon lattice. Figure 5.6 depicts the influence of varying pulse energy density 0.8 Jcm^{-2} $< D_p <$ 2.5 Jcm^{-2} at a constant layer thickness of $d_P = 10$ nm. In this case the maximum doping concentration stays virtually constant at $C_s \approx 1.5 \times 10^{20}$ cm^{-3}, whereas the doping depth increases from 90 nm $< d_e <$ 360 nm. The increase in profile depth is close to linear, which is due to the rising melting depth time of the silicon, when the laser pulse energy density increases. The larger melting time also seems to increase the electrical activation. Whereas for D_p = 0.8 Jcm^{-2} $\rho_s > 3\ k\Omega/\Box$ and thus $A < 0.1$, the activation increases to $A = 0.53$ and $A = 0.87$ for D_p = 1.3 Jcm^{-2} and 2.5 Jcm^{-2}, respectively. Obviously, the addition of the precursor layer thickness as a free parameter allows for an extensive control of the

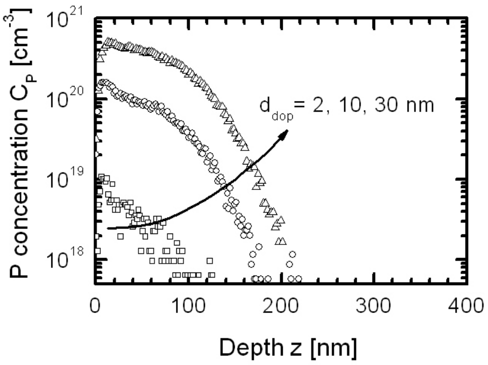

Fig. 5.5: The maximum doping concentration at the surface C_s increases strongly from $C_s \approx 10^{19}$ cm^{-3} to $C_s \approx 5 \times 10^{20}$ cm^{-3} when the thickness of the precursor layer rises from 2 nm $< d_P <$ 20 nm. The increase of C_s is almost linear with d_P. The depth of the doping profile likewise increases, albeit just twofold from $d_e \approx 100$ nm to $d_e \approx 200$ nm.

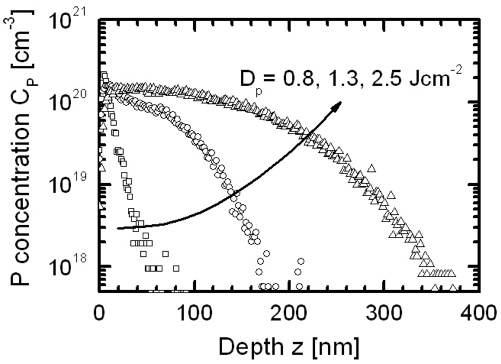

Fig. 5.6: Whereas $C_s \approx 1.5 \times 10^{20}$ cm^{-3} stays virtually constant for increasing pulse energy density, the doping depth rises significantly from 80 nm $< d_{emitter} <$ 380 nm for 0.8 Jcm^{-2} $< D_p <$ 2.5 Jcm^{-2}. The increase of $d_{emitter}$ is almost linear with D_p.

desired doping profiles in the case of sputtered phosphorous dopant layers. This fact was also shown by Eisele [113].

5.2.4 Solar Cells

Experimental

Solar cells are fabricated using the P250, P508 and sputtered doping precursors. As there were two different sputtering setups available in the course of this work, two series of solar cells with sputtered precursor have been characterized. According to which setup carried out the precursor depositon the cells are denoted "Sputter 1" and "Sputter 2". All solar cells fabricated on p-type substrates use evaporated Ti-Pd-Ag as front and aluminium as back contact material. The P250 and Sputter 1 cells feature p-type, FZ, 0.5 Ωcm samples, with a thickness $w = 250$ μm, a thermal oxide passivation with point contacts on the back, silicon nitride passivation and photolithographically defined contacts on the front side. The P508 cell is fabricated

Tab. 5.1: All presented solar cell results originate from p-type, FZ substrates with $w = 250\ \mu$m. The solar cell parameters for P250 and Sputter 1 precursor are averaged values from 6 equally processed samples. Both series feature 0.5 Ωcm samples. They have oxide passivated back sides with aluminium point contacts and a photolithografically defined front electrode. The P508 and Sputter 2 samples are fabricated on 1 Ωcm samples. They have full area aluminium back contacts and front electrodes defined by a shadow mask.

Sample	V_{oc}[mV]	J_{sc} [mAcm^{-2}]	FF[%]	η[%]
P250	634 ± 2.7	34.5 ± 0.9	56.3 ± 2.5	12.3 ± 0.8
Sputter 1	604 ± 2.8	33.3 ± 0.4	59.1 ± 1.4	11.9 ± 0.4
P508	618	34.1	68.1	14.4
Sputter 2	619	32.0	75.9	15.0

on p-type, FZ, 1 Ωcm material with a thickness $w = 250\ \mu$m and features front contacts defined by shadow mask as well as an evaporated full area back contact. The Sputter 2 cells are fabricated on the same substrate as the P508 cells. They have shadow mask evaporated front and full area back contacts. The cell area is always $A_{cell} = 4$ cm^2. Table 5.1 contains a representative compilation of solar cell results with n-type phosphorous emitters. For P250 and Sputter 1 the average of six equally processed cells is presented.

The cell parameters for the P250 precursor exhibit a relatively high open circuit voltage $V_{oc} > 630$ mV. However, considering the high quality back side with aluminium point contacts, significantly higher open circuit voltages would be expected. The most striking parameter is the remarkably low fill factor $FF < 60$ %. Therefore the efficiency of these cells only reaches $\eta = 12.3$ %. The Sputter 1 precursor exhibits even lower open circuit voltages of only $V_{oc} = 604$ mV. As the cell structure is equal for the P250 and Sputter 1 series the lower V_{oc} and J_{sc} indicate that the emitter quality for the liquid doping precursor is superior. The P508 cell reaches $V_{oc} = 618$ mV and a higher Fill Factor $FF = 68.1$ %. The Sputter 2 solar cell even reaches $FF = 75.9$ %, a value which is already in the range of industrial solar cells. The $V_{oc} = 619$ mV of this cell is probably limited by the aluminium back contact and the low emitter passivation quality due to the shadow mask evaporation, which also holds for the P508 cell.

The following figures show the dark IV-characteristics as well as the local ideality factors of selected solar cells from the above table. As apparent from figure 5.7 the dark IV-curves of the P250 and Sputter 1 cells show strong similarities. Examining the reverse current region yields rather low parallel resistances $r_p \approx 3\ k\Omega cm^2$ for both cells. In the forward region their curves both exhibit a strongly non-ideal behavior with a very low and almost constant slope up to $V = 0.8$ V. This low slope points to a massive interference of emitter inhomogeneities or local shunts on the IV-characteristic. In fact the expected diode behavior is totally masked by these effects in the case of the P250 and Sputter 1 cells. This strange behavior reflects in the low fill factor. The curves for the Sputter 2 and P508 cells more resemble the "normal" IV-curve of a solar cell. Their parallel resistances $r_p \approx 100\ k\Omega\mathrm{cm}^2$ are high enough to exclude influence of the parallel resistance on the Fill Factor. In the forward voltage region the P508 cell exhibits a noticeable hump up to $V \approx 0.5$ V. The curve of the Sputter 2 cell only shows a very little upward curvature at low forward voltages. The strength of this curvature directly reflects in the measured Fill Factors of the solar cells: the less pronounced the hump the higher the Fill Factor. The local ideality factors in figure 5.8 depict the irregularities in the measured IV-curves. The local ideality factors of the P250 and Sputter 1 series exhibit minimum values of $n_{loc} = 2.7$ (P250) and $n_{loc} = 3$ (Sputter 1). The Sputter 2 cell shows a minimum $n_{loc} = 1.2$, whereas the P508 cell exhibits $n_{loc} = 1.7$ at minimum.

Table 5.2 shows the results of a more detailed characterization of the four selected solar cells. The values for r_s were determined using Eq. 2.49, while Eqs. 2.46 - 2.48 served to determine $FF_{0,n}$ and FF_p, with FF_p including FF_s. For assessing the influence of the ideality factor, the values $n_{loc,min}$ from Fig. 5.8 were used, as the characterization according to [61] did not yield consistent results. For all four cells the Fill Factor without considering the ideality factor $FF_0 = 83$ %. The presented values clearly show that the Fill Factors of the P250 and Sputter 1 cells indeed are mainly limited by the high ideality factors, as $FF_{0,n} = 67.9$ % and 64.3 % for P250 and Sputter 1, respectively. Their relatively high series resistances cause a further decrease of their fill factors. Due to its low $n_{loc,min}$ the Sputter 2 cell reaches the highest Fill Factor $FF = 75.9$ %, which is mainly due to its $r_s = 1.22\ \Omega\mathrm{cm}^2$. The P508 cell ranges in between. The higher ideality causes a drop of the Fill Factor down to $FF_{0,n} = 75.4$ % and the series resistance a further decrease to $FF_p = 66.5$ %. For all four cells but Sputter the deviation of the theoretical to the actually measured Fill Factor is less than three percent. Thus the use of $n_{loc,min}$ for the estimation of the impact of the ideality on the Fill Factor seems justified.

The data shown in figures 5.7 and 5.8 reveals the inhomogeneity problems from

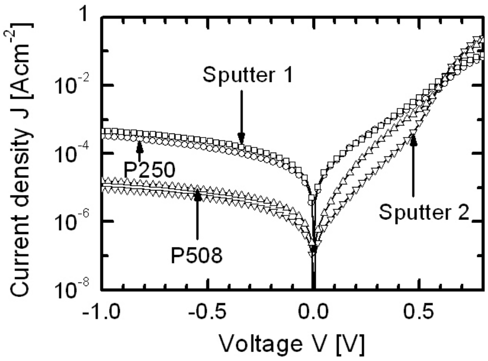

Fig. 5.7: The P250 and Sputter 1 cells exhibit low parallel resistance values of $r_p \approx 3\ k\Omega\text{cm}^2$, as well as remarkably low slopes in the forward voltage region without the standard J_{01}, J_{02} and r_s region in the curve being distinguishable. The P508 curve exhibits a significantly higher $r_p \approx 100\ k\Omega\text{cm}^2$. In the forward region a pronounced upward hump is noticeable. The parallel resistance of the Sputter 2 cell is comparable to the P508 cell. In the forward region its curve only shows a slight upward curvature at low positive voltages.

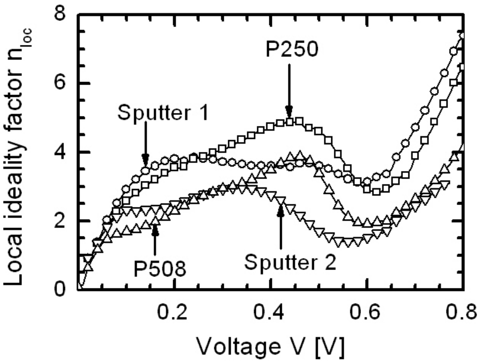

Fig. 5.8: The local ideality factors reflect the different values for the cells' fill factor. The Sputter 1 cell reaches values of $n_{loc} = 4$ at $V = 0.2$ V and never drops below $n_{loc} < 3$ from there on. The P250 cell even reaches $n_{loc} = 5$ at $V = 0.45$ V. The P508 cell also goes up to $n_{loc} = 4$, however only at $V = 0.45$ V. The Sputter 2 cell exhibits the lowest ideality factor. The value of n_{loc} is directly linked to the measured Fill Factors.

which the solar cells with laser doped emitter suffer. As mentioned in chapter 4.6 an optimization of the energy density profile inside the laser focus is necessary to achieve a more homogeneous doping and therefore a better solar cell performance. The latest results from Eisele and Röder [4] impressively show that a careful tailoring of the beam profile enables solar cell efficiencies exceeding $\eta = 18$ %. At the same time, however, their results show the sensitivity of the process towards fluctuations in the energy density profile.

Tab. 5.2: A detailed characterization of the cells from Figs. 5.7 and 5.8 shows that the main reason for the low Fill Factors of the P250 and Sputter 1 cells is their high ideality factors, which cause $FF_{0,n} < 70$ %. Additionally, their $\rho_s > 200$ Ω/ cause increased series resistances, which further reduce FF. For the Sputter 2 cell the main reduction in Fill Factor stems from the series resistance. For the P508 cell, both ideality and series resistance have an approximately equal share in reducing FF. Due to the good agreement of measured and calculated FF the use of $n_{loc,min}$ in the estimation seems justified.

Sample	r_s [Ωcm^2]	r_p [Ωcm^2]	$n_{loc,min}$	$FF_{0,n}$ [%]	FF_p [%]	FF_{meas} [%]
P250	2.50	3.8×10^3	2.65	67.9	58.2	59.8
Sputter 1	2.45	2.6×10^3	3.0	64.3	55.8	60.2
P508	2.14	6.4×10^4	1.7	75.4	66.5	68.1
Sputter 2	1.22	1.0×10^5	1.2	80.7	75.6	75.9

5.3 Aluminium

5.3.1 Experimental

For the characterization of Aluminium as a doping precursor evaporated layers with thicknesses $1\ nm < d_{Al} < 20$ nm are used. The substrate resistivity of the polished FZ wafers employed for the sheet resistance tests is $\rho > 5000$ Ωcm. An electron beam evaporation system deposits the aluminium layers onto the polished silicon surfaces. Subsequently to the coating the samples receive the laser irradiation with 0.8 Jcm^{-2} $< D_p <$ 2.3 Jcm^{-2} and $N_{melt} = 2$. Similar to the phosphorous precursors every substrate carries a number of individual areas irradiated with different laser parameters. After the laser irradiation the residual Al is removed by a dip in either NaOH or HF and the sheet resistance is measured. For the fabrication of solar cells n-type, polished Cz wafers with 0.5 Ωcm $< \rho <$ 3 Ωcm and a thickness $w = 300$ μm and n-type, polished FZ wafers with 100 Ωcm $< \rho <$ 300 Ωcm are used. The aluminium is coated onto the polished side, whereas the etched back side receives an n$^+$ laser doped phosphorous back surface field. The BSF is necessary to enable the formation of an ohmic back contact on the n-type substrates. After the formation of the emitter and the BSF the precursor residues are removed by an HF-dip and the samples are subsequently cleaned by a full RCA cycle. Subsequently the Cz cells receive an evaporated aluminium grid, defined by a shadow mask as front electrode, followed by a SiN_x antireflection layer. The FZ cells are immediately passivated by a thin a-Si:H layer, with the front contact being deposited afterwards. To achieve a contact to the emitter the "aluminium induced crystallization" [114] is exploited by annealing the FZ samples at $T = 220\ °C$ for $t = 30$ min. The back electrode for both samples consists of an evaporated Ti-Pd-Ag layer.

5.3.2 Sheet Resistance

Figure 5.9 exhibits the measured sheet resistance versus laser pulse energy density for five different aluminium layer thicknesses $1\ nm < d_{Al} < 20$ nm and $N_{melt} = 2$. The sheet resistance values cover almost two orders of magnitude between the minimum $\rho_s \approx 40\ \Omega/$ for $d_{Al} = 20$ nm and $D_p = 0.8$ Jcm^{-2} and the maximum $\rho_s > 1000\ \Omega/$ for $d_{Al} = 1$ nm and $D_p = 1.1$ Jcm^{-2}. For all layer thicknesses except $d_{Al} = 1$ nm the sheet resistance behavior for the aluminium precursors is completely different than for the phosphorous precursors. Instead of decreasing ρ_s with rising D_p the sheet resistance values stay rather constant in the case of $d_{Al} = 3$ and 5 nm, and even tend upwards for the thicker precursor layers. Only for $d_{Al} = 1\ nm$ a decreasing sheet resistance for higher pulse energy density is observable. The lowest value for ρ_s is achieved with the lowest D_p and the highest d_{Al}.

5.3.3 Doping profiles

The unexpected behavior of the sheet resistance indicates that the doping mechanism is partly different for aluminium than for phosphorous. While the increase of the precursor thickness for both materials leads to lower sheet resistances, the increase in pulse energy density in the case of Al does not decrease the sheet resistance. In order to gain more insight into the doping mechanism for aluminium, the doping profiles of selected samples are determined by SIMS. Figure 5.10 depicts the profiles for $d_{Al} = 5$ and 20 nm at pulse energy density $D_p = 1.3$ Jcm^{-2}. Clearly the maximum doping concentration rises from $C_s = 1 \times 10^{21}$ cm^{-3} to $C_s = 3 \times 10^{21}$ cm^{-3} with d_{Al} increasing from 5 to 20 nm. Also the shape of the curves is different. Whereas the profile for the thinner layer exhibits a slight "kink" at $z \approx 30$ nm, the thicker layer exhibits a rather Gaussian shape and a slightly higher emitter depth of $d_e \approx 200$ nm. Only very close to the surface, a small kink is visible in the profile of $d_{Al} = 20$ nm. The succession of the two profiles is in accordance with the measured sheet resistances. However, their scaling factors strongly differ as $A = 0.46$

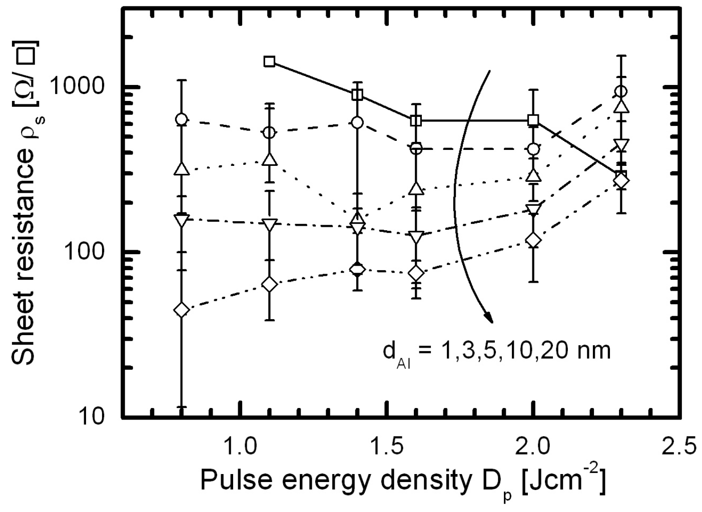

Fig. 5.9: The sheet resistance of aluminium doping precursors is strongly dependent on the thickness of the dopant layer, as well as the laser pulse energy density. In all cases a higher d_{Al} leads to a decrease in the measured sheet resistance to a minimum $\rho_s \approx 40\ \Omega/$ at $d_{Al} = 20$ nm and $D_p = 0.8$ Jcm^{-2}. Unlike in the case of phosphorous, increasing laser power does not lead to lower but to higher or virtually constant sheet resistance values. Only for $d_{Al} = 1$ nm layers, ρ_s likewise decreases with mounting D_p.

for $d_{Al} = 5\ nm$ compared to $A = 0.12$ for $d_{Al} = 20$ nm. An interesting observation is found in figure 5.11, which presents the aluminium profiles for $D_p = 1.3$ and 2.5 Jcm^{-2} for $d_{Al} = 5$ nm. This time both profiles exhibit a kink, which is even more pronounced for the higher pulse energy density. This kink is possibly due to the segregation coefficient k_{Al} of aluminium. As reported e.g. by Wood [85], $k_{Al} < 1$ for recrystallization velocities $v_{cryst} < 10$ m/s, which also occur during laser doping. Thus, the kink formation probably points to a segregation of aluminium close to the surface.

Although the higher pulse energy density leads to an increased surface concentration as well as an almost doubled profile depth $d_e \approx 400$ nm, the measured sheet resistance at the same time increases from $\rho_s \approx 160\ \Omega/$ to $\rho_s \approx 750\ \Omega/$. The activation factors accordingly drop from $A = 0.46$ in the case of $d_{Al} = 5$ nm to $A = 0.15$ for $d_{Al} = 20$ nm.

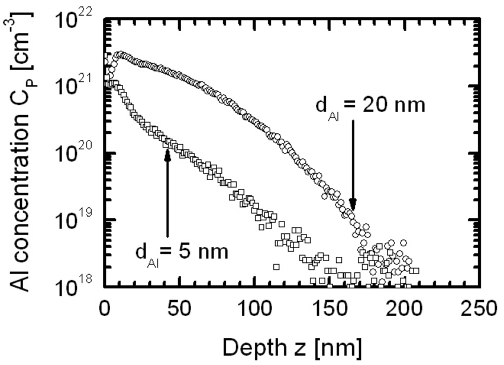

Fig. 5.10: An increase in the aluminium layer thickness from $d_{Al} = 5$ nm to $d_{Al} = 20$ nm leads to both increased surface concentration, as well as slightly higher doping depth. Also the shape of the doping profile changes from a "kink and tail" to a more Gaussian shape. Further the activation factor strongly decreases from $A = 0.46$ in the case of 5 nm precursor thickness to $A = 0.12$ for $d_{Al} = 20$ nm.

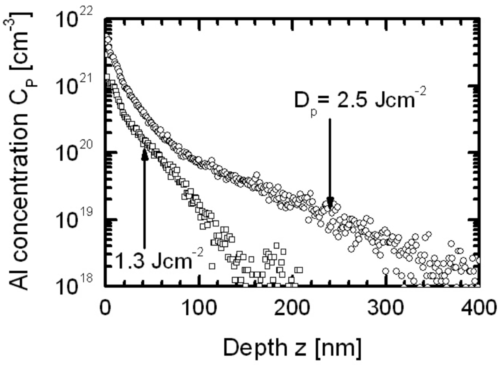

Fig. 5.11: Increasing the laser pulse energy density at a constant $d_{Al} = 5$ nm does not alter the shape of the profile. However, both maximum concentration as well as doping depth increase noticeably. This increase is in contrast to the simultaneous rise in the sheet resistance from $\rho_s \approx 160\ \Omega/$ to $\rho_s \approx 750\ \Omega/$. The activation factor is accordingly diminished from $A = 0.46$ to $A = 0.15$.

Obviously, the higher pulse energy densities indeed do lead to an increased incorporation of aluminium into the silicon. However, the incorporated Al is not electrically activated. Furthermore the higher D_p even leads to a decrease of electrical activation. Possibly a partial oxidation of the aluminium is the reason for the unexpected behavior of the sheet resistance. Higher pulse energy densities would likewise lead to an increased Al incorporation as well as a stronger Al oxidation due to the longer melting times. A different possibility is the above mentioned segregation, which could lead to the formation of some kind of electrically inactive clusters near the surface. However, segregation should be smaller for higher D_p, as they increase the recrystallization velocity. This, according to Ref. [85], should in turn increase k_{Al}, while the opposite behaviour seems to be the case here. A different, interesting observation is the extreme chemical resistance of the laser treated silicon surfaces.

5.3.4 Etch resistance

The abovementioned cleaning process easily removes the excess aluminium after laser irradiation by dipping the samples in NaOH or HF. After the dip a subsequent RCA step thoroughly cleans the samples. However, even after the complete RCA cycle the surfaces of the irradiated areas do remain hydrophilic. Even a prolonged exposition to HF ($t > 30$ min) does not remove the hydrophilic behavior. Experiments with different cleaning agents, as Piranha ($H_2SO_4 : H_2O_2$) do not have an effect on the behavior. Applying 60 % concentrated hot KOH ($T = 90$ °C) to specially fabricated test samples leads to the formation of interesting structures. These samples receive laser pulses with a spacing $\Delta y = 10$ μm, which is larger than the dimension of the individual pulse. Thus, there is no overlap between the pulses. The figures 5.12 and 5.13 show two SEM pictures of laser doped silicon samples etched for $t = 15$ min. The top view in figure 5.12 reveals a succession of highly parallel vertical trenches. The distance of the features is $x = 9.9$ μm, which matches the laser pulse distance of $\Delta y = 10$ μm in that experiment. Obviously there is a periodic succession of larger and smaller trenches. Figure 5.13 shows the same sample in a side view. The larger trenches reach a depth $z \approx 3.5$ μm, whereas the smaller ones only extend down to $z \approx 1.6$ μm. The arrangement of the laser pulses leads to the assumption that strong etching takes place between the pulses, as there is no doping of the silicon and therefore the KOH can etch the material. Inside the laser pulse strong Al doping takes place and obviously prevents the etching of the silicon. However, the doping concentration seems to be higher at the circumference of the pulse than in the very center, which would be an explanation for the smaller trench, which is visible there. However, a terminal conclusion for the mechanisms responsible for the interesting behavior, as well as the unexpected doping characteristics could not be obtained during the time of this thesis.

5.3.5 Solar Cells

In spite of the unclear status of the silicon surface after aluminium laser doping, a number of solar cells have been fabricated in order to assess the principal applicability of aluminium for emitter fabrication. Table 5.3 presents cell results for aluminium precursor thicknesses of $d_{Al} = 3$ and 10 nm and different values for D_p. The samples with $d_{Al} = 3$ nm are fabricated on Cz substrates with SiN_x ARC, while the samples with $d_{Al} = 10$ nm bear an $a - Si : H$ passivation layer. For the low

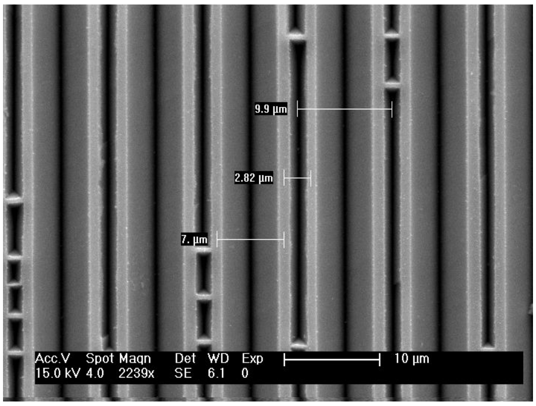

Fig. 5.12: An SEM top view onto an areas doped with single laser pulse irradiation of Al shows a periodic succession of trenches after 15 *min* etching in 60 % KOH at $T = 90\,^{\circ}$C. The periodicity matches the distance of the laser pulses $\Delta y = 10$ μm. Apparently different zones of high and low Al doping alternate, as the undoped silicon is being attacked by the etch, while doped silicon is not.

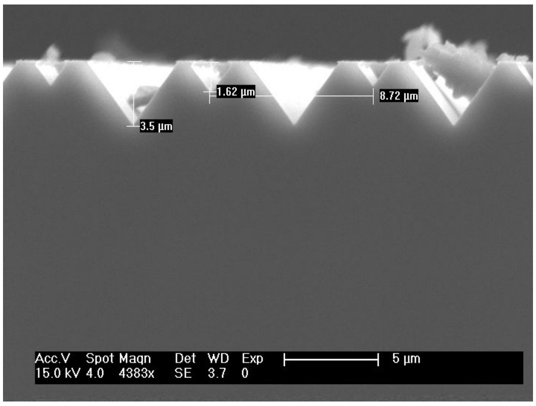

Fig. 5.13: An SEM side view on the same area reveals the trench depths after the etching. The large trenches extend down to $z \approx 3.5$ μm, whereas the small trenches only reach $z \approx 1.6$ μm.

precursor thickness an increase of the pulse energy density from $D_p = 1.2$ Jcm^{-2} to $D_p = 1.8$ Jcm^{-2} leads to a significant rise of the open circuit voltage from $V_{oc} = 418$ mV to $V_{oc} = 506$ mV. The impact on the other cell parameters remains within the measurement variation. The short circuit current densities $J_{sc} \approx 24$ mAcm^{-2} are rather low, as are the Fill Factors $FF \approx 64$ %. Each value represents the average of two solar cells. For $d_{Al} = 10$ nm altogether eight cells, consisting of a repeated series of four different pulse energy densities are averaged. The reason for this averaging is that no clear trend can be extracted from the individual results. Obviously the impact of the change in pulse energy density is smaller than the already existing variation in the experiment. The cells´ $V_{oc} = 547$ mV are higher than the ones for $d_{Al} = 3$ nm, possibly because the amorphous silicon providing some surface passivation. At the same time,k $J_{sc} = 17.3$ mAcm^{-2} is much lower than for the thinner precursor. One reason for that is the $a - Si : H$ passivation layer, which is not optimized as an antireflection coating and further strongly absorbs itself in the short wavelength range. Also the Fill Factors $FF = 49.5$ % are much lower than

Tab. 5.3: The solar cells fabricated from evaporated aluminium precursor layers with $d_{Al} = 3$ nm and 10 nm all exhibit rather poor results. While for $d_{Al} = 3$ nm an increase in D_p from $D_p = 1.2$ Jcm^{-2} to $D_p = 1.8$ Jcm^{-2} increases the open circuit voltage from $V_{oc} = 418$ mV to $V_{oc} = 506$ mV, no significant impact of a change in D_p is obvious for $d_{Al} = 10$ nm. Due to this reason the results for $d_{Al} = 10$ nm are averaged from two groups of four cells with four different values of D_p.

Sample	V_{oc} [mV]	J_{sc} [mAcm^{-2}]	FF[%]	η[%]
3 nm, 1.2 Jcm^{-2}	418 ± 8	23.9 ± 1	63.3 ± 2.6	5.7 ± 0.1
3 nm, 1.8 Jcm^{-2}	506 ± 22	24.4 ± 0.6	64.7 ± 2	7.3 ± 0.3
10 nm	547 ± 5	17.3 ± 1.3	49.5 ± 6.9	4.7 ± 1

for $d_{Al} = 3$ nm.

Even if the complete reason for such low solar cell performance is not clear, the results render the use of aluminium as a dopant for the formation of full area p-type emitters out of scope. The characterization of aluminium emitters in chapter 7 will show that the open circuit voltages are mainly limited by an extremely high recombination inside the aluminium emitter, which is partly caused by the high emitter doping concentration and probably also because of the inability to produce clean hydrophobic surfaces, which can be sufficiently passivated.

5.4 Chapter Summary

This survey proves the basic applicability of the three examined liquid and sputtered phosphorous precursors for the fabrication of solar cell emitters. The liquid precursors allow for an adjustment of the emitter sheet resistance down to $\rho_s \approx 150\ \Omega/$ by adapting the applied laser pulse energy density. Their doping profiles exhibit maximum concentration in the range 10^{19} cm^{-3} $< C_s <$ 10^{20} cm^{-3} and emitter depths of up to $d_e = 400$ nm. Sputtered phosphorous introduces the precursor layer thickness as additional parameter, thus allowing for the tuning of the doping profile and sheet resistance in an even wider range. Probably a change in the concentration of the doping liquids likewise enables an extension of the processing range. Further, Eisele [113] showed in a recent publication that also the laser pulse duration has a strong influence on the doping profiles, as already discussed in chapter 2. Longer laser pulses accordingly lead to a deeper and more lowly doped emitter.

The solar cells fabricated, unfortunately, all suffer from emitter inhomogeneities introduced by the laser process. Therefore, the full potential of the technology could not be exploited within the scope of this thesis. However, recently the efficiency of laser doped solar cells with sputtered phosphorous precursors was increased to $\eta > 18$ %, proving the high quality of suchlike produced emitters [72].

Regarding only the sheet resistance, the aluminium precursor is also capable to produce emitters with doping levels suited for solar cells. However, the dependence of the sheet resistance on the employed laser pulse energy density is completely different than for the phosphorous precursors, as the aluminium emitters mainly exhibit an increasing sheet resistance with rising laser power. A comparison with doping profiles shows that the higher laser power indeed incorporates more Al into the silicon, but at the same time renders more of the dopant electrically inactive. One possible explanation for the electrical inactivity is the formation of aluminium oxide inside the emitters. Such partial oxidation could also explain the exceptional etching resistance of the doped surfaces and the inability to reach a hydrophobic surface status necessary for passivation. Consequently the solar cell results with aluminium precursors are rather poor with maximum $V_{oc} \approx 550$ mV and $\eta \approx 7$ %.

The following chapter will close in on the influence of the laser irradiation on the silicon itself, while chapter 7 will return to laser diffused emitters. There the potential of these emitters will be assessed in general.

Chapter 6

Lifetime Reduction in Laser Irradiated Silicon

6.1 Introduction

Already in the early days of semiconductor laser processing several authors studied the effect of laser irradiation on the minority charge carrier lifetime or the operating parameters of silicon semiconductor devices. Deshmukh et.al. [115] examined the influence of pulsed ruby laser radiation on the quality of Si-SiO_2 interfaces. They found increased values of oxide charge and interface state density upon the irradiation, already starting from pulse energy densities as low as $D_p = 0.5$ Jcm^{-2}, using a rather large laser spot of approximately 6 mm in diameter. Further, they mentioned evidence of conductivity type conversion from p- to n-type in some samples after the laser treatment, as well as the recovery of the minority carrier lifetime after a thermal treatment. Parker et.al. [116, 117] used the fundamental and frequency doubled output of an Nd:YAG laser for irradiating bipolar transistors, diodes and MOS-capacitors, and studied the evolution of leakage currents or storage times. In contrast to the the work of Deshmukh et.al., their focus size was only approximately 10 μm in diameter. Also in their experiments a strongly detrimental impact of the laser treatment on the device parameters became evident. Similarly to Deshmukh et.al., the device properties recovered after thermal annealing. However, none of these studies could unambiguously identify the mechanism, which is responsible for the changes in device parameters.

In contrast to the previous studies, the laser focus of the *ipe* laser doping process has a strongly elliptical or line shape, which Köhler et.al. [3] showed to be beneficial for the crystal quality in the recrystallized zone. They compared samples irradiated with a circular beam of approximately 50 μm diameter, to others treated with the line shape focus by Transmission Electron Microscopy (TEM). The former samples showed visible dislocations, whereas the latter samples appeared to be defect free, within the detection limits of the TEM. In spite of the findings of Köhler et.al., in samples irradiated with a line focus still minority carrier lifetime degradation is observed. This chapter tries to shed some light on the reasons.

For doing so, this chapter examines silicon, which is laser irradiated without any doping precursors, displaying the dependency of the effective minority carrier lifetime τ_{eff} on the irradiation parameters. It then discusses possible reasons for the lifetime decrease, using the results from surface texture measurements, etch experiments, Secondary Ion Mass Spectrometry (SIMS), Fourier Transformed Infrared (FTIR) spectroscopy, Photoluminescence (PL), X-Ray Topography (XT) and Electrochemical Capacitance Voltage (ECV) measurements, as well as thermal annealing experiments. The results from this thorough characterization point to impurities, incorporated due to the laser irradiation, being responsible for the lifetime reduction. At the end of the chapter, a simple model for estimating the local lifetime inside the laser affected layer at the silicon surface is presented.

6.2 Dependency of Carrier Lifetime on Laser Irradiation Parameters

6.2.1 Sample preparation

High quality Float Zone (FZ) p-type silicon wafers with diameter $d = 100$ mm and doping concentrations 7.2×10^{13} cm^{-3} $< N_A < 1.5 \times 10^{16}$ cm^{-3} and a set of lowly doped FZ n-type samples serve for investigating the effects of laser irradiation on the minority carrier lifetime. Table 6.1 displays the characteristics and laser parameters of all samples. Every sample carries three different irradiation parameters on three quarters, while one quarter remains unprocessed for reference. Not all samples have equally polished front and back surfaces. Therefore, only samples from series A and E are irradiated on both sides. After the laser process, they undergo a standard RCA cleaning prior to the deposition of a high quality silicon nitride passivation layer on the front and back surface. In all other series, the back surface is passivated before the laser treatment on the front side. Afterwards they similarly undergo the cleaning

Tab. 6.1: Different laser pulse energy densities as well as number of melt cycles allow for a thorough characterization of their influence on the minority carrier lifetime. Further, using different wafer types and resistivities resolves possible dependencies of bulk material on the laser impact.

Series	Wafer Type	Doping Concentration	Thickness	Parameter	Process
A	p-type	1.5×10^{16} cm^{-3}	300μm	N_{melt}	double
B	p-type	5×10^{15} cm^{-3}	300μm	N_{melt}	single
C	p-type	2.2×10^{15} cm^{-3}	525μm	N_{melt}	single
D	p-type	7.2×10^{13} cm^{-3}	525μm	N_{melt}	single
E	p-type	1.5×10^{16} cm^{-3}	300μm	N_{melt}	double
F	p-type	1.5×10^{16} cm^{-3}	300μm	D_p	single
G	n-type	2×10^{12} cm^{-3}	500μm	D_p	single

and front side passivation, before being cleaved into quarters and measured by Quasi Steady State Photoconductive Decay (QSSPC).

6.2.2 Variation of the Laser Pulse Energy Density

The most important parameter for laser doping is the pulse energy density D_p, as it determines the depth of the molten layer. Thus it sets a fixed limit for the diffusion process. The experiment to assess the influence of D_p on τ_{eff} comprises the sets F and G. Figures 6.1 and 6.2 depict the injection dependent effective minority carrier lifetime for various laser pulse energy densities. All samples in these two series feature an equal number of melt repetitions $N_{melt} = 2$.

Both series similarly show a reduction of τ_{eff} with increasing pulse energy density $0 < D_p < 2.8$ Jcm^{-2}. However, two reduction steps can be identified for both sample materials. For $D_p < 2.4$ Jcm^{-2} (Series F) or $D_p < 2.1$ Jcm^{-2} (Series G) the reduction is noticeable but not pronounced, diminishing the lifetime from reference values of $\tau_{eff} \approx 500$ μs or 9000 μs to $\tau_{eff} \approx 250$ μs and 5000 μs, for p-type and n-type material respectively. For both series the lifetime reduction is almost perfectly monotonic with increasing D_p. The last increase of D_p in both series leads to a significantly stronger lifetime reduction down to $\tau_{eff} \approx 100$ μs and 30 μs. Inspecting the surface of these samples after irradiation shows that the last increase in pulse energy density exceeds the threshold for silicon evaporation. Figure 6.3 depicts an SEM micrograph

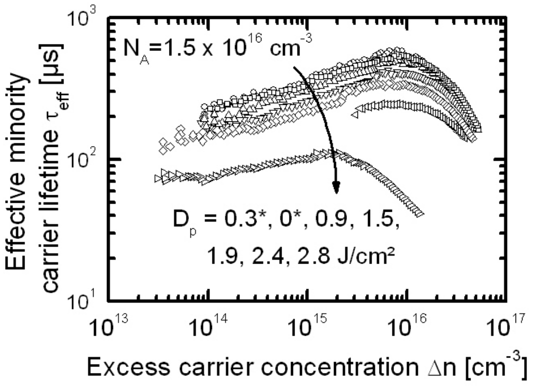

Fig. 6.1: The samples with $N_A = 1.5 \times 10^{16}$ cm^{-3} show a monotonous degradation from $\tau_{eff} \approx 500$ μs for the untreated reference to $\tau_{eff} \approx 100$ μs for the maximum energy density. Apparent is a rather gentle decrease of the lifetime for the lower values of D_p and a large step for the maximum value. Surface destruction due to the exceeding of the evaporation threshold is the reason for this step.

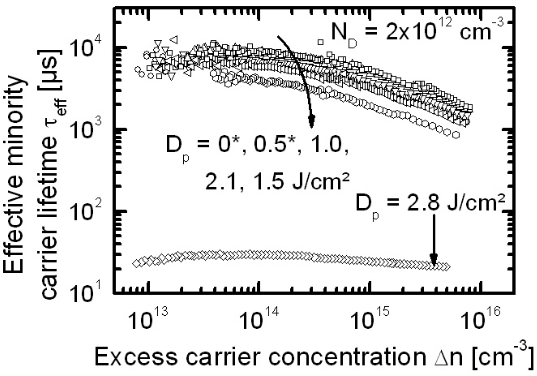

Fig. 6.2: The behaviour of figure 6.1 is even more pronounced for the n-type sample with $N_D = 2 \times 10^{12}$ cm^{-3}. For lower energy densities the lifetime slowly degrades from $\tau_{eff} \approx 9000$ μs for the untreated reference to $\tau_{eff} \approx 5000$ μs for $D_p = 1.4$ Jcm^{-2}. A further increase of D_p leads to a complete lifetime breakdown to $\tau_{eff} \approx 30$ μs. Again, surface evaporation of Si is the cause.

of a silicon surface, irradiated with $D_p = 2.8$ Jcm^{-2}, showing strong damage. Most likely this surface damage coincides with a strongly increased surface recombination, which is in turn responsible for the abrupt breakdown of carrier lifetimes.

6.2.3 Variation of the Number of Melting Cycles

The sample sets A to D serve for evaluating the influence of N_{melt} on τ_{eff}. All samples are irradiated with $D_p = 1.5$ Jcm^{-2} and $1 < N_{melt} < 20$. Figure 6.4 exemplarily presents the measured effective minority carrier lifetime of sample set A. The maximum lifetime decreases from $\tau_{eff} \approx 500$ μs for the not irradiated reference to $\tau_{eff} \approx 70$ μs for $N_{melt} = 20$.

The degradation is not perfectly monotonous, as the curves for 1 and 2 melt cycles are interchanged. Figure 6.5 combines the maximum measured lifetimes versus the

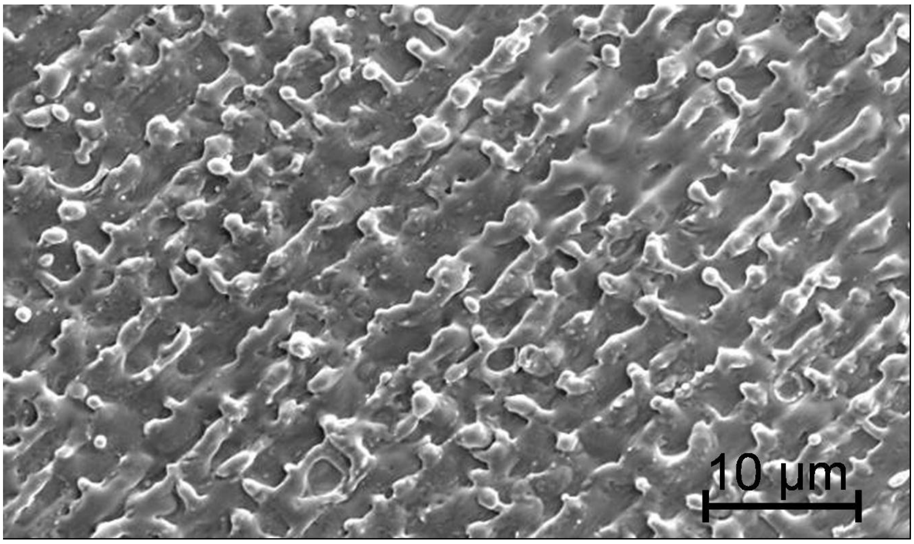

Fig. 6.3: Irradiation with $D_p = 2.8$ Jcm^{-2} and $N_{melt} = 2$ induces strong damage to the silicon surface. The elongated structures show clear melting and even the ejection of molten material. Most probably, the damage coincides with an increase of the surface recombination velocity.

number of melting cycles for the sets A to D. Whereas the absolute lifetime values increase from $\tau_{eff} \approx 500$ μs for the most highly doped samples of series A to a remarkably high $\tau_{eff} > 20$ ms for the lowest doped samples of series D, the relative trend of decreasing effective lifetime with increasing N_{melt} is similar. All sets show a virtually monotonous reduction of the measured effective carrier lifetimes with N_{melt} increasing from 1 to 20. There indeed exist exceptions from the strictly monotonic behavior for the 1.5×10^{16} cm^{-3} and the 2.2×10^{15} cm^{-3} doped sample. Also for $N_A = 7.2 \times 10^{13}$ cm^{-3} the decrease does not strictly follow the succession of melt repetitions. However these exceptions do not contradict the general conclusion that a higher number of melting cylces corresponds to a stronger reduction of carrier lifetime. In fact it is likely that the deviations are due to fluctuations in the surface passivation quality of the silicon nitride, as not all samples of each sample set could be coated in one deposition run. Above all the high resistivity wafers of series D, exhibiting $\tau_{eff} > 20$ ms are very sensitive to small changes in the surface passivation quality. Considering e.g. the maximum reference $\tau_{eff} = 24.2$ ms of series D a surface recombination velocity of $S_{eff} = 1.1$ cms^{-1} can be calculated according to Eq. (2.32). A subtle increase of S_{eff} to e.g. 1.5 cms^{-1} would already lead to $\tau_{eff} = 17.5$ ms.

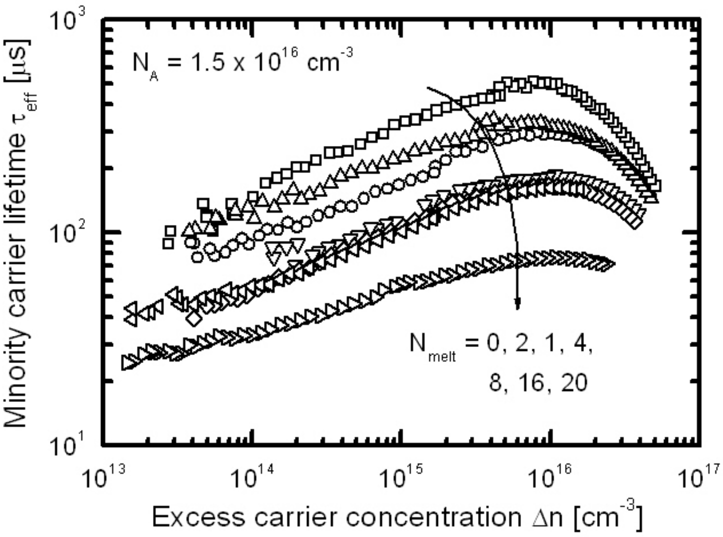

Fig. 6.4: For the samples with $N_A = 1.5 \times 10^{16}$ cm^{-3} the maximum minority carrier lifetimes degrade from $\tau_{eff} \approx 500$ μs for the untreated reference to $\tau_{eff} \approx 80$ μs for $N_{melt} = 20$.

Rating. The data presented in the preceding section show that both, increasing pulse energy density as well as higher melt repetitions degrade the minority carrier lifetime of samples, regardless of dopant type or concentration. As the laser only melts a several hundred nm thin layer at the silicon surface, it is most probable, that the measured impact on τ_{eff} originates from this laser affected layer. In older studies, minority carrier lifetimes as low as $\tau_{eff} = 10$ ns were determined from the measured parameters of laser irradiated devices [116]. In this thesis only the effective lifetime of whole samples and not a localized minority carrier lifetime is directly accessible, which makes the characterization of the observed effects more cumbersome. However, the remainder of this chapter will show that indeed the surface layer limits the effective lifetime.

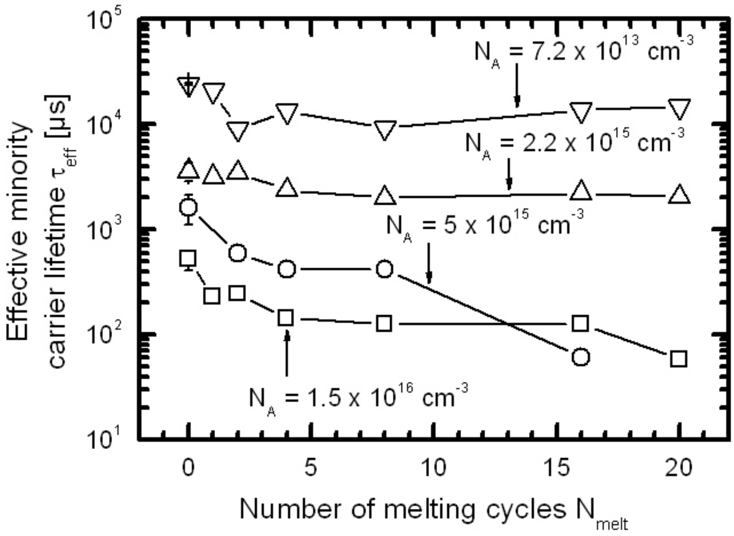

Fig. 6.5: The comparison of sample sets A to D shows that the general trend of decreasing effective carrier lifetime with higher N_{melt} is independent of the sample doping concentration. The reference lifetime values rise from $\tau_{eff} \approx 500\ \mu$s to $\tau_{eff} \approx 24$ ms from the highest to the lowest sample doping concentration. The values of τ_{eff} do not for all curves follow the succession of increasing melt cycles monotonously. The deviations from the strict monotony are due to fluctuations in the surface passivation quality.

6.3 Localizing the Origin of Laser Induced Lifetime Decrease

In principle, four different possibilities exist for an introduction of defects by the laser irradiation:

A) Bulk defects. Theoretically, albeit improbable, an introduction of defects into the bulk due to the extremely high temperature gradients needs to be considered. If this was the case then the measured lifetimes would still be low after a removal of the laser affected layer.

B) Surface Recombination. The laser induced melting and recrystallization strongly affects the silicon surface. Thus, an increase in the surface area by the creation of a texture, or an increase in the surface trap density D_{it} are possible. Both effects would cause higher surface recombination. The changes in surface area are monitored by profilometry measurements. An etching experiment assesses D_{it}: If an increase in D_{it} was the main reason for the degraded lifetimes, then removing only a few nm from the actual surface should suffice to restore τ_{eff} to reference values.

C) Distributed Defects inside the laser treated surface layer. The investigations in [3] did reveal no crystal defects above the detection limit of TEM inside the laser irradiated layers. Still, a smaller density of crystal defects, which are not detectable by TEM could be present. For example [116] suggested that the radiation leads to the formation of point defects inside the processed layers. Another possibility is the incorporation of unwanted impurities during the irradiation. Again, an etching experiments tests this assumption: If the defects were distributed inside the molten layer, a gradual increase of the lifetime would be expected for gradual etching of this layer.

D) Defects localized at the interface between recrystallized layer and bulk. A localized, high density of defects could be localized at the interface between the recrystallized layer and the unmolten bulk of the samples. If the defects were concentrated at the interface between substrate and recrystallized zone, a step-like lifetime increase should occur when this interface is removed by etching.
In order to pin down the laser induced defects, the experiments presented in the following sections step by step will examine these four different recombination mechanisms.

6.3.1 Increase in Surface Area

From the overview in chapter 4 we know that laser melted silicon recrystallizes epitaxially on the substrate. Still, after the process a slight surface texture is observable, as seen in Figs. 4.5 and 4.6. This texture indicates that a certain material displacement takes place. The formation of a surface texture implies an increase in the surface area. If this increase were significant, it could be a reason for the observed reduction in carrier lifetimes, as a higher surface area increases the Surface Recombination Velocity (SRV). Figure 6.6 shows an SEM closeup on single laser pulses, scanned on a bare, polished substrate. It seems that a portion of silicon

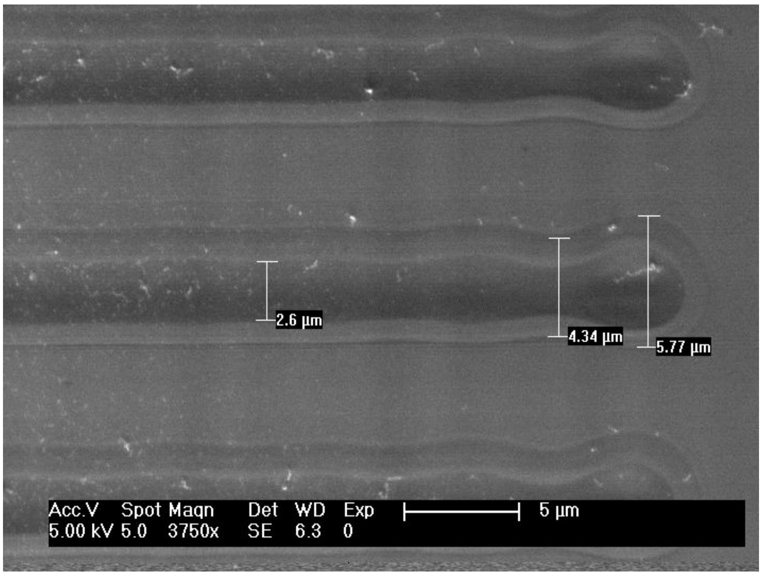

Fig. 6.6: The irradiated single pulses exhibit a distinct surface structure. Apparently the inner part of the pulse is lowered, whereas the outer part is elevated. The total width of the structure is approximately 5 μm.

has been transported from the center to the sides of the pulse, forming a kind of perimeter wall there. The center area seems lowered, compared to the outer ring. The sharp cutoff at the right side of the pulse results from the adjustable slit that blocked the outer parts of the laser beam during the irradiation. Figure 6.7 shows a surface topogramm of a single pulse recorded with a DekTak stylus profilometer. Actually the silicon is accumulated at the edge of the laserpulse while some material is removed from the center. The height of the outer accumulated "wall" is approximately 15 nm, the depth of the inner "valley" approximately 30 nm, the total width of the structure is approximately 5 μm.

The question arises how large the increase in surface area ΔA_s caused by the laser texture is, relative to the planar surface before the laser treatment. Due to the line shape of the laser focus, a two-dimensional consideration is sufficient for an estimate of the surface increase. Figure 6.8 depicts a scan of a surface, irradiated with typical parameters of $D_p = 2$ Jcm^{-2} and a pulse spacing $\Delta y = 3$ μm. Spacing the pulses closely together results in a periodic surface texture. For the parameters used in this case, the texture has a triangular shape with a height of $h_s \approx 10$nm and a base length equal to Δy. Calculating the relative surface increase ΔA_s created by the irradiation by approximating the surface with a series of triangles yields

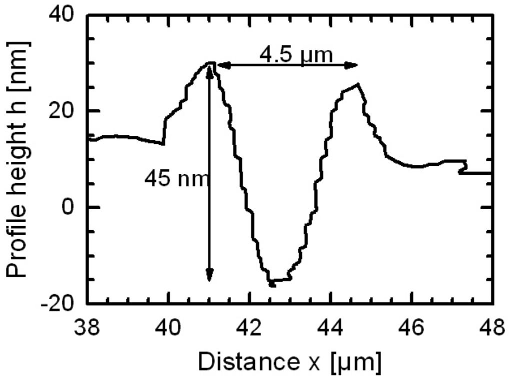

Fig. 6.7: Profilometry measurements of irradiated single pulses confirm the impression from the SEM image. In the center of the pulse an approximately 35 *nm* deep valley forms, whereas the perimeter is elevated approximately 25 *nm* high. The total width is 5 *µm*.

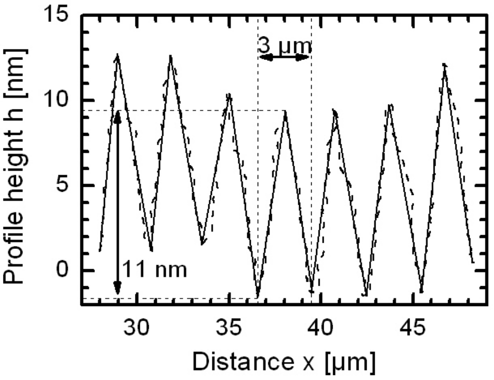

Fig. 6.8: Irradiation with $D_p = 2\ Jcm^{-2}$ and a pulse spacing of $\Delta y = 3\ \mu m$ results in a triangular surface structure with a base length of Δy and a height $h_s \approx 10\ nm$. The solid lines represent a linear approximation to the dashed measurement data. The relative surface increase due to laser irradiation $\Delta A_s < 0.003\ \%$, which is completely negligible. Calculated using the linear approximation.

$\Delta A_s < 0.003\ \%$. This value is completely neglegible. With increasing laser pulse energy density, the dimensions of the surface texture grow larger, reaching the µm-scale when the surface exceeds evaporation temperature. In turn, the electronical quality of the surface strongly degrades, as described in the next chapter. However, such high values for D_p are far above the processing window for fabricating high quality laser emitters. Thus, for typical laser doping parameters, the increase of surface area due to the laser induced texture is too small to influence the surface recombination velocity. However, an increased interface state density due to the irradiation could still lead to a higher SRV.

6.3.2 Surface removal by etching

The laser melted zone extends some 100 nm deep into the silicon bulk. If the defects were localized solely at the surface or inside the recrystallized layer, the lifetime of irradiated sample should completely recover with this layer removed. Figure 6.9 shows the effective lifetime versus the excess carrier density for 1 Ωcm samples irradiated with different N_{melt} at a laser fluence $D_p = 2.7$ Jcm^{-2}. The lifetimes rapidly drop from $\tau_{eff} \approx 500$ μs without laser treatment to $\tau_{eff} \approx 2$ μs for $N_{melt} = 20$. Clearly a high number of melt repetitions in conjunction with a high pulse energy density is most detrimental for the material. After removing approximately 3 μm of the sample surface in a 60 % KOH solution at $T = 60$ °C, RCA cleaning and re-passivating the samples, the picture drastically changes. Figure 6.10 shows that the carrier lifetime of the irradiated samples is completely restored to values at least equal to the not irradiated references. Further, there is no correspondence to the sample history any more. The fluctuations in the absolute carrier lifetime of the samples are due to variations in the surface passivation quality, as the samples are coated in several runs with the passivation layers. These findings confirm that there is no modification of the bulk properties due to the irradiation.

Figure 6.11 depicts the results of a second etch experiment. There, samples processed equally with $D_p = 1.5$ Jcm^{-2} and $N_{melt} = 2$ and 14 are etched for different durations in 60 % KOH solution at $T = 20$ °C. At this temperature, the etch rate of the solution is low [118], thus enabling a controlled removal of thin layers of silicon. A preliminary experiment determines the etch rate to $R_{etch} = 17$ nmmin^{-1}. Thus, the etch depth d_{etch} in the experiment is determined via etching for different times, taking into accout a depth uncertainty of $\Delta d_{etch} \approx \pm 20$ nm. There is significant spread in the lifetime data because the samples are etched individually. However, for both melt repetitions there is a clearly monotonic increase in the effective lifetime with increased removal of the irradiated layer. For $N_{melt} = 14$ the lifetimes recover to the reference values for etch depths $d_{etch} > 300$ nm approximately. This depth corresponds to the melting depth for this laser fluence. For $N_{melt} = 2$ only three samples were processed. Thus, the depth at which the reference lifetime is reached cannot be resolved. Still a similar increase of τ_{eff} with d_{etch} is obvious.

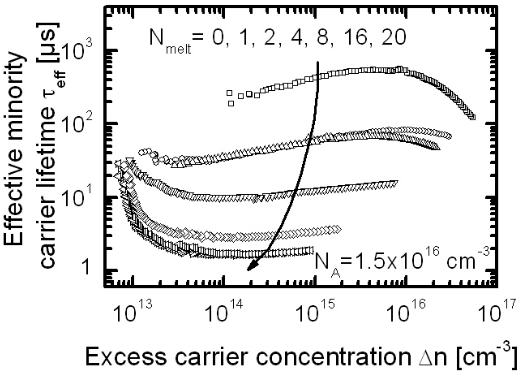

Fig. 6.9: Irradiation with a high laser fluence of $D_p = 2.7$ Jcm^{-2} rapidly degrades the effective carrier lifetime of the samples from $\tau_{eff} \approx 500$ μm down to $\tau_{eff} \approx 2$ μm.

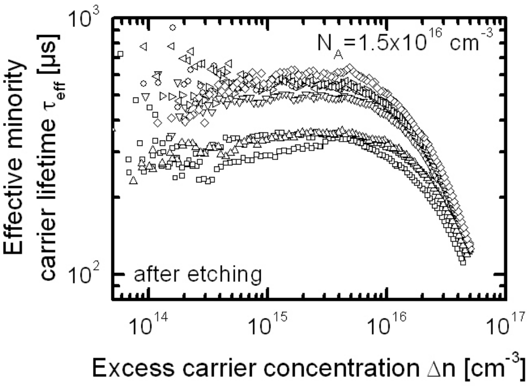

Fig. 6.10: After removing an approximately 3 μm thick surfacial layer and applying a new passivation, the lifetime of all processed samples completely recovers to values of 300 μs< τ_{eff} < 600 μs. Additionally any reference to the irradiation parameters is removed.

6.3.3 Result - Distributed Defects

The results of chapter 6.3.2 show that the laser induced recombination extends throughout the melted and recrystallized layer and is not located neither at the surface nor at the interface to the bulk alone, as there is a gradual increase of the effective lifetimes and no sudden changes. The data for $N_{melt} = 14$ in Fig. 6.11 indicate a linear increase of the effective lifetime with etch depth, as would be expected for a homogeneous distribution of the defects inside the laser affected layer.

6.4 Identifying the Origin for Laser Induced Lifetime Decrease

6.4.1 Excluding structural defects

Obviously the laser induced recombination centers are distributed throughout the surface layer. Still, we do not know, which process is responsible for the measured

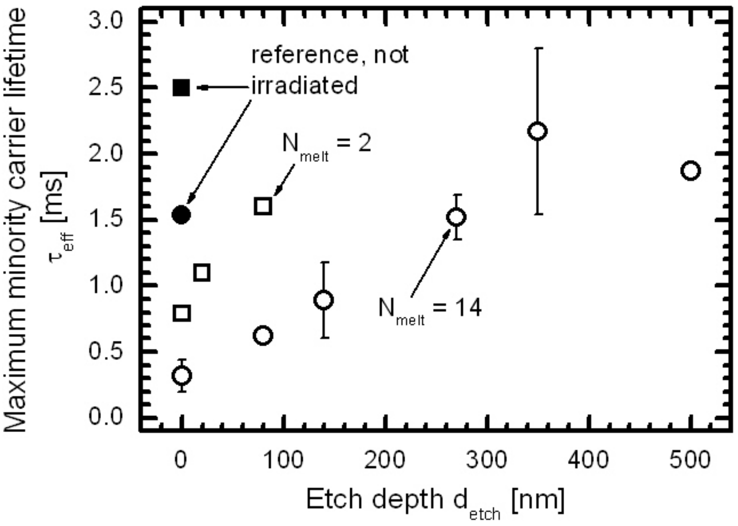

Fig. 6.11: A stepwise removal of the surface of irradiated p-type samples gradually increases the maximum effective carrier lifetime from $\tau_{eff} = 320\ \mu$s and 790 μs to $\tau_{eff} > 2$ ms and $\tau_{eff} = 1.6$ ms, respectively, for $N_{melt} = 14$ and 2. For the former series, etching approximately 300 nm restores the reference values, indicating that the recrystallized zone is completely removed.

decrease in lifetimes. In spite of the TEM characterization showing no signs of crystal defects [3], I perform additional investigation on the crystal structure, employing X-Ray Topography (XT) [119] and defect etching.

X-Ray Topography

Two regions with different laser parameters are prepared on a polished, 0.5 Ωcm Cz-wafer for XT characterization. They feature $N_{melt} = 20$ (area 1) and 2 (area 2) and an equal $D_p = 1.8$ Jcm^{-2}. Figure 6.12 shows the X-Ray topogram with the two areas marked with dashed lines[1]. Apart from a clearly visible, line shaped structure at the edges of the two regions, they do not show any signs of crystal strain fields. The slightly visible, periodic line pattern in area 2 results from the nm-sized surface texture produced by the scanned laser columns. The strain field at

---

[1] The measurements, performed by R. Köler, Humboldt Universität, Berlin, leading to the presented data, as well as the help with their interpretation, are greatly appreciated.

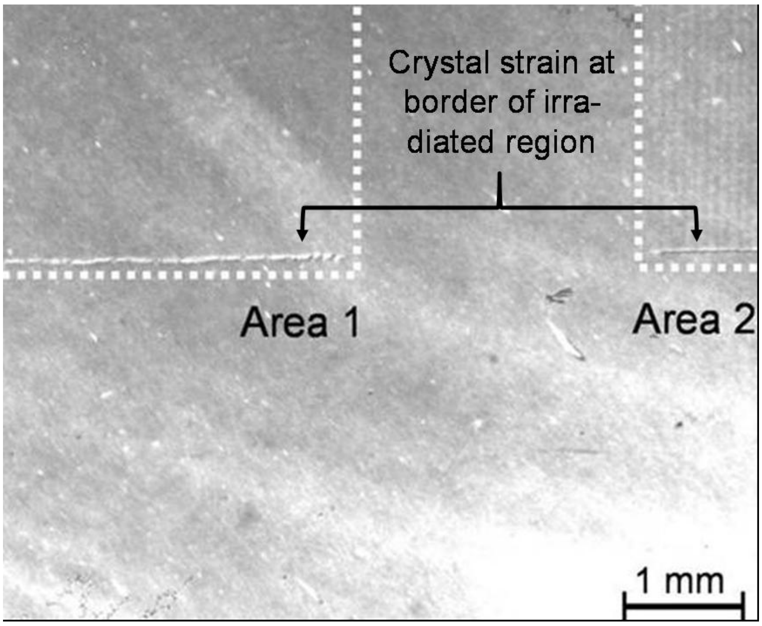

Fig. 6.12: X-Ray topography analysis does not reveal any crystal defects on areas, irradiated with $N_{melt} = 20$ (area 1) and 2 (area 2) respectively. Only at the border of the irradiated area a zone of increased crystal strain is visible. There the laser spot remains stationary for a longer time, as the xy-gantry motion v_{trans} reverses to scan the single columns. Consequently, the border region is hit by a strongly increased number of laser pulses, which cause the crystal strain. The randomly distributed speckles on the figure stem from imperfections of the photographic plate used for the characterization.

the edges results from a strongly increased number of melting cycles at these points. As explained in chapter 4.4.1 at the end of one column the y-translation v_{trans} stops, the sample advances by Δx and the scanning continues in the opposite direction. The translation movement by Δx is done at a velocity $v_x << v_{trans}$. Therefore, the number of melt repetitions at the border $N_{melt,x} >> N_{melt}$.

Defect Etching

Due to the resolution limit of the employed XT measurements, only defect structures larger than approximately 10 μm are detectable. Thus, in addition some samples are submitted to defect etching. After laser irradiation, a modified Schimmel etch solution, as described in [120], etches the irradiated areas up to a depth of approximately 200 nm. The samples are only partially immersed into the solution,

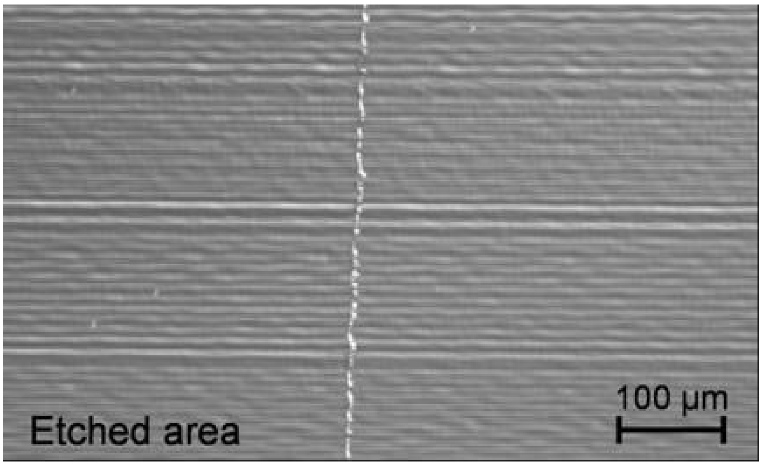

Fig. 6.13: Etching an irradiated silicon sample with a modified Schimmel solution does not reveal any crystallographic defects inside the etched part (left) in comparison to the not etched part (right). Only the laser induced surface texture is clearly visible.

allowing for an easy comparison of etched and not etched parts of the irradiated areas. Figure 6.13 displays one of the etched samples. In the middle, the boundary between etched (left) and not etched (right) areas is clearly visible. Similar to the XT-measurements, there is no evidence of crystallographic defects inside the irradiated area. Only the surface roughness induced by the pulsed laser melting is observed on both parts of the picture.

6.4.2 Assessing Impurity Incorporation

The findings of the last paragraph coroborate the absence of structural defects, as found by Köhler. This fact leads the search towards the possible effects of unwanted impurities taken up during the melting phase. There exist numerous studies dealing with the incorporation of impurities into silicon. Most of them are dedicated to dopant species, as the survey in chapter 4 shows. However, several publications also investigated species which are not classically used for doping in silicon, such as e.g. oxygen [121,122]. Both found strong oxygen doping of silicon due to pulsed Nd:YAG irradiation. However they disagreed on the mechanism responsible for the uptake. Hoh et.al. [121] found that the incorporation from the atmosphere could be blocked by a layer of thermal SiO_2 on top of the irradiated silicon. Consequently, they postulate the oxygen being supplied from the gas. In contrast to that, Mada [122] also measured oxygen uptake with a SiN_x capping layer on top of the silicon. In addition, electrical measurements showed that also an n-type doping of the silicon ocurred due to the oxygen uptake. Bentini et.al. [109] examined the incorporation of oxygen into gallium arsenide (GaAs) and silicon dependent on the oxygen pressure and the laser fluence. They found a strong incorporation of oxygen into GaAs, which was dependent on the oxygen pressure p. Thus, they concluded that the supply of oxygen was from the gas molecules impinging onto the sample surface while it was molten. For silicon they did not obtain reproducible results. In a later study [97] they observed the uptake of phosphorous from phosphorous chloride (PCl_3) vapour into silicon. Here, they differently suggested the adsorption of P at the surface as source for the doping. However the experiments in [109] were performed at a high pressure in the range of $1 \times 10^3 < p < 6 \times 10^3$ mbar whereas in the later experiments a region of $10^{-4} < p < 10^2$ mbar was examined.

Apparently different models exist regarding the formation of the impurity source in a laser doping process. The results presented in the following indicate that both, supply from the ambient gas as well as from a surface layer, contribute to the impurity source.

SIMS Characterization

Figure 6.14 depicts oxygen concentration profiles of p-type, FZ samples, irradiated on both sides with $D_p = 1.8$ Jcm^{-2} and $N_{melt} = 1,\ 4,\ 16,\ 64,\ 192$, measured by SIMS[2]. Clearly, a monotonous increase of the maximum O-concentration $C_{O,max}$, as well as the incorporation depth d_O is seen, when going to a higher number of melting cycles. The measured values range from 3×10^{18} cm^{-3} $< C_{O,max} < 2 \times 10^{19}$ cm^{-3} and 150 nm$< d_O <$ 400 nm respectively. The order of magnitude as well as the depth of the oxygen uptake approximately corresponds to the data presented in [121]. The rising $C_{O,max}$ and d_O suggest that a continuous supply of oxygen exists at the surface. With mounting N_{melt} the profiles approach a rectangular shape as more and more oxygen is stored inside the silicon. Starting from $N_{melt} = 16$ the maximum oxygen concentration seems to move from the surface into the laser treated layer. For the curves featuring 64 and 192 melt cylces $C_{O,max}$ exceeds the concentration close to the surface approximately by a factor of 2. The reason for this phenomenon is not clear. In principle, outdiffusion from a given impurity profile could give rise to a surface concentration, which is lower than the concentration inside the diffused

---

[2] The measurements were performed by G.Bilger, *ipe*, Universität Stuttgart. The support by performing the measurements and the aid in their interpretation is greatly appreciated.

layer. However, together with the outdiffusion also a loss of the total incorporated impurity amount would be expected. In the present case exactly the opposite is the case, namely a rising total amount of incorporated oxygen with a higher number of melting cycles. A different possibility would be a segregation coefficient k_O larger than unity for the incorporated oxygen. Yatsurugi et.al. [123] found a value of $k_O = 1.25$ for conventionally grown silicon. To the knowledge of the author there exist no values measured explicitly for laser induced oxygen incorporation. White et.al. [82], however, found for a number of other species the segregation coefficient always increased over the equlibrium value in the case of laser incorporation. So, $k_O > 1$ seems not unlikely in the actual case. The ultimate clarification of the processes associated with the impurity incorporation is, however, not subject of this thesis. Thus, only a simple, descriptive model will be developed in the remainder of this chapter.

Together with oxygen, the irradiated silicon layers also take up carbon (C) and

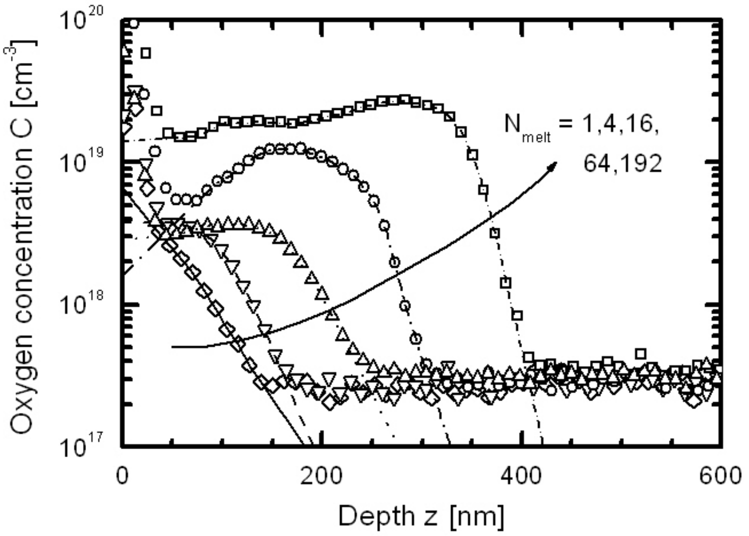

Fig. 6.14: SIMS measurements of the oxygen concentration incorporated during the irradiation of bare silicon wafers show a clear, monotonous increase of both maximum concentration and incorporation depth with higher N_{melt}. The lines represent extrapolations on the measured data (symbols) to correct for the augmented count rates at the surface and the background count rate.

nitrogen (N). This can be seen in figures 6.15 and 6.16, where the SIMS count rates of these three impurities are depicted in arbitrary units for p-type, FZ samples, irradiated with $D_p = 1.5$ Jcm^{-2} and $N_{melt} = 2,\ 16$. Arbitrary units are used in these figures, as no calibration standard was available for carbon and nitrogen. Similarly as in figure 6.14 the oxygen incorporation increases for higher N_{melt}, as does the incorporation of C and N. The profiles of all three impurities exhibit equal shapes. Apparently C, O and N follow the same incorporation mechanism.

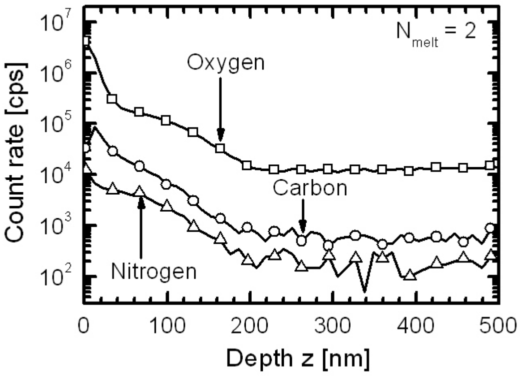

Fig. 6.15: SIMS analysis shows that oxygen, carbon and nitrogen are equally incorporated into FZ silicon, irradiated with $N_{melt} = 2$. The diffusion profiles of the impurities exhibit similar shapes and an incorporation depth $d_{in} \approx 200$ nm.

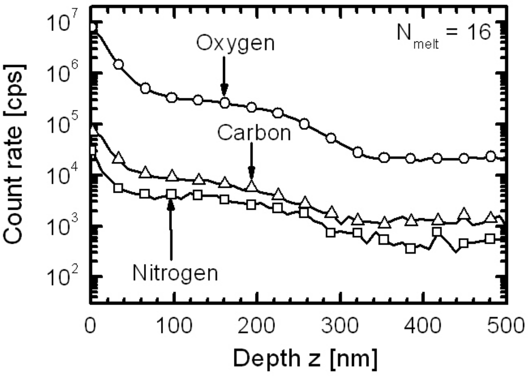

Fig. 6.16: SIMS profiles reveal that the irradiation with a higher $N_{melt} = 16$ increases d_{in} to approximately 350 nm in comparison to figure 6.15. The maximum count rates for O and N stay virtually constant, whereas there seems to be a decrease in the case of C. However, the exact separation of surface adsorbed oxygen from the actually incorporated oxygen is difficult for SIMS measurements.

This finding is in contrast to the results found by Berti et.al. [124], who investigated the incorporation of species from different gas ambients and did not find an uptake of N from an N_2 atmosphere. However, all their samples only received a single irradiation. They also postulated that the oxygen incorporated during laser irradiation forms a SiO_2 layer, up to 50 nm thickness on top of the silicon. The results presented above clearly contradict this observation, as there is no laser induced

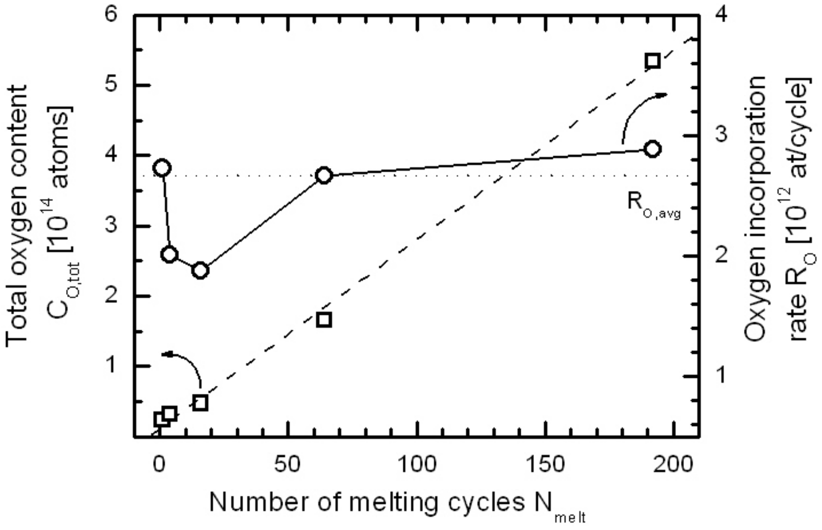

Fig. 6.17: The total amount of incorporated oxygen atoms linearly rises up to $N_O \approx 5 \times 10^{14}$ for $N_{melt} \approx 200$. A fit to the data yields an average incorporation rate of $R_{O,avg} = 2.68 \times 10^{12}$, while the rate determined from the individual data points ranges between $1.8 \times 10^{12} < R_O < 2.8 \times 10^{12}$.

oxide layer, but rather a diffusion of oxygen into the molten Si.

Incorporation mechanism From the SIMS measurements the absolute amount of incorporated oxygen atoms N_O with respect to the number of melting cycles can be determined. Figure 6.17 depicts N_O together with an incorporation rate R_O, calculated from the individual data points, as well as an average incorporation rate $R_{Ox,avg}$, calculated by fitting the data. Obviously N_O increases linearly with N_{melt}. The incorporation rate per melting cycle ranges between $1.8 \times 10^{12} < R_O < 2.8 \times 10^{12}$ atoms/cycle, with the average value $R_{O,avg} = 2.68 \times 10^{12}$ atoms/cycle. Apparently, for every melt cycle, an equal number of oxygen atoms is added to the already accumulated amount. Further, there seems to be no saturation behavior up to the approximately 200 melt cycles performed in this experiment. This, in turn, indicates a continuous supply of atoms. This supply could be a very thin oxide layer growing between two successive laser pulses. Alternatively, atoms striking the liquid silicon surface during a melting cycle could form the supply.

Using the kinetic theory of gases allows for an estimation of the number of atoms

N_{strike} striking a surface within a given time interval Δt [125] to

$$N_{\mathrm{strike}} = p_{\mathrm{gas}} A_{\mathrm{strike}} \Delta t \sqrt{\frac{1}{m k_{\mathrm{B}} T}} \tag{6.1}$$

with p the gas pressure, A_{strike} the considered area, m the mass of the considered gas atom or molecule, k_B Boltzmann´s constant and T the absolute temperature. Solving (6.1) for Δt, using $p = 1\ bar$, the mass of the oxygen molecule and $N_{strike} = R_{O,avg}$ yields $\Delta t \approx 4\ ps$. Assuming a silicon melting time of $\tau_{melt} = 50\ ns$ during laser doping yields $N_{strike} \approx 3 \times 10^{16}\ cm^{-2}$, which is four orders of magnitude higher than the number of incorporated oxygen atoms per pulse. Therefore, it is possible that the source of the oxygen found in the laser irradiated layers is the molecules impinging on the melt. Accordingly, it also seems possible that the incorporation of the dopant atoms takes place from the gas phase of the evaporated doping precursor (see chapter 4). Still, this finding does not rule out incorporation from an oxide layer. Indeed $N_O \approx 2.4 \times 10^{13}$ cm^{-3} already after the first two laser pulses, indicating that initially the oxygen uptake is much higher, with probably the native oxide layer as a source. Assessing, however, the oxidation kinetics during the pause between two successive laser pulses, only lasting some tens of microseconds, is rather complex and out of the scope of this work. Therefore this work will not elaborate further on the incorporation mechanism.

6.4.3 Impurity Characterization

A multitude of studies investigated the configuration and effects of the three incorporated impurity species C, O, N of Figs. 6.15 and 6.16. Carbon is known to be part of structural defects in annealed silicon, giving rise to the so called C-line [126], G-line [127] or P-line [128] in Photoluminescence (PL) measurements. Nitrogen is believed to be incorporated above all in the kinetics of so called shallow thermal donors (STDs), electrically active defect states that additionally involve oxygen [129]. Oxygen itself is the most widely studied species, being responsible for further donor states, also known as thermal and new thermal donors (TDs, NTDs), e.g. [130,131], as well as other defect states, such as oxygen precipitates [132]. Some of these structures are optically active and can be detected by Fourier Transformed Infrared Absorption (FTIR) or PL measurements.

FTIR Measurements

FTIR has been used widely as a tool to characterize the electronic structure of crystallographic irregulatities in silicon. Kaiser [133] found a strong absorption band at 1106 cm^{-1} at room temperature, which he associated with oxygen. Hrostowski [134] examined the temperature evolution of this signature and found a shift towards higher wavenumbers for decreasing T. He suggested an interstitial configuration of the oxygen (O_I). The same band was observed by Stein and Peercy [135] in oxygen implanted Si, together with signatures of oxygen-vacancy (O-V) and divacancy (V-V) defects. They performed a laser annealing step, which annealed the O-V and V-V defects but not the O_I defect.

To check if some of the signatures described in literature, above all the absorption peak at $\lambda^{-1} = 1106$ cm^{-1}, described by Stein also form during laser doping, the samples from the SIMS measurements in the preceding section (see figure 6.14) section are used for FTIR measurements at room temperature. The measurement setup is introduced in chapter 3. The laser fluence is $D_p = 1.3$ Jcm^{-2}, whereas N_{melt} varies between 1 and 192.

Figure 6.18 presents the absorption A_abs in the range of $900 < \lambda^{-1} < 1200$ cm^{-1}, measured at room temperature. Clearly an increase in A_abs around $\lambda^{-1} = 1100$ cm^{-1} for higher N_{melt} shows. The maximum peak height for 192 melt cycles reaches $A_abs = 0.6$ %. This absorption band corresponds to the literature values of the 1106 cm^{-1} band. In comparison to the literature values there exists a broadening of the peak towards lower wavenumbers. There also seem to be two, sharply differentiated peaks for all measured curves. Further, the peak positions for $N_{melt} = 192$ are shifted towards lower wavenumbers by $\Delta\lambda^{-1} = 5$ cm^{-1}.

Measuring at low temperatures greatly enhances signal strength and sharpness [134]. Thus the samples are remeasured at liquid helium temperature in a different setup. Figure 6.19 shows the expected shift towards $\lambda^{-1} = 1134$ cm^{-1} as well as the increase in peak height[3]. The maximum absorption reaches $A_abs \approx 1.2$ %, whereas the monotonous increase of the absorption for higher N_{melt} remains unchanged.

In the literature there exist calibration factors χ for the conversion of the measured absorption into absolute concentration values C_O of interstitial oxygen. They are of the form $C_O = \chi\alpha_0$ with α_0 being the absorption coefficient determined from measurements. In [132] an overview of different factors used for different measure-

---

[3] The FTIR measurements at low temperature were performed by M. Allardt, University of Dresden. The support in measuring and interpreting the data is greatly appreciated.

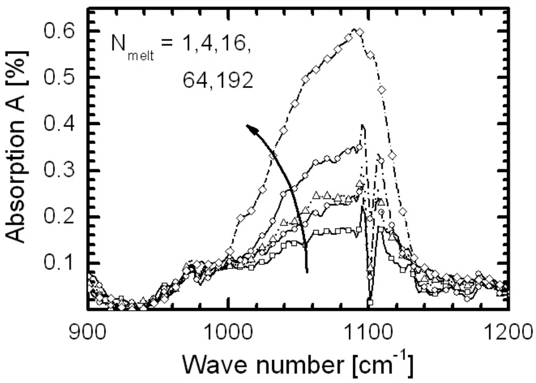

Fig. 6.18: For an increasing number of melting cycles the infrared absorption in the range of λ^{-1} = 1100 cm^{-1} grows monotonously. Measurements at room temperature.

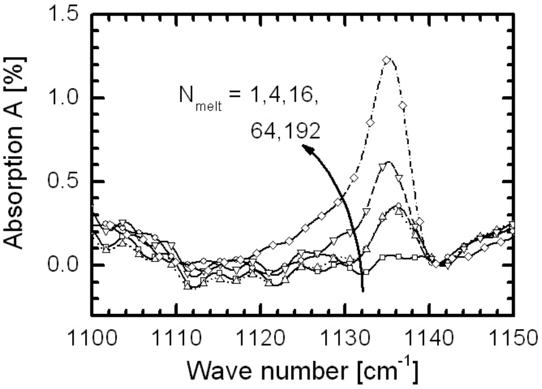

Fig. 6.19: At liquid helium temperature the broad peak around $\lambda^{-1} \approx 1100$ cm^{-1} shifts to higher wavenumbers, as reported in the literature. Apparently interstitial oxygen is responsible for the absorption. The monotonous intensity gain prevails.

ment conditions is given. From the measured absorption rates at N_{melt} = 192 we obtain an absorption coefficient $\alpha_{RT} \approx 75\ cm^{-1}$ for room temperature and $\alpha_{LHe} \approx 151\ cm^{-1}$ for liquid helium temperature, assuming an absorbing, oxygen containing layer of approximately 400 nm on each side of the samples, according to figure 6.14. For room temperature the conversion factor is $\chi = 3.14 \times 10^{17}\ cm^{-3}$, yielding an oxygen concentration of $C_O = 75\ cm^{-1} \times 3.14 \times 10^{17}\ cm^{-2} = 2.4 \times 10^{19}\ cm^{-3}$ for our samples. For liquid helium temperature also the FWHM width of the absorption peak $\Delta\omega_{abs}$ needs to be taken into account. Therefore the oxygen concentration is $C_O = \chi\Delta\omega_{abs}\alpha_0 = 1.4 \times 10^{16}\ cm^{-2} \times 5.5 \times 151\ cm^{-1} = 1.2 \times 10^{19}\ cm^{-3}$. Both values are of the same order of magnitude as measured by SIMS in figure 6.14. A different value results from the comparison of the absorption peak height of the laser irradiated sample ($N_{melt} = 192$) with the peak of a sample with known oxygen concentration. This comparison only yields $C_O \approx 3 \times 10^{18}\ cm^{-2}$ [136], which is approximately five to ten times lower than the above values. The reason for this large discrepancy is not clear. However, the determination of the absolute oxygen content by using the approximate incorporation depth and the calibration factors bears significant uncertainties, as does the comparative estimation, using a known sample.

Apart from O_I, the performed measurements do not reveal any other infrared active species inside the examined wavenumber interval of $500 < \lambda^{-1} < 2000$, in spite of a multitude of other absorption bands, characteristic for the above mentioned oxygen donor states, precipitates, etc. also being located inside this interval. Thus they either do not form during laser induced melting, or their concentration remains below the detection limits of the used instruments. As the thickness of the laser affected layers at the two surfaces remains below 1 μm even for the large number of melting cycles used here, also the corresponding absorption volume is only approximately 0.3 % of the total wafer volume. This fact possibly hinders the detection of other infrared active species which do not occur in such large concentrations as O_I.

PL Measurements

Figure 6.20 shows the results of PL-measurements of the sample with $N_{melt} = 192$ from the above series, compared to a not irradiated reference sample[4]. The measurements were also taken at liquid helium temperature, with an excitation wavelength $\lambda = 514$ nm. The absorption length L_α for this wavelength is $L_\alpha \approx 1$ μm, so that the detected signal contains significantly more information from the irradiated layer than the FTIR signal. The measured curve of the irradiated sample perfectly matches the reference curve, apart from showing a slightly lower signal. Above all, neither the well known dislocation lines in the range of 0.8 eV$< E_{PL} <$ 0.99 eV [137], nor the C, G and P-lines show up in the PL spectra. Also certain thermal donors exhibit PL signatures, as described by Tajima [138] or Nakajima [139]. However, these lines can not be found in the measurement of Figure 6.20, either. The slight decrease in the intensity probably stems from a minor surface texture that is created by the irradiation.

As the PL characterization does not show any evidence of optically active dislocations, it further backs up the earlier results of the absence of one and two dimensional crystal defects inside the irradiated layers. Also other types of known defects seem not to be present. The FTIR measurements prove that the oxygen found by SIMS is incorporated interstitially. No other lines of thermal donors, carbon or nitrogen related species could be detected. Still, some could exist because of the low aerial

---

[4] The PL measurements at low temperature were performed by J. Weber, M. Allardt, University of Dresden. Their support in measuring and interpreting the data is greatly appreciated.

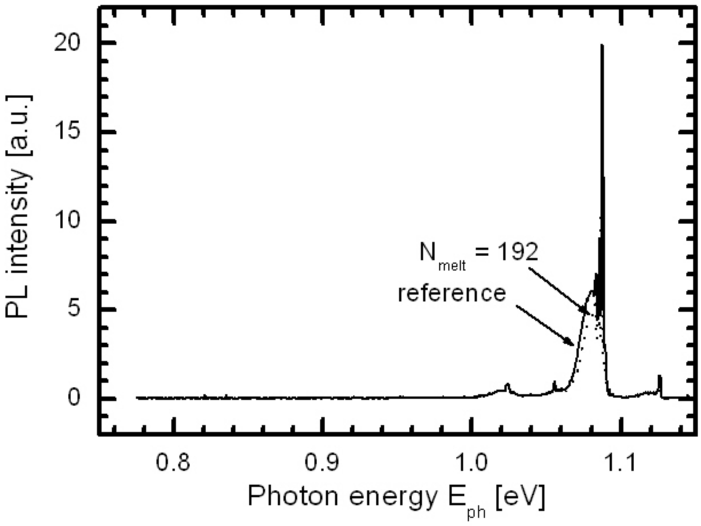

Fig. 6.20: The comparison of PL-measurements from the untreated reference and one 192-fold irradiated sample shows no observable difference in the resulting spectra. The signal from the irradiated sample is slightly lower around 1.1 eV, which is, however, caused by the laser induced surface texture.

density of the incorporated species when the whole absorption volume is regarded. To look for any electrically active species I therefore additionally perform ECV measurements on selected samples.

ECV Measurements

Figure 6.21 depicts the results from an ECV measurement of two irradiated p-type FZ samples with D_p = 1.8 Jcm^{-2} and N_{melt} = 4 and 16. Clearly, a conductivity change from p-type to n-type is observed at the surface, with a maximum concentration $C_{max} \approx 2 \times 10^{17}$ cm^{-3}, extending approximately 200 nm and 300 nm into the substrate for four and 16 melt repetitions respectively. The profile for the low number of melting cycles rapidly declines, whereas the sample for the higher N_{melt} approaches a more rectangular shape. For later calculations I use a Gaussian profile with $C_{max} = 2 \times 10^{17}$ cm^{-3}, and a $1/e$ width of σ = 55 nm as an approximation for a doping profile with low N_{melt}, and a rectangular profile with $C_{max} = 2 \times 10^{17}$ cm^{-3} and a depth z = 200 nm for a high N_{melt}. The phenomenon of conductivity change upon laser irradiating a p-type substrate was also reported by Mada [122],

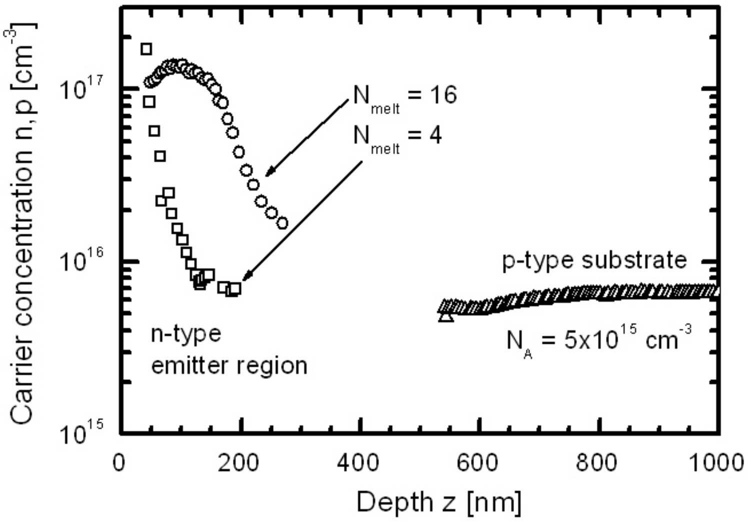

Fig. 6.21: Determining the carrier concentration by ECV-profiling shows that inside the laser irradiated surfacial layers an n-type doping occurs. The peak concentration amounts to $C_{max} \approx 10^{17}\ cm^{-3}$, while the depth of the doping profile reaches depths of $d_{dop} = 200$ nm for four and $d_{dop} = 300$ nm for 16 melt cycles respectively.

who even fabricated pn-junction diodes from the irradiated areas. They however ruled out oxygen thermal donors being responsible for the doping, as they did not see the vanishing of the n-type doping after annealing the samples at 650 °C for 1 h, which they claimed sufficient for the destruction of these donors.

Thermal Annealing Experiment

To investigate on the thermal behaviour we perform thermal annealing experiments at temperatures $T = 800$ °C for 6 h with the ECV measured samples of Figure 6.21. Interestingly the n-type doped surfacial region vanishes and p-type conductivity is re-established throughout the whole sample. Obviously there is indeed a kind of "thermal donors" created by the irradiation, only their specific type is difficult to analyse. Based on these findings we prepare three series of lifetime samples from FZ, p-type doped substrates with $N_A = 5 \times 10^{15}$ cm^{-3}. The laser parameters are $D_p = 1.8$ Jcm^{-2} and $0 < N_{melt} < 16$. One series is passivated with the same process as described above directly after the irradiation. The other two sets are RCA cleaned and then subjected to an annealing step in N$_2$ atmosphere at $T = 600$ °C and 800 °C

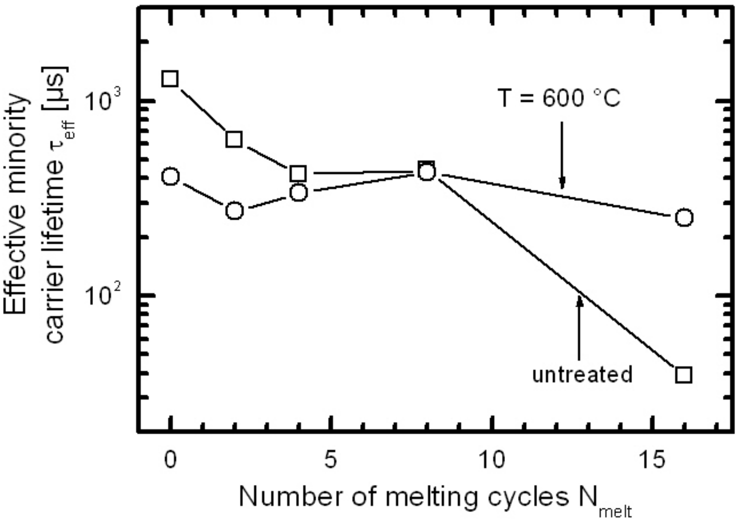

Fig. 6.22: Annealing the samples irradiated with $D_p = 1.8$ Jcm^{-2} and $0 < N_{melt} < 16$ leads to a certain degradation of minority carrier lifetimes, as the reference τ_{eff} drops from $\tau_{eff} \approx 1300$ μs to $\tau_{eff} \approx 400$ μs without irradiation. On the contrary, there can be seen a strong influence of the temperature treatment on the lifetime of the sample irradiated with $N_{melt} = 16$. Here the lifetime drastically increases from $\tau_{eff} = 40$ μs to $\tau_{eff} = 250$ μs

respectively. After annealing, an HF-dip precedes the surface passivation with SiN$_x$. Finally the effective carrier lifetime of all three series is measured. Unfortunately, some degradation during the annealing step obscures the results and renders the 800 °C samples useless. The samples annealed at $T = 600$ °C, however, still show an interesting feature. Figure 6.22 depicts these results. The reference samples exhibit the well known monotonic lifetime decrease for higher values of N_{melt}, from $\tau_{eff} = 1200$ μs($N_{melt} = 0$) to $\tau_{eff} = 40$ μs($N_{melt} = 16$). After thermal treatment, some degradation appears due to the annealing, as the lifetime of the untreated reference sample drops from $\tau_{eff} = 1300$ μs to $\tau_{eff} = 400$ μs. I ascribe this reduction to some residues not completely removed by the cleaning step, or residues inside the annealing furnace. The opposite effect, however, appears for the maximally irradiated sample ($N_{melt} = 16$). Here the lifetime increases from $\tau_{eff} = 40$ μs to $\tau_{eff} = 250$ μs. Apparently the thermal treatment removes the n-type doping and likewise destroys or diminishes the laser induced defects in the sample.

6.5 Discussion

6.5.1 Defect Nature

The preceding results give a strong hint, that the appearance of an n-type doping after laser irradiation and the lifetime degradation are linked. Similar phenomena were e.g. reported by Karg et al. [140]. They found electrically active, oxygen related defects, which acted as donors, and simultaneously reduced the minority carrier lifetime, due to a high capture cross section for holes. However, Karg et.al. could unambiguously identify the type of defect in their publication by FTIR and Deep Level Transient Spectroscopy (DLTS) characterization, while similar measurements do not give a clear picture of the defect nature in the current work. Therefore, a clear association of the effects, which are seen in laser irradiated silicon, with some of the known oxygen donors, is not possible. However, the results lead to a number of conclusions:

Dependency of τ_{eff} on N_{melt} and D_p. Laser irradiation degrades the effective minority carrier lifetime in both, n- and p-type silicon material. There is a direct correlation between τ_{eff} and the laser pulse energy density as well as the number of melting cycles.

Minor Influence of the Surface. The increase in surface area for typical laser irradiation parameters is below 1 % and thus negligible. An increase of the interface trap density is possible. Etch experiments, however, show, that the contribution of the actual surface to the total laser induced recombination is not predominant. In contrast to that, the recombination is distributed throughout the laser affected surfacial layer. There is no introduction of defects into the silicon bulk.

Impurity Incorporation. A strong incorporation of the impurities oxygen, carbon and nitrogen occurs. They are continuously supplied from the ambient gas during multiple irradiations. The total oxygen concentration increases linearly with N_{melt} and reaches a maximum concentration $C_O \approx 10^{19}\ cm^{-3}$.

Interstitial oxygen without precipitation. The incorporated oxygen is configured interstitially inside the silicon lattice, as shown by FTIR measurements. The concentration determined from these measurements roughly corresponds to the results of the SIMS analysis. There is no evidence of oxygen precipitates. Their existence would be surprising anyway, as they are usually formed due to the aggregation of supersaturated oxygen by prolonged heat treatment. As the melting and recrystallization during laser doping are in the range of $10^9 - 10^{10}\ Ks^{-1}$, there is no time for such aggregation. Results from Pensl [141], who avoided oxygen precipitation by a rapid thermal quench of Ribbon Growth on Substrate (RGS) silicon also backs this consideration.

Absence of crystal defects. Structural characterization by X-Ray Topography as well as defect etching also show no sign of oxygen precipitates (OPs), and no dislocation loops or stacking faults produced during the formation of OPs, nor any other crystal irregularities. Photoluminescence does not show any evidence of known oxygen related defects, nor any other photoactive defects, either. Thus the findings of the TEM measurements of Köhler et.al. [3] are coroborated. There are no detectable crystal irregularities inside the laser treated layers. They seem to be free from one and two dimensional structural defects.

Laser induced n-type doping. In spite of the optical measurements not showing evidence of electrically active species, ECV profiling still reveals that the laser irradiation causes an n-type doping inside the surface layers. The doping profiles match the diffusion profiles of the detected C, O and N, while their absolute concentration is around $10^{17}\ cm^{-3}$. Prolonged heat treatment destroys these donors and likewise leads to a partial recovery of the effective minority carrier lifetime of heavily irradiated samples. This correlation indicates that the lifetime degradation after laser irradiation is caused by the incorporated impurity species, which form recombination centres and at the same time exhibit a donor like behaviour. It is important to note that the lifetime reduction is not caused by the doping, but by the defects, which come along with the doping. The following estimation will confirm this statement.

6.5.2 Estimation of Defect Lifetime

The laser treatment gives rise to an n-type doping with concentrations $N_D \approx 10^{17}$ cm^{-3}, as evident from Fig. 6.21. Further, the laser induced defects are distributed throughout the several 100 nm of irradiated surface layer. Thus, the local minority carrier lifetime inside the surface layer must be sufficiently low, to cause a noticeable effect on the effective lifetime. The Auger lifetime for $N_D = 10^{17}$ cm^{-3} ranges around $\tau_{Aug} \approx 50$ μs, resulting in a diffusion length $L_{Aug} = \sqrt{D\, \tau_{Aug}} \approx 300$ μm[5]. This value is in the range of the bulk diffusion length of high quality bulk silicon, and would therefore not cause any noticeable recombination inside a several hundred nanometer thin surface layer. Thus, the n-type doping **alone** does not degrade τ_{eff}. In fact, the diffusion length needs to reduce to a few μm to cause an effect on the lifetime. This would be the case for defect lifetimes around or below $\tau_{SRH} = 10$ ns, corresponding to a diffusion length $L_{SRH} \approx 4$ μm.

6.5.3 Implications for Laser Diffused Emitters

The strong dependence of τ_{eff} on D_p and N_{melt}, which is discussed in this chapter, generally suggests using the minimum possible number of melting cycles, as well as the minimum possible laser pulse energy density for the fabrication of laser diffused emitters. From an industrial point of view, this fact coincides with maximizing the throughput of a laser doping process. The investigations in the following chapter will assess the impact of different laser irradiation parameters on furnace diffused and laser diffused emitters, and thereby demonstrate the potentials of the laser doping process.

---

[5] Using a diffusion coefficient $D \approx 19$ cm^{2}s^{-1}, as corresponding to an n-type doping density $N_D \approx 10^{17}$ cm^{-3}

Chapter 7

Characterization of Laser Doped Emitters

7.1 Introduction

The last chapter showed that laser irradiation leads to a degradation of the effective minority carrier lifetime in silicon, due to the introduction of laser induced defects into the melted and recrystallized surface layer. The magnitude of this degradation is strongly dependent on the applied laser parameters. The local lifetime inside the affected surface layer is roughly estimated to range around $\tau_{loc} \approx 10$ ns, which is comparable to the local Auger lifetime inside a medium doped emitter. Therefore, the effect of the laser irradiation should be noticeable in low to medium doped emitters, but negligible in highly doped emitters. The first section of this chapter strengthens this assumption, as it presents data regarding the impact of laser irradiation on lowly doped high efficiency emitters. The second section addresses the situation in emitters fabricated from liquid and sputtered phosphorous doping precursors. The third section presents data from p-type emitters, fabricated from laser irradiated aluminium layers.

7.2 Phosphorous Emitters

7.2.1 Laser irradiated furnace diffused emitters

Experimental

Furnace diffused high efficiency emitters serve to evaluate the impact of the laser induced defects on real emitters. As substrates p-type FZ silicon with $N_A = 7 \times 10^{13}$ cm^{-3}, a thickness of $w = 500$ μm and polished front and etched back sides are used. The processing sequence comprises

- RCA clean
- Phosphorous diffusion
- Drive-in and oxidation
- Oxide stripping
- Laser irradiation of front and back surface
- RCA clean
- Silicon nitride re-passivation ($n \approx 3$) of both surfaces.

The emitter sheet resistance after diffusion and drive-in amounts to $\rho_s \approx 100\ \Omega/\Box$. Similar to the lifetime samples of chapter 6, quarter wafers are irradiated with the laser, with always one untreated quarter as reference. After the re-passivation the wafers are cleaved into the quarters and their effective lifetime is measured. Similarly to chapter 6, there exist two sets of laser parameters with $N_{melt} = 2$ and 20. The laser pulse energy density varies between 1.0 Jcm^{-2} $< D_p <$ 2.0 Jcm^{-2}. Apart from the samples irradiated with $D_p = 2.0$ Jcm^{-2} the samples sheet resistance does not change after the laser irradiation. For the high pulse energy density the sheet resistance increases, which is in accordance with surface evaporation caused by the high D_p.

Lifetime data

Figures 7.1 and 7.2 exhibit the results from the QSSPC lifetime measurements of the two different series. In both series, the untreated reference samples show very high maximum effective lifetimes $\tau_{eff} \approx 3$ ms. For $N_{melt} = 2$ the laser irradiation

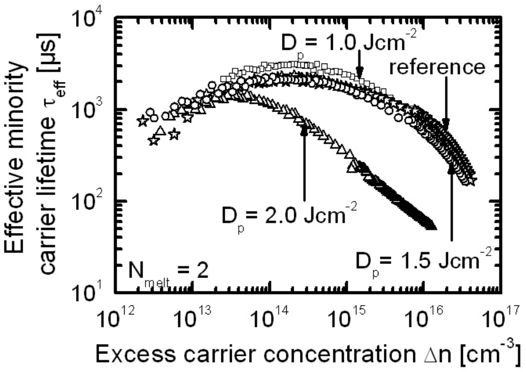

Fig. 7.1: The effective lifetime of furnace diffused emitters irradiated with $N_{melt} = 2$ and $1.0\ \text{Jcm}^{-2} < D_p < 2.0\ \text{Jcm}^{-2}$ shows a relatively low sensitivity to laser treatment for $D_p = 1$ or $1.5\ \text{Jcm}^{-2}$, when compared to the untreated reference. Only high pulse energies $D_p = 2.0\ \text{Jcm}^{-2}$ lead to a strong degradation of carrier lifetime. This effect is caused by the onset of surface evaporation.

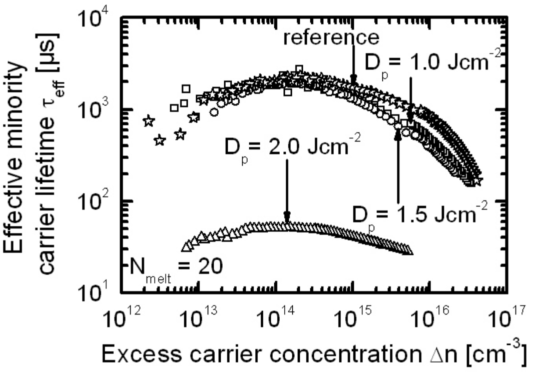

Fig. 7.2: The effective lifetime of furnace diffused emitters irradiated with $N_{melt} = 20$ and $1.0\ \text{Jcm}^{-2} < D_p < 2.0\ \text{Jcm}^{-2}$ shows higher sensitivity to laser treatment with $D_p = 1$ or $1.5\ \text{Jcm}^{-2}$ and a massive degradation for $D_p = 2.0\ \text{Jcm}^{-2}$ when compared to the series with $N_{melt} = 2$. The reason for the higher sensitivity stems from the higher amount of incorporated impurities.

shows almost no impact on the effective carrier lifetime for $D_p = 1.0$ and $1.5\ \text{Jcm}^{-2}$, as the corresponding curves range only slightly below the reference curve. For high $D_p = 2.0\ \text{Jcm}^{-2}$, however, the impact becomes very clear, as the corresponding curve does not reach the maximum lifetimes of the other curves and exhibits a strongly linear slope towards higher excess carrier densities, as typical for strong emitter recombination. The reason for this strong degradation is once again the onset of surface damage at this high pulse energy density. For $N_{melt} = 20$ (figure 7.2) the picture is slightly but not significantly different. Here, the lifetime values for irradiation with $D_p = 1.0$ and $1.5\ \text{Jcm}^{-2}$ are only slightly below the untreated reference, albeit already clearly distinguishable from that. Similarly as for the low number of melting cycles, going to $D_p = 2.0\ \text{Jcm}^{-2}$ induces a huge lifetime drop, which is even more pronounced as in figure 7.1.

Emitter saturation current density

Equation 2.36 allows for the extraction of the emitter saturation current densities of the samples from the measured effective lifetimes. The untreated references hereby exhibit very low values of $J_{oe} \approx 25$ fAcm^{-2} which is a sign for both very good emitter quality as well as good surface passivation by the applied silicon nitride layer. Figure 7.3 presents the extracted emitter saturation current densities plotted against the applied laser pulse energy density for the two sample series. As visible already from the lifetime measurements the impact of the laser irradiation at $D_p = 1.0$ Jcm^{-2} is low for both $N_{melt} = 2$ and 20, increasing the saturation current density from $J_{oe} = 25$ fAcm^{-2} to $J_{oe} = 37$ and 49 fAcm^{-2} respectively. For $D_p = 1.5$ Jcm^{-2} the difference between the two series becomes more pronounced, with $J_{oe} = 48$ fAcm^{-2} for $N_{melt} = 2$ and $J_{oe} = 157$ fAcm^{-2} for $N_{melt} = 20$. Due to the partial evaporation of the surface the J_{oe}-values increase drastically to $J_{oe} = 581$ fAcm^{-2} ($N_{melt} = 2$) and $J_{oe} = 1.56$ pAcm^{-2} ($N_{melt} = 20$).

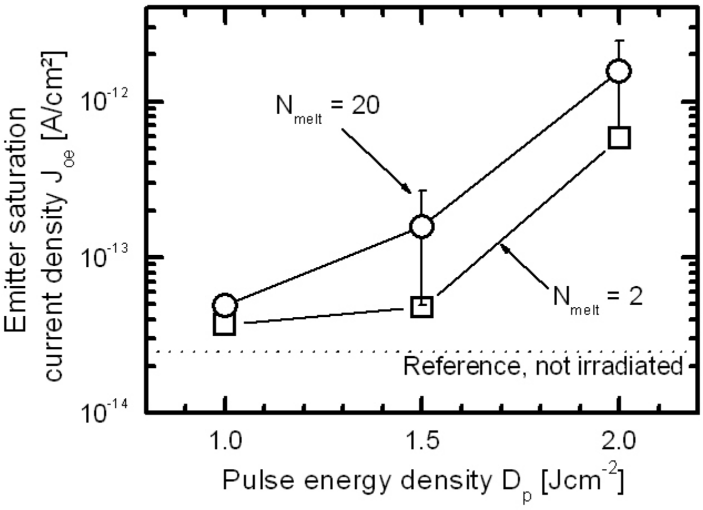

Fig. 7.3: Laser irradiation of furnace diffused emitters leads to an increase in the extracted emitter saturation current densities. For $N_{melt} = 2$ the values increase from the reference $J_{oe} = 25$ fAcm^{-2} to $J_{oe} = 37, 48$ and 581 fAcm^{-2} for 1.0 Jcm^{-2} < D_p < 2.0 Jcm^{-2}. For $N_{melt} = 20$ the increase is more pronounced, leading to values of $J_{oe} = 48, 157$ and 1560 fAcm^{-2}. The jump in J_{oe} for the highest pulse energy density results from the onset of surface evaporation and the thereby caused damage.

Analysis of doping profiles

As shown in chapter 6, laser irradiation leads to an incorporation of oxygen, carbon and nitrogen from the ambient into the silicon. Figure 7.4 shows the phosphorous doping profiles of one reference and three samples irradiated with $D_p = 1.0$ and 1.5 Jcm^{-2} and $N_{melt} = 2$ and 20. Figures 7.5 - 7.7 then show a more detailed view of the three differently irradiated samples, including the profiles for oxygen and carbon. The phosphorous concentration in all four doping profiles has been scaled from the measured raw data in order to match the measured emitter sheet resistance.

Already in the overview of figure 7.4 the clear impact of the laser irradiation on the pre-existing phosphorous doping is seen. In contrast to the reference sample, which exhibits a Gaussian doping profile caused by the drive-in, with a surface concentration $C_s \approx 1.5 \times 10^{19}$ cm^{-3}, all other samples show alterations in the doping profile up to a clearly defined depth. The course of the profile of the sample with $N_{melt} = 2$ and $D_p = 1.0$ Jcm^{-2} is virtually horizontal at the surface, instead of the sloped Gaussian profile. The effect is pronounced for the sample with $N_{melt} = 20$, which exhibits a decreasing phosphorous concentration towards the surface. The reason for this decrease towards the surface is not perfectly clear. As the emitter sheet resistance of this sample remains unchanged from the untreated reference, it is improbable that the irradiation causes phosphorous outdiffusion. Accordingly no loss of phosphorous but only a shift of the maximum from $z = 0$ to $z \approx 150$ nm is observed. A segregation coefficient of phosphorous larger than unity could cause such an effect, similar to the considerations for oxygen in chapter 6. However, such a value for phosphorous has never been reported in literature. Possibly also changes in the surface matrix could cause a variation in the SIMS count rate, leading to a misinterpretation of the absolute phosphorous concentration. The sample with $N_{melt} = 20$ and $D_p = 1.5$ Jcm^{-2} shows the same decrease of phosphorous concentration towards the surface, only the affected depth is higher, extending to $z \approx 320$ nm, corresponding to the higher pulse energy density, leading to a higher melting depth.

A closeup on the single profiles, including the count rates for oxygen and carbon exhibits the expected situation. The sample with $N_{melt} = 2$ and $D_p = 1.0$ Jcm^{-2} in figure 7.5 shows a significant carbon incorporation up to a depth $z \approx 180$ nm, corresponding to the depth up to which the phosphorous doping profile is altered from the reference Gaussian shape. The carbon concentration declines rapidly from the surface. The oxygen profile is even weaker and only in the first 100 nm dis-

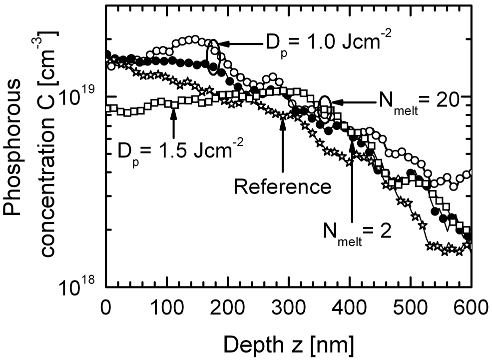

Fig. 7.4: Laser irradiation alters the pre-existing Gaussian phosphorous doping profiles from furnace diffusion. Already a low pulse energy density $D_p = 1.0\ \mathrm{Jcm}^{-2}$ causes a virtually horizontal course of the profiles ($N_{melt} = 2$), or even a decrease of the doping concentration towards the surface ($N_{melt} = 20$), with an affected depth of $z \approx 150$ nm. Increasing the pulse energy density to $D_p = 1.5\ \mathrm{Jcm}^{-2}@N_{melt} = 20$ likewise causes a decrease of the phosphorous concentration at the surface, albeit the affected depth extends to $z \approx 320$ nm. This sample also exhibits a lower surface concentration $C_s = 8.6 \times 10^{19}\ \mathrm{cm}^{-3}$.

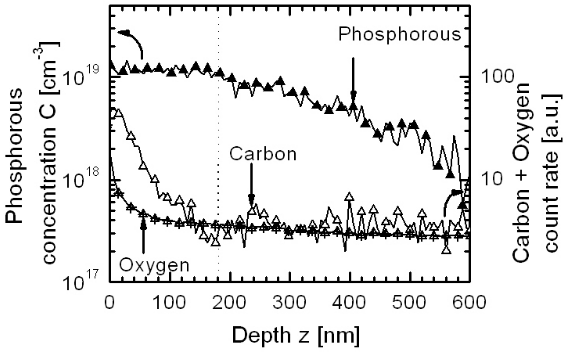

Fig. 7.5: Taking a detailed look at the phosphorous, oxygen and carbon profiles of a sample treated with $D_p = 1.0\ \mathrm{Jcm}^{-2}$ and $N_{melt} = 2$ shows that the incorporation depth $z \approx 150$ nm of carbon matches the region in which the phosphorous doping profile is altered. The carbon count rate, however, rapidly declines from the surface into the sample. The oxygen count rate is only slightly increased at the surface.

tinguishable from the background. Going from 2 to 20 melt cycles mainly affects the C and O incorporation, as visible in figure 7.6. Their incorporation depth stays virtually constant, when compared to figure 7.5, however their profiles turn into more rectangular shapes. In figure 7.7 this trend is pronounced for oxygen, as the melt depth for the higher pulse energy density extend to $z \approx 350$ nm. The carbon profile changes back to a rather exponential shape, rather than the rectangular one of figure 7.6. However, both impurities reach deeper into the emitter for the higher value of D_p.

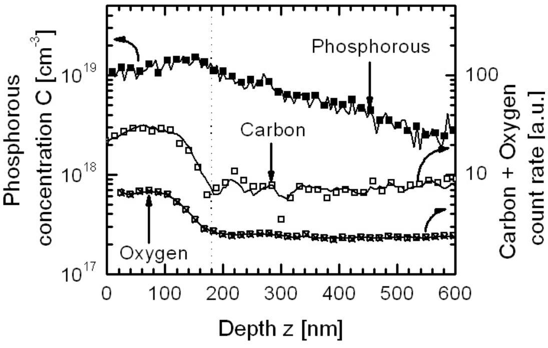

Fig. 7.6: In comparison to figure 7.5 an increase of the melting cycles from $N_{melt} = 2$ to 20 significantly increases both the effect on the phosphorous doping as well as the incorporation of oxygen and carbon. Similar to the findings in chapter 6 the profiles of both impurities exhibit rather rectangular shapes. Their incorporation depth $z \approx 180$ nm again matches the depth up to which the phosphorous doping is altered.

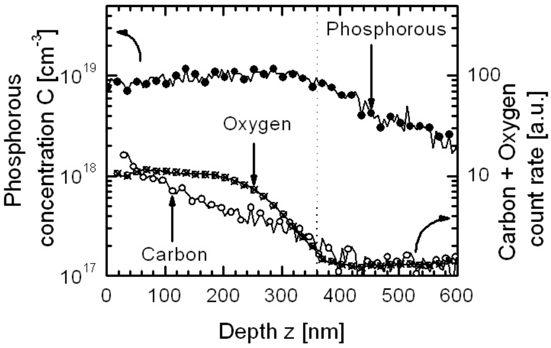

Fig. 7.7: An increase in the pulse energy density while keeping N_{melt} constant leads to an increased incorporation of impurities up to a depth $z \approx 320$ nm, as would be expected from the deeper melting zone in the silicon.

Estimation of defect lifetime

As apparent from the above results, the impurity incorporation is comparable for undoped lifetime samples and samples with a pre-existing phosphorous doping profile. Therefore one would expect that the incorporated impurities likewise lead to the introduction of defects, as observed for the lifetime samples. To validate this theory, a theoretical emitter saturation current density $J_{oe,calc}$ is determined from the measured phosphorous doping profiles of the irradiated, pre-diffused emitters, according to Eq. 2.37. To account for the effect of laser induced defects, an additional Shockley Read Hall lifetime τ_{SRH} is included, following Eq. 2.39. A variation of τ_{SRH} within reasonable limits (e.g. 1 ns $< \tau_{SRH} <$ 1 μs) leads to changing values for $J_{oe,calc}$. The comparison of measured saturation current densities J_{oe} of laser irradiated emitters, and calculated values $J_{oe,calc}$ then yields the expected range of τ_{SRH}.

For a reliable estimation, the exact value of the emitter surface recombination velocity S_f of the irradiated samples needs to be known. This value is in turn dependent on the surface doping concentration of these samples. The surface recombination velocity $S_{f,ref}$ of the not irradiated reference samples serves as a reference point for the determination of S_f. Modeling the emitter saturation current density $J_{0e,mod}$ of the reference samples, either with the device simulator PC1D, or by using Eq. 2.37, allows for the extraction of $S_{f,ref}$: The measured doping profile of the reference samples serves as input parameter for the modeling. By varying the surface recombination velocity $S_{f,mod}$ in the model, the value of $J_{0e,mod}$ is matched with the measured $J_{0e,ref}$ of the reference samples. For that case $S_{f,mod} = S_{f,ref}$ holds.

As shown by Kerr [41] for silicon nitride and Cuevas [142] for silicon dioxide passivated surfaces, the SRV depends on the surface doping concentration (see also chapter 2). Unfortunately, the silicon nitride layers of this thesis are silicon rich, unlike the layers employed by Kerr. Therefore, deviations from their dependence on the surface concentration are possible. The calculation of the emitter saturation current density for the not irradiated reference sample requires an SRV value of $S_{f,ref} = 1000$ cms^{-1} to obtain the measured value of $J_{oe} = 25$ fAcm^{-2}. This SRV value is lower than the value of $S_{kerr} = 1758$ cms^{-1}, resulting from the parametrization of Kerr and the value of $S_{Cuevas} = 1720$ cms^{-1}, resulting from the parametrization of Cuevas for a surface concentration $C_S = 1.72 \times 10^{19}$ cm^{-3}, as found in the reference sample. Thus, for the SRV determination of laser irradiated samples with varying surface concentrations, I use a corresponding scaling factor R_{SRV} to obtain values for their surface recombination velocity according to

$$S_{eff}(C_s) = R_{SRV} 10^{16}\ cm^{-3} C_s \tag{7.1}$$

following the parametrization of Cuevas in the regime 10^{19} cm^{-3} $< C_s < 2 \times 10^{20}$ cm^{-3}. Table 7.1 shows the assumed values for S_{eff} together with the surface concentration, the shape of the incorporated defect profile and its incorporation depth used for the four analyzed samples.

Figure 7.8 shows the results of the calculated emitter saturation current densities versus the SRH lifetime of the incorporated defects, using the SRV values, as well as the defect profile shape and incorporation depth from table 7.1. High SRH lifetimes $\tau_{SRH} > 10^{-7}$ s would not influence the emitter saturation current, as the Auger lifetimes inside the emitters are much lower. The lower the defect lifetimes become, the higher is their impact on the resulting J_{oe}-values and the stronger the three samples differentiate. Using the measured saturation current densities of

Tab. 7.1: The effective surface recombination velocity used for the estimation of the SRH lifetime of the laser induced defects is dependent on the varying surface doping concentration of the samples. For its determination a scaling factor $R_{SRV} = 1.7$ is used together with the parametrization of Cuevas. The scaling factor is determined from the emitter saturation current density of the untreated reference sample ($N_{melt} = D_p = 0$). The shape of the incorporated defect profile is assumed as Gaussian for $N_{melt} = 2$ and rectangular for $N_{melt} = 20$. The incorporation depth results from the SIMS measurements.

N_{melt}	D_p [Jcm^{-2}]	Surface concentration [cm^{-3}]	SRV [cms^{-1}]	Defect profile	Incorporation depth [nm]
0	0	1.7×10^{19}	1000	–	0
2	1.0	1.3×10^{19}	764	Gaussian	180
20	1.0	1.1×10^{19}	629	Rectangular	180
20	1.5	7.7×10^{18}	453	Rectangular	360

$J_{oe} = 37,\ 49$ and $157\ \text{fAcm}^{-2}$ and introducing them into the figure as vertical lines yields the range for the SRH lifetime as $3\ \text{ns} < \tau_{SRH} < 7\ \text{ns}$. This range confirms the roughly estimated $\tau_{SRH} \approx 10$ ns in chapter 6. Apparently the laser generated defects indeed place a lower limit on the performance of emitters, independent of the employed doping precursor.

7.2.2 Laser diffused emitters

Experimental

Three different doping precursors serve to examine the quality of full area laser diffused emitters. Out of them there are two phosphorous containing liquids, Merck Siodop P250 and Filmtronics P508. The third precursor is red phosphorous, sputtered using a specifically fabricated target in an RF sputtering equipment. For the liquid precursors p-type, FZ wafers with $N_A = 5\times10^{12}\ \text{cm}^{-3}$, a thickness $w = 550\ \mu\text{m}$ and polished front and etched back surface are used. Like the furnace diffused samples every quarter wafer receives different irradiation parameters. The processing sequence contains:

- Spin coating and curing of front and back surface

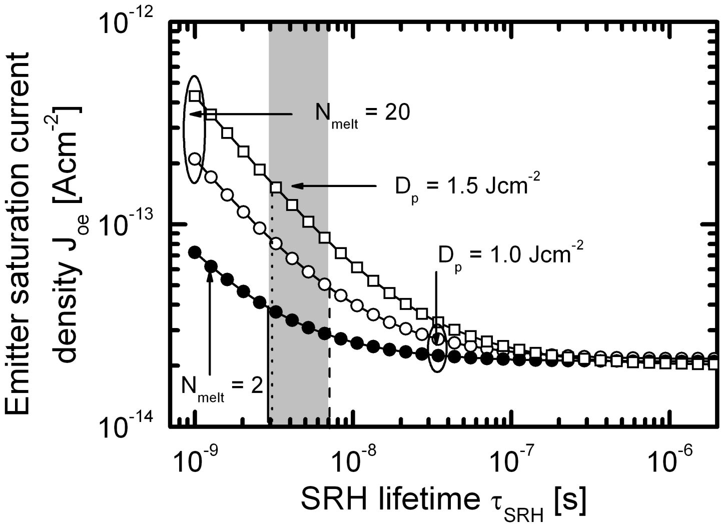

Fig. 7.8: The theoretically calculated emitter saturation current densities of the three analyzed samples divert for assumed defect lifetimes $\tau_{SRH} < 10^{-7}$ s. The comparison of calculated and measured values (vertical lines) yields a range of 3 ns $< \tau_{SRH} <$ 7 ns.

- laser irradiation of front and back surface
- HF-dip for precursor removal and cleaning
- silicon nitride ($n = 3$) deposition on front and back surface
- cleaving into quarters and lifetime measurement.

Wafers with a base doping of $N_A = 3 \times 10^{16}$ cm^{-3}, a thickness $w = 300$ μm and polished front and back surfaces serve for the evaluation of the sputtered precursor layers. Here, every wafer contains five individual laser parameter sets and one untreated, passivated field in addition for process control. The process is as follows:

- HF-dip for native oxide removal
- deposition of silicon nitride ($n = 3$) passivation and protection layer on back surface
- HF-dip, clean and rinse

- deposition of phosphorous precursor layer on front surface
- laser irradiation of front
- RCA-clean
- deposition of silicon nitride ($n = 3$) passivation layer on front surface ⇒ cleaving into six pieces and lifetime measurement.

Lifetime data

Figure 7.9 exhibits the measured effective minority carrier lifetimes of the two series with liquid precursors, irradiated with $0.7\ \mathrm{Jcm}^{-2} < D_p < 2\ \mathrm{Jcm}^{-2}$ for P250 and $D_p = 1.4$ and $1.7\ \mathrm{Jcm}^{-2}$ for P508. Only values for $N_{melt} = 2$ are depicted in the graph. The first look reveals that for $D_p < 1.5\ \mathrm{Jcm}^{-2}$ the lifetime of the P250 precursors is significantly higher than the values of the P508 precursors, which display a strong lifetime decrease towards higher injection levels, as typical for strong emitter recombination. The lifetime of the P508 samples decreases for higher laser pulse energy densities, however not very strongly. Only for $D_p = 2.0\ \mathrm{Jcm}^{-2}$ the P250 samples exhibit lower lifetimes. The reason for this phenomenon is however again the exceeding of the surface evaporation temperature, combined with a partial surface ablation in these samples. Due to the very low doping level of these substrates the overall lifetimes of these samples are high, even exceeding $\tau_{eff} = 10$ ms for the samples with the weakest irradiation. The extremely high lifetime also shows the excellent passivation quality of the silicon nitride layers.

Figure 7.10 displays the measured carrier lifetimes of the samples with sputtered precursors, $N_{melt} = 2$ and $0.8\ \mathrm{Jcm}^{-2} < D_p < 1.6\ \mathrm{Jcm}^{-2}$. Due to the higher substrate doping the overall lifetime for theses samples is much lower than the values of figure 7.9. Compared to the untreated reference the effective lifetimes of the emitter samples are significantly reduced by approximately one order of magnitude, ranging between $\tau_{eff} \approx 60\ \mu$s and $\tau_{eff} \approx 20\ \mu$s, depending on the employed pulse energy density. This strong lifetime drop already indicates a pronounced emitter saturation current density of theses samples.

Emitter saturation current density

From the measured effective lifetime the emitter saturation current density is extracted. For the n^+pn^+ samples with liquid precursors the methodology is the same

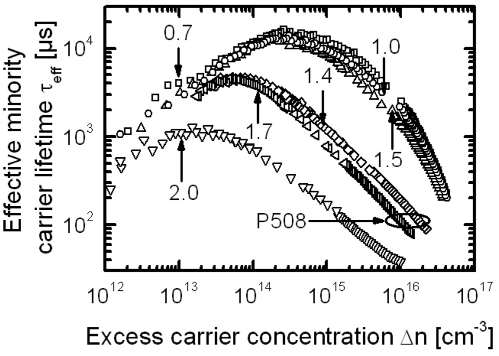

Fig. 7.9: For $0.7 < D_p < 1.5$ Jcm^{-2} the effective lifetime for the P250 doping precursor is significantly higher than for the P508 precursor and $D_p = 1.4$ and 1.7 Jcm^{-2}. Only for $D_p = 2$ Jcm^{-2} a strong lifetime drop for P250 is seen. This drop is due to surface evaporation.

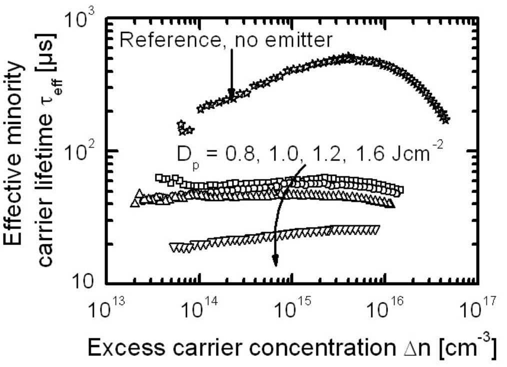

Fig. 7.10: Sputtered doping precursors lead to a significant lifetime degradation, which points to strong emitter recombination. Due to the higher substrate doping, the absolute lifetime values are lower than for the liquid doping precursors of Fig. 7.9.

as for the furnace emitters. The samples with sputtered precursors however feature a diffused front and a passivated back surface. The emitter saturation current density is therefore determined by extracting the surface lifetime τ_s from the all sides passivated reference sample and using this τ_s with Eq. 2.27 and 2.29 to extract the saturation current density of the front side emitters. Figure 7.11 presents the resulting saturation current densities for all three sample series ($N_{melt} = 2$), plotted against the sheet resistance of the emitters. On first sight the three series behave significantly different. The samples P250 and P508 both show J_{oe}-values increasing towards lower ρ_s, both with approximately the same slope, which is included into the graph as dashed/dotted lines as guide to the eye. In spite of the similar slope, the absolute J_{oe}-values of the two series are widely different. Whereas the P250 samples cover a sheet resistance range of $604\ \Omega/\square < \rho_s < 178\Omega/\square$, reaching a maximum $J_{oe} = 46$ fAcm^{-2}, the sheet resistance of the P508 samples ranges between $163\ \Omega/\square < \rho_s < 61\Omega/\square$, with saturation current densities increased by a factor of 5 minimum, with 342 fAcm$^{-2} < J_{oe} < 975$ fAcm^{-2}. Even if the resistance ranges of both series are distinct, an extrapolation of their individual slopes would lead to strongly differing values for the saturation current densities.

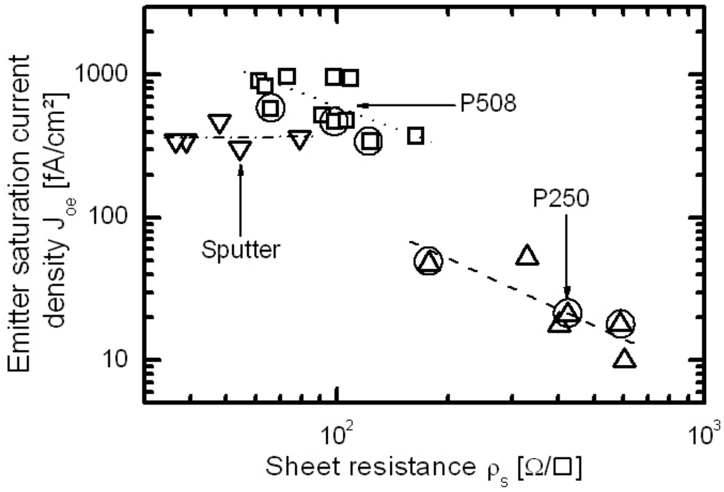

Fig. 7.11: The effective lifetimes of samples with sputtered phosphorous precursor, irradiated with the old and the new laser setup show different behaviour. For the old processing setup the τ_{eff}-values seem to be virtually independent of the amount of incorporated phosphorous, which is reflected in the sheet resistance varying from 37 $\Omega < \rho_s <$ 79 Ω. For the new setup, the effective lifetime decreases for higher doping levels, as would be expected due to augmented auger recombination. The circles mark the samples, which are characterized by SIMS (see Figs. 5.3, 5.4).

From these findings it seems logical that the P508 precursors contain impurities that degrade the quality of the suchlike fabricated emitters. However, to rule out possible influence from the resulting doping profiles themselves, three samples (marked by circles) from the the P250 and P508 series are examined by SIMS. The results are presented in Figs. 5.3, 5.4. The samples with sputtered precursors exhibit a totally different behaviour. Instead of increasing towards lower sheet resistances, their emitter saturation current densities stay rather constant between 310 fAcm^{-2} $< J_{oe} <$ 472 fAcm^{-2} for 79 $\Omega/\Box < \rho_s < 36\Omega/\Box$. One explanation for such a sheet resistance independent saturation current density is the emitter performance being dominated by a high surface recombination velocity. In such a case the influence of increasing Auger recombination in the emitter bulk is shielded by an extremely high surface recombination. Eisele [113] used these samples for SIMS analysis. He indeed found very high surface concentrations $C_s > 10^{20}$ cm^{-3}, which

Tab. 7.2: The parameters used for the calculation of an emitter saturation current density without any laser induced recombination are given below.

Sample Parameter	$L1_1$	$L1_2$	$L1_3$	$L2_1$	$L2_2$	$L2_3$
$C_s[10^{19}\ \mathrm{cm}^{-3}]$	2.47	2.86	6.8	13.6	13.6	9.34
$\rho_s[\Omega/\square]$	569	423	179	66	98	123
$J_{oe,calc}$ [fAcm^{-2}]	14	17	46	134	94	66
S_f [cms^{-1}]	1436	1663	3936	7907	7907	5430

probably lead to very high values for S_f, thus strengthening the above hypothesis.

Analysis

A detailed analysis of the emitters fabricated from the liquid precursors faces the same difficulty in the determination of the "real" value of the surface recombination velocity. With the doping precursor another possible source of contamination and consequently of additional recombination is added, including even more unknowns into any calculation. Therefore I use the measured doping profiles to determine a value of the emitter saturation current, which would be expected without including any laser or precursor generated recombination. The resulting values can then be compared with the actually measured ones, thus allowing for an assessment of the level of recombination added by the precursors. Table 7.2 presents the parameters used for the calculation. The value of the surface recombination velocity results from the measured surface doping concentration, using Eq. (7.1).

Figure 7.12 depicts the resulting measured and calculated emitter saturation current densities plotted against the corresponding sheet resistance. The measured values (hollow symbols) correspond to the values from figure 7.11. The calculated $J_{oe,calc}$ for the P250 samples align almost perfectly with the measured $J_{oe,meas}$, as becomes apparent from the figure with $J_{oe,calc} = 14, 17$ and 46 fAcm^{-2} compared to $J_{oe,meas} = 18, 21$ and 46 fAcm^{-2}. This close match shows that only negligibly few recombination active contaminants can be contained in the precursor, as a much higher emitter saturation current densities would be expected otherwise.

The situation is different for the P508 precursors, as becomes apparent from comparing the calculated $J_{oe,calc} = 66, 94$ and 134 fAcm^{-2} with the measured $J_{oe,meas} = 342, 472$ and 582 fAcm^{-2}. Here a large amount of recombination active impurities is

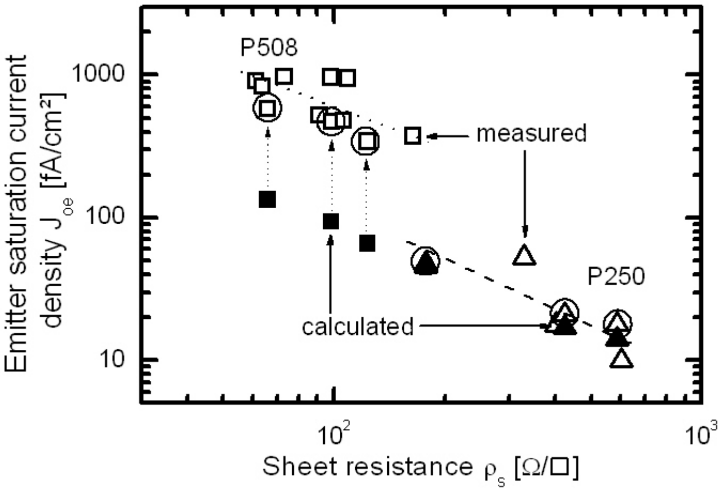

Fig. 7.12: Calculating the emitter saturation current densities expected without any laser induced recombination for the emitters fabricated with liquid doping precursors shows a strong difference between the two different precursors. The samples with P250 precursors show only very little difference between the calculated (filled triangles) and measured (hollow triangles) values, with $J_{oe,calc} = 14, 17$ and 46 fAcm^{-2} compared to $J_{oe,meas} = 18, 21$ and 46 fAcm^{-2} respectively. In contrast to that the comparison for the P508 precursors yields $J_{oe,calc} = 66$, 94 and 134 fAcm^{-2} (filled squares) compared to $J_{oe,meas} = 342, 472$ and 582 fAcm^{-2} (hollow squares). Apparently the P250 precursor is virtually free of harmful contaminants, whereas the P508 precursor contains impurities that drastically augment the recombination inside the fabricated emitters. The circles mark the samples that have been characterized by SIMS.

necessary to cause saturation current densities augmented by approximately a factor of 5 over the expected values. Looking at the results from the furnace diffused emitters also shows that this strong recombination cannot be explained by the laser induced defects alone. Indeed a rough estimation of the local lifetime necessary to cause such high saturation current densities yields values of $\tau_{SRH} \approx 10$ ps, which is three orders of magnitude lower than the lifetime of the laser induced defects.

7.2.3 Solar cells

The preceding results show that high quality solar cell emitters can be fabricated when a high purity doping precursor is used. In chapter 5 already an IV characterization of four differently produced solar cells was performed. For a more detailed insight into the influence of the emitters on the cell performance, the quantum efficiency of these four cells is analyzed in the following.

Measurements

Figure 7.13 depicts the measured Internal Quantum Efficiency of the P250, P508 and Sputter 1,2 solar cells from chapter 5. In the low wavelength regime ($\lambda < 600$ nm) clearly the strongly differing emitter quality catches the eye. The P250 cell exhibits an IQE close to unity over almost the whole wavelength segment, with a saturation value $IQE_{350} = 0.96$ at $\lambda = 350$ nm. Obviously the passivation quality of the photolithographically processed front side is good. In spite of equal processing, the Sputter 1 cell exhibits an IQE decreasing to $IQE_{350} = 0.71$, thus indicating stronger emitter or surface recombination. Obviously the sputtered doping precursor does not allow for a passivation equal to P250. The even lower Quantum Efficiency values of $IQE_{350} = 0.36$ in the case of P508 and $IQE_{350} = 0.42$ for Sputter 2 are primarily due to the simple front side process with the silicon nitride layer only applied after the contact evaporation. Thus a good passivation is not achieved. In the long wavelength regime the P250 and Sputter 1 cells exhibit a significantly increased IQE for $\lambda > 1000$ nm, which is due to the point contacted silicon dioxide back side, acting as a reflector.

Analysis

Inspecting both long and short wavelength regime of the Internal Quantum Efficiency, allows for estimating the contribution of bulk and emitter to the total recombination current in a solar cell. Thus, the limiting factor can be identified. Using Eq. 2.53 permits to obtain the effective bulk diffusion length L_{eff} from the IQE in the regime 800 nm $< \lambda <$ 1000 nm. From L_{eff} the bulk recombination current density J_{0b} (including recombination at the back surface) is determined as [62]

$$J_{0b} = \frac{q\,D\,n_i^2}{N_A\,L_{eff}} \tag{7.2}$$

Tab. 7.3: The effective diffusion length of the four samples ranges between 160 μm $< L_{eff} <$ 330 μm. Due to their lower base doping concentration the bulk saturation current densities (including rear side recombination) of P250 and Sputter 1 are comparatively higher than the ones of P508 and Sputter 2.

Sample	P250	Sputter 1	P508	Sputter 2
L_{eff} [μm]	330	250	260	160
N_A [10^{16} cm^{-3}]	3.3	3.3	5.5	5.5
J_{0b} [fAcm^{-2}]	340	450	230	370

with N_A the base doping density and D the base diffusion coefficient. Figure 7.14 depicts the inverse IQE of the four cells, together with the corresponding fits to obtain L_{eff}. The resulting values for L_{eff}, as well as the corresponding values for J_{0b} are listed in the compilation of Table 7.3. The lowest L_{eff} = 160 μm is determined for the Sputter 2 sample. However, as the sample only disposes of a full area aluminium back contact, the low value is not surprising. In contrast to that the still low values of L_{eff} = 330 μm for P250 and L_{eff} = 250 μm for Sputter 1 are unexpected, as the samples feature a thermal SiO_2 back side with point contacts. The low effective diffusion lengths point to problems in the oxidation. Indeed P508 has a similar L_{eff} = 260 μm with a fully metallized back contact.

The assessment of the emitter parameters is more difficult and less accurate. Indeed, Eq. 2.54 can be rearranged in order to yield information about the emitter surface recombination velocity

$$S_E = \frac{D_E(1 - IQE)}{IQE\, d_E - L_{alpha}} \tag{7.3}$$

However a significant uncertainty arises from the fact that the simple equations 2.54 and 7.3 only describe uniform emitters with good accuracy. Diffused emitters with spatially changing D_E only allow for a rough estimation. Nevertheless, such an estimation will be conducted in the following.

Table 7.4 lists the parameters assumed for the calculation of S_E, as well as the resulting S_E and J_{0e}. The assumed values for the surface concentration C_s and the emitter depth d_E bear the highest uncertainties. For P508 and Sputter 2, values from SIMS measurements with comparable sheet resistance are used (Figs. 5.4, 5.5). For P250, the value for C_s is linearly scaled from the sample with $\rho_s = 178\ \Omega/\Box$ in Fig: 5.3. For Sputter 1 similar values to P250 are assumed, due to the similar sheet

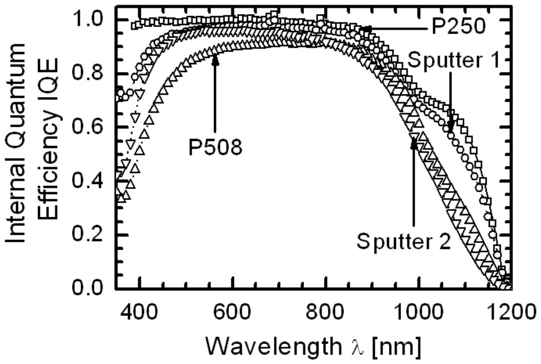

Fig. 7.13: The short wavelength regime shows the strongly differing emitter qualities of the four samples. For P250 the IQE stays close to unity, indicating low emitter and front surface recombination. The Sputter 1 cell displays a drop down to $IQE_{350} = 0.72$, in spite of an equally processed front side. The P508 and Sputter 2 cells only reach $IQE_{350} \approx 0.4$ due to their simple front side process. The reflecting silicon dioxide layer on the back of P250 and Sputter 1 leads to a significantly enhanced IQE for $\lambda > 1000$ nm.

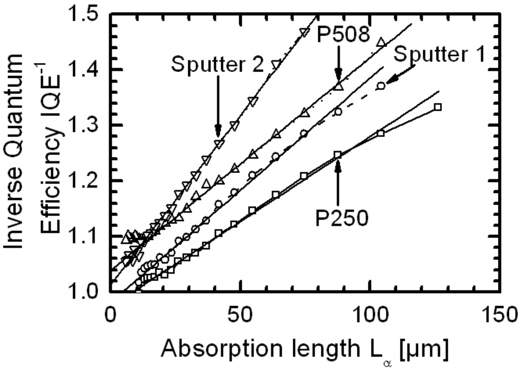

Fig. 7.14: A comparison of the diffusion lengths of the four cells reveals that the passivation quality of the oxide layers (P250, Sputter 1) is rarely superior to the full area back contact of P508 and Sputter 2. Oxide passivation yields $L_{eff} = 250$ μm (Sputter 1) or 330 μm (P250), while full area aluminium yields $L_{eff} = 260$ μm (P508) or 160 μm (Sputter 2).

resistance. For the depth d_E only the emitter part above a concentration $N_D = 10^{19}$ cm^{-3} is considered, as predominantly the highly doped part near the surface of an emitter determines its characteristics. Moreover, the diffusion coefficient $D_E(N_D)$ only varies weakly for $N_D > 10^{19}$ cm^{-3}. Therefore the assumed values for D_E are averaged over the considered emitter depth. The emitter saturation current densities are determined using Eq.2.37, including a Gaussian defect profile with defect lifetime $\tau_{SRH} = 10$ ns.

Clearly, the surface recombination velocity $S_E = 1.4 \times 10^4$ cms^{-1} for P250 is lowest, while for Sputter1 it is augmented 10-fold and even higher for P508 and Sputter 2. Accordingly, $J_{0e} = 120$ fAcm^{-2} for P250 and $680 < J_{0e} < 830$ fAcm^{-2}.

Tab. 7.4: For P250 the values for C_s is obtained by linearly scaling the doping profile of the sample with $\rho_s = 178\ \Omega/\square$ from Fig. 5.3, in order to match the measured $\rho_s = 240\ \Omega/$. As Sputter 1 a similar ρ_s, parameters are assumed. The surface concentration for P508 and Sputter 2 is obtained from comparable doping profiles of Figs. 5.4 and 5.5. For the estimation, only the emitter part down to a doping concentration $N_D = 10^{19}$ cm^{-3} is considered, as predominantly the highly doped part near the surface determines the emitter characteristics. Moreover, $D_E(N_D)$ only varies slowly for $N_D > 10^{19}$ cm^{-3} and is therefore averaged across the considered emitter part.

Sample	P250	Sputter 1	P508	Sputter 2
IQE(350 nm)	0.96	0.71	0.36	0.42
C_s [10^{19} cm^{-3}]	3	3	14	40
d_E (@10^{19}) [nm]	100	100	120	110
D_E [cms^{-2}]	2.6	2.6	2.2	2.0
S_E [10^5 cms^{-1}]	0.12	1.2	3.8	3.2
J_{0e} [fAcm^{-2}]	110	760	830	680

Calculating the open circuit voltages which would be theoretically expected when considering only bulk ($V_{oc,b}$) and additionally emitter recombination ($V_{oc,be}$), reveals the limiting factors for the different cells. The share of the emitter is seen at first glance by comparing $\Delta V_{oc,e} = V_{oc,b} - V_{oc,be}$. Table 7.5 lists the corresponding values, as well as repeating the calculated bulk and emitter saturation current densities used for the calculations, as well as the real, measured open circuit voltages V_{oc}. As expected from the high IQE_{350}, emitter recombination only has a minor impact on V_{oc} for P250. The picture changes for Sputter 1, which displays a significant $\Delta V_{oc,e} = 26$ mV due to J_{0e}. The other two cells P508 and Sputter 2 are both primarily limited by emitter recombination, as $\Delta V_{oc,e} = 28$ mV for Sputter 2 and even $\Delta V_{oc,e} = 39$ mV for P508. As stated above, this high impact is due to the simple front side process. Interestingly for all cells the calculated $V_{oc,be}$ values are higher than the actually measured open circuit voltages. The fact that this difference is significantly larger for the cells with the higher ideality factors could be a hint that they suffer from an additional degradation due to the strong non-idealities.

Tab. 7.5: The upper part of the table repeats the calculated J_{0b} and J_{0e} for easy comparison. The lower part shows the open circuit voltage, when only bulk ($V_{oc,b}$) and additionally emitter recombination ($V_{oc,be}$) are considered. Further the voltage drop $\Delta V_{oc,e}$ due to the emitter recombination is listed, as well as the real, measured voltage V_{oc}.

Sample Parameter	P250	Sputter 1	P508	Sputter 2
J_{0b} [fAcm^{-2}]	340	450	230	370
J_{0e} [fAcm^{-2}]	110	760	830	680
V_{oc} [mV]	638	606	618	619
$V_{oc,b}$ [mV]	657	649	664	652
$V_{oc,be}$ [mV]	650	623	625	624
$\Delta V_{oc,e}$ [mV]	7	26	39	28

7.2.4 Emitter Potential in the Presence of Defects

Section 7.2.2 has shown that laser induced defects do not prevent the obtaining of low emitter saturation current densities, provided a clean doping precursor is used. The preceding section has shown that these emitters are not the main cause for the low solar cell efficiencies achieved in this thesis. In order to gain a better understanding of the potential of solar cells with laser doped emitters, as well as solar cells with defect containing emitters in general, some basic assessment is presented in the following.

For this assessment I assume a high efficiency solar cell structure, with a high lifetime, p-type substrate, and a base doping $N_A = 5 \times 10^{16}$ cm^{-3}. Assuming the base lifetime being limited by Auger recombination and calculating τ_{Auger} using the parametrization of Glunz [31], leads to a bulk lifetime $\tau_b = 275$ μs and a resulting bulk diffusion length $L_b = (D\,\tau_b)^{1/2} = 760$ μm. With this base diffusion length the effective diffusion length [67]

$$L_{eff} = L_b \, \frac{1 + (S_b \frac{L}{D}) \, \tanh(\frac{W}{L_b})}{(S_b \frac{W}{L_b}) + \tanh(\frac{W}{L_b})} \tag{7.4}$$

is obtained with $S_b = 100$ cms^{-1} the assumed back surface recombination velocity, $W = 250$ μm the assumed cell thickness and $D = 21$ cm^{2}s^{-1} the base diffusion coefficient. Using Eq. 7.2 the base saturation current density $J_{0b} = 54$ fAcm^{-2} is determined from L_{eff}.

The impact of emitter defects on J_{0e} is calculated for Gaussian emitters with four different surface concentrations $C_s = 1,\ 2,\ 5 \times 10^{19}$ cm^{-3} and 1×10^{20} cm^{-3}. The corresponding emitter depths d_e are adjusted in a way that the resulting sheet resistance $\rho_s = 100\ \Omega/\Box$ for all configurations. The calculations are carried out using Eq.2.37 for defect lifetimes 1 ns $< \tau_{SRH} <$ 100 ns, likewise Gaussian defect profiles and the defect diffusion depth matching d_e. The surface recombination velocity S_f depends on C_s according to $S_f = 10^{16}\ C_s$ [142]. Table 7.6 lists the parameters used for the calculation of the emitter saturation current densities.

Tab. 7.6: The combination of emitter depths d_e and surface concentrations C_s yields emitter sheet resistances $\rho_s = 100\ \Omega/\Box$ for all four cases. The surface recombination velocity S_f is determined using a parametrization of Cuevas [142].

Emitter	E1	E2	E3	E4
C_s [10^{19} cm^{-3}]	1	2	5	10
d_e [nm]	430	290	150	85
S_f [10^3 cms^{-1}]	1	2	5	10

Figure 7.15 presents the emitter saturation current densities J_{0e} versus defect lifetime τ_{SRH}. Clearly, for high lifetimes a low emitter surface concentration is most beneficial, as $J_{0e} \approx 20\ fAcm^{-2}$ for $\tau_{SRH} = 100$ ns. However, as defect lifetimes reduce, they increasingly influence the total emitter recombination. As a consequence, higher surface concentrations together with a more shallow emitter become more and more beneficial for minimizing J_{0e}. Their drawback regarding higher Auger and surface recombination is outweighed by their shallower depth, which at the same time means shallower defect incorporation. For $\tau_{SRH} \approx 5$ ns as determined in this thesis, a surface concentration 2×10^{19} cm^{-3} $< C_s < 5 \times 10^{19}$ cm^{-3} is close to optimum. Figure 7.16 depicts the resulting maximum expected open circuit voltages, considering both, emitter and bulk recombination and assuming a short circuit current density $J_{sc} = 35$ mAcm^{-2} in Eq. 2.43. Using a surface concentration in the above mentioned range should allow for obtaining maximum voltages close to or exceeding $V_{oc} = 680$ mV. Actually, Eisele and Röder [72] impressively corroborated this estimation by fabricating cells with an optimized laser process and passivation layer and $V_{oc} > 670$ mV.

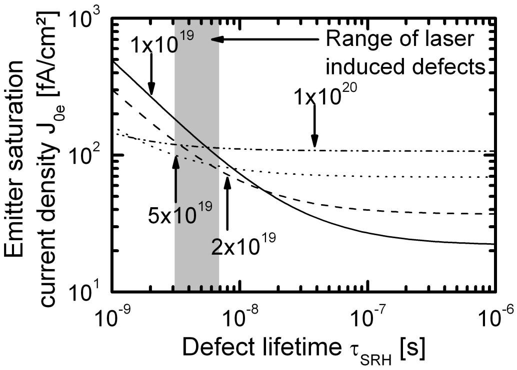

Fig. 7.15: For high defect lifetimes τ_{SRH} a low emitter doping is most beneficial, as it entails low surface and Auger recombination. However, as τ_{SRH} reduces, higher surface concentrations become more and more interesting, as they mean shallower emitter and defect diffusion. For the laser induced defects as determined in this thesis, 2×10^{19} cm^{-3} $< C_s <$ 5×10^{19} cm^{-3} is close to optimum.

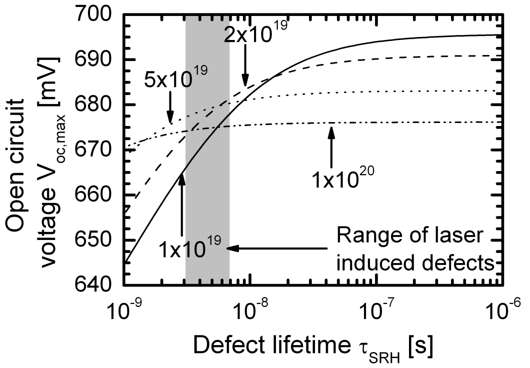

Fig. 7.16: Considering J_{0e} and J_{0b} and assuming $J_{sc} = 35$ mAcm^{-2} the maximum obtainable open circuit voltages are obtained. They follow the evolution of emitter saturation current densities in Fig. 7.15. For laser doped emitters $V_{oc} \approx 680$ mV should be within reach.

7.3 Aluminium Emitters

7.3.1 Experimental

As presented in chapter 5 evaporated aluminium has been examinated as a possible doping precursor for p-type doping in the course of this work. For characterizing the emitters fabricated from aluminium layers, $p^{+}np^{+}$ structures are fabricated on n-type, FZ samples with a base doping $N_D = 6.2 \times 10^{13}$ cm^{-3} and a thickness $w = 525$ μm. The samples are polished on their front and etched on their back side. Their fabrication sequence is as follows:

- Deposition of PECVD-SiO_2 as protecting layer on the sample back
- Short HF-dip
- Evaporation of aluminium (thickness $d_{Al} = 10$ nm) on the front side

- Laser irradiation of front side
- HF-dip for removal of back side protection layer
- Evaporation of aluminium (thickness $d_{Al} = 10$ nm) on the back side
- Laser irradiation of back side
- RCA-clean
- Deposition of $SiN_x (n \approx 3)$ on front and back side

One important observation after the cleaning step which followed the laser irradiation is that the surface of the irradiated region does not turn hydrophobic after the HF-dip, as normally happens on a silicon surface. As already described in chapter 5 the laser doped aluminium surfaces are highly resistant to all employed etchants. Most probably the extremely high surface doping concentration $C_s > 10^{21}$ cm^{-3} measured in most of the samples or possibly the formation of an aluminium oxide is responsible for the change in the surface behaviour after etching. However the non hydrophobic surface status probably also entails a poor surface passivation. Likewise these samples receive laser irradiation in two series ($N_{melt} = 2$ and 20). The applied laser pulse energy density ranges between 0.8 Jcm^{-2} $< D_p <$ 2.0 Jcm^{-2}, identically for both series. Every wafer holds four different sets of laser parameters, distributed on its quarters. After the deposition of the silicon nitride passivation layer the samples are cleaved into quarters and their effective lifetime is measured.

7.3.2 Lifetime data

The figures 7.17 and 7.18 show the results of the lifetime measurements. Both lifetime series exhibit rather low overall lifetimes $\tau_{eff} < 1$ ms, given this lowly doped base material. For $N_{melt} = 2$ the maximum effective lifetimes range between 170 μs $< \tau_{eff} <$ 600 μs, with all curves showing strong linear lifetime decrease as is indicative for emitter recombination. There is no perfectly distinct trend in the succession of the lifetime values, as the curves for $D_p = 0.8$ and 1.0 Jcm^{-2} do not reflect the increase in pulse energy density. The τ_{eff} for the higher pulse energy densities are noticeably lower, however they again lie closely together. This unclear behaviour is probably due to the extremely high doping concentrations of aluminium, which are already achieved at low fluences and in any case cause strong recombination. For 20 melt cycles the lifetime values for $D_p = 0.8$ and 1.0 Jcm^{-2} similar to $N_{melt} = 2$ appear very close together and obtain almost the same absolute τ_{eff} than the samples with two melt cycles. For the higher energy densities the curves differentiate stronger however, showing significantly increasing emitter recombination with stronger irradiation.

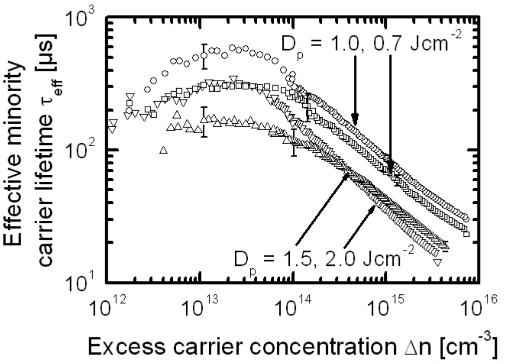

Fig. 7.17: Samples with emitters fabricated from evaporated aluminium precursors and $N_{melt} = 2$ exhibit strong recombination, given their low doping densities of $N_D = 6.2 \times 10^{13}$ cm^{-3}. Their maximum lifetimes come to 170 μs $< \tau_{eff} <$ 600 μs. In log-log scale all curves show linearly decreasing lifetimes towards higher injection densities as typical for emitter recombination. Against expectation the lifetime for $D_p = 0.8$ Jcm^{-2} is lower than for $D_p = 1.0$ Jcm^{-2}, even if the curves lie close together. Probably the extremely high surface concentration of the aluminium emitters (see chapter 5 together with non optimum passivation is responsible for this phenomenon.

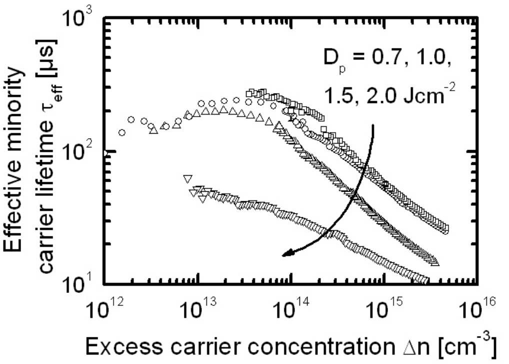

Fig. 7.18: The lifetimes of aluminium samples irradiated with $N_{melt} = 20$ lie within the same range as the lifetimes in figure 7.17. Similarly the curves for $D_p = 0.8$ and 1.0 Jcm^{-2} lie close together but still in the expected succession. The curves for the higher D_p-values differentiate stronger than for $N_{melt} = 2$.

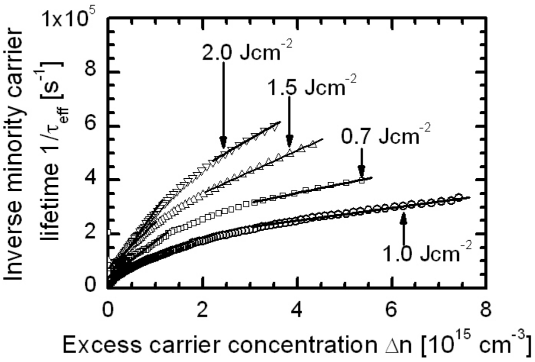

Fig. 7.19: The inverse minority carrier lifetime of the aluminium doped solar cells ($N_{melt} = 2$) exhibit two linear regions when plotted against Δn. For injection densities $\Delta n < 1 \times 10^{15}$ cm^{-3} the slope of the curves is significantly higher than for higher Δn-values.

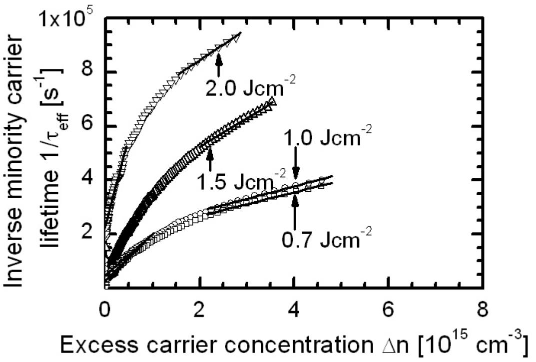

Fig. 7.20: The behavior of the inverse lifetime for doping with $N_{melt} = 20$ is similar to the case of $N_{melt} = 2$. There exist two regions with strongly differing slopes, instead of only one as typical e.g. for furnace phosphorous emitters.

7.3.3 Emitter saturation current density

In order to determine the emitter saturation current densities J_{oe} of the samples once again the method of Cuevas is employed. However, in this case the extraction of J_{oe} from the modified inverse effective lifetime turns out to be difficult, as the inverse lifetimes exhibit an unusual behaviour. A similar finding has already been reported by Kerr [41] for silicon nitride passivated boron emitters. The figures 7.19 and 7.20 depict the problem. Instead of one linear region the curves show two linear regions, with a much higher slope for lower injection densities. Kerr explained this phenomenon by the fixed positive charges which are included in the nitride layers. As they lead to an increase of the electron density at the surface, opposing the electron density decrease caused by the strong p-type doping. Depending on the injection density a situation can occurr where $n \approx p$ resulting in a high surface recombination velocity. Similarly to the measurements of Kerr the inverse lifetimes of the aluminium emitters exhibit two clearly differentiated regions. Figures 7.19 and 7.20 show these values. For injection densities $\Delta n < 1 \times 10^{15}$ cm^{-3} the curves exhibit a significantly stronger slope than for higher Δn-values. As both Δn-ranges are relevant for the operation of a solar cell, depending on the illumination level,

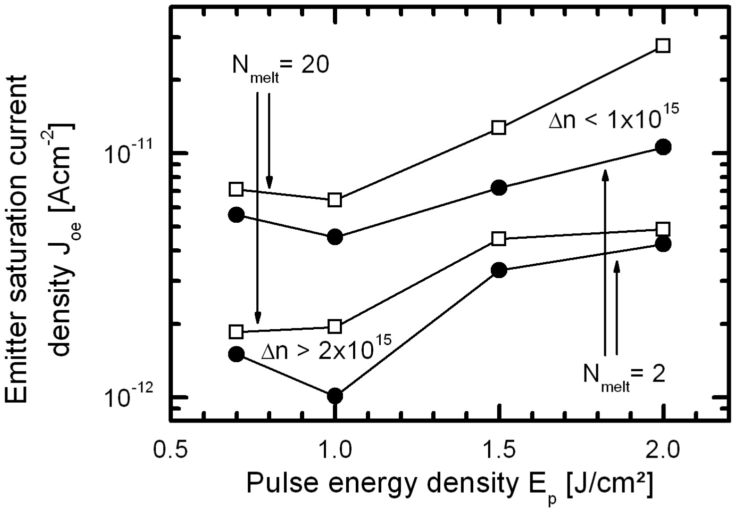

Fig. 7.21: The saturation current densities for aluminium emitters increase with the number of melting cycles as well as the pulse energy density (0.7 Jcm^{-2} < D_p < 2.0 Jcm^{-2}), regardless, whether the value for J_{oe} is extracted from the region $\Delta n < 1 \times 10^{15}$ cm^{-3} or $\Delta n > 2 \times 10^{15}$ cm^{-3}. For the former region the values stretch from 6 pAcm^{-2} < J_{oe} < 10 pAcm^{-2} for $N_{melt} = 2$ and 7 pAcm^{-2} < J_{oe} < 30 pAcm^{-2} for $N_{melt} = 20$. For the latter region the values are lower, ranging between 2 pAcm^{-2} < J_{oe} < 5 pAcm^{-2} for $N_{melt} = 2$ and 20.

an "emitter saturation current density" is extracted from each of the two ranges. The resulting values are depicted in figure 7.21 plotted against the employed laser pulse energy density. In contrast to the phosphorous emitters, plotting J_{oe} against the corresponding ρ_s does not yield any apparent correlations. This fact is not surprising, as the sheet resistance for $d_{Al} = 10\ nm$ was virtually independent of D_p in chapter 5, whereas τ_{eff} indeed changes with the pulse energy density. For all laser parameters the saturation current densities for $N_{melt} = 20$ are higher than for $N_{melt} = 2$, albeit only slightly for $\Delta n > 2 \times 10^{15}$ cm^{-3}. For this injection range the J_{oe}-values increase from $J_{oe} \approx 2$ pAcm^{-2} to $J_{oe} \approx 5$ pAcm^{-2}, with 0.8 Jcm^{-2} < D_p < 2.0 Jcm^{-2}. For $\Delta n < 1 \times 10^{15}$ cm^{-3} the increase goes from $J_{oe} = 6$ pAcm^{-2} to $J_{oe} = 10$ pAcm^{-2} for $N_{melt} = 2$ and from $J_{oe} = 7$ pAcm^{-2} to $J_{oe} \approx 30$ pAcm^{-2} for $N_{melt} = 20$.

7.3.4 Interpretation

The extracted values for the emitter saturation current densities of aluminium emitters are remarkably high and prone to severely influence the efficiency of solar cells produced from aluminium precursors. They reflect the extremely high surface doping concentration achieved with the aluminium precursor layers. This high C_s-values on the one hand cause an extremely low τ_{Aug} inside the emitters, on the other hand probably render the passivation virtually ineffective. The overview in chapter 5 showed aluminium doped solar cells with open circuit voltages $V_{oc} \approx 550$ mV. Extracting the implied open circuit voltage from the above lifetime measurements allows for an estimation of the maximum V_{oc} that these emitters would allow. Figure 7.22 depicts these values, showing that definitely the emitter recombination is limiting the open circuit voltage in the cells fabricated from aluminium precursors. For $N_{melt} = 2$ the maximum achievable voltages range between 545 mV $< V_{oc,impl} <$ 572 mV, with a slight decrease towards higher pulse energy densities. For 20 melt cycles the values for $D_p = 0.8$ and 1.5 Jcm^{-2} are almost equal at $V_{oc,impl} \approx 540$ mV, with $V_{oc,impl} = 554$ mV for $D_p = 1.0$ Jcm^{-2} and a low value of only $V_{oc,impl} = 505$ mV for the highest pulse energy density.

As apparent from the above results, aluminium precursors in the examined configuration are not suited for the fabrication of large doped areas in solar cells because of their extremely high recombination. Also an experiment trying to lower the doping concentration by "diluting" the evaporated aluminium with previously deposited amorphous silicon, did yield similar doping densities after the irradiation. On the other hand, when reducing the area coverage fraction of the aluminium doped regions still reasonable or even good solar cell efficiencies should be realizable. Evidence for the feasibility of using aluminium for local doping are e.g. given in [143] or [144], who used local aluminium doping for the formation of either local BSF structures ("Laser Fired Contacts") or local back emitters ("Laser Fired Emitters"). In both cases, the area coverage fraction $f_A < 5$ % and therefore the corresponding contribution of the recombination in the aluminium doped regions was reduced.

7.4 Chapter Summary

The characterization of laser irradiated furnace diffused emitters shows that the laser treatment increases the saturation current density. The impact on J_{oe} rises with both higher pulse energy density D_p, as well as higher melt repetitions N_{melt}.

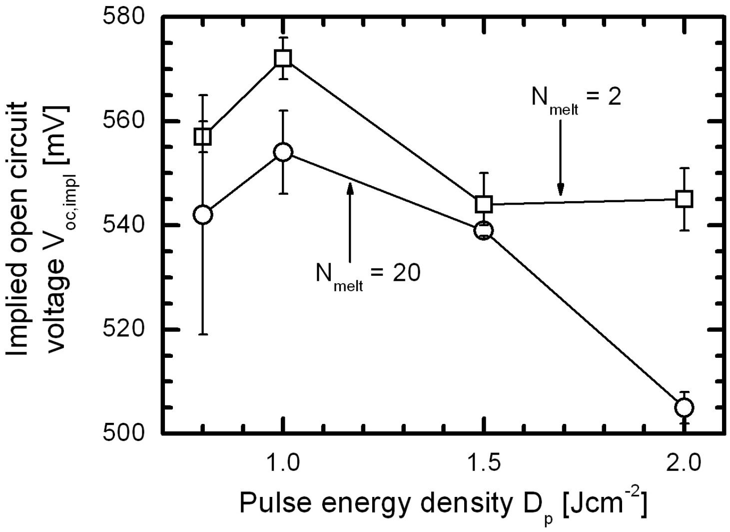

Fig. 7.22: The values for the implied open circuit voltage $V_{oc,impl}$ extracted from the lifetime measurements of the emitter test samples show that the high emitter recombination strongly limits the solar cell efficiency. For $N_{melt} = 2$ the implied voltages range between 545 mV $< V_{oc,impl} <$ 572 mV, with lower values towards higher pulse energy densities. For $N_{melt} = 20$ the values are even lower, only reaching $V_{oc,impl} = 554$ mV at $D_p = 1.0$ Jcm^{-2} as a maximum and only $V_{oc,impl} = 505$ mV for $D_p = 2.0$ Jcm^{-2}.

However, for low to moderate pulse energy densities and $N_{melt} = 2$, the impact on the emitter saturation current density is small and the J_{oe}-values measured after laser irradiation would still allow for the fabrication of high efficiency solar cells. SIMS characterization of the samples reveals that the laser irradiation on the one hand alters the phosphorous doping profile and on the other hand leads to an incorporation of C and O, as was the case for the lifetime samples. A comparison of the measured emitter saturation current densities J_{oe} and values $J_{oc,calc}$, which were theoretically calculated from the measured doping profiles, yields an estimated value for the local lifetime inside the laser affected layers of 3 ns $< \tau_{SRH} <$ 7 ns. These laser induced defects set a limit to the performance of suchlike treated emitters. An analysis of two liquid doping precursors shows that the achievable J_{oe}-values depend strongly on the employed precursor. Whereas the P250 precursor yields saturation current densities well below $J_{oe} = 100$ fAcm^{-2}, the P508 precursor results in values increased at least by a factor of 5. Analyzing the doping profiles of the corresponding samples shows that the origin for this increased saturation current densities must lie in the ingredients of the doping liquid. Sputtered phosphorous doping precursors exhibit intermediate saturation current densities and a different dependence of J_{oe} and the sheet resistance ρ_s.

Solar cells with emitters fabricated from liquid and sputtered phosphorous layers both exhibit strongly differing Quantum efficiencies in the short wavelength regime, pointing to different emitter quality. In accordance with the J_{oe} characterization, a very high emitter quality for the P250 precursor is evident, in contrast to a non optimum emitter in the case of the sputtered precursor and the solar cells with simple front side processing. An assessment of the influence of defects on the quality of different emitters shows that the optimum surface concentration in the presence of defect lifetimes $tau_{SRH} \approx 5$ ns, as determined in this thesis, is 2×10^{19} cm^{-3} $< C_s < 5 \times 10^{19}$ cm^{-3} , for a $\rho_s = 100\ \Omega/\Box$ emitter. Such an emitter, together with high efficiency solar cell processing, should allow for $V_{oc} \approx 680$ mV.

Aluminium emitters generally exhibit a much lower quality and yield saturation current densities in the pA-range. Accordingly, the implied open circuit voltages of these samples only reach maximum values of $V_{oc,impl} \approx 570$ mV. These values match with the measured V_{oc} of solar cells with p-type aluminium emitters and show that the emitter recombination is the limiting factor for the cell efficiency.

Chapter 8

Perspectives for Laser doped Solar Cells

8.1 Summary and Conclusion

This thesis examines the impact of pulsed, specifically focused, green laser irradiation on the electronical properties of p-type silicon and phosphorous diffused n-type emitters. The laser treatment induces a reduction of the effective minority carrier lifetime τ_{eff}, with the magnitude of the reduction being dependent on the employed laser pulse energy density D_p as well as the number of repeated melting cycles N_{melt}. Both, increasing D_p as well as N_{melt} lead to a monotonic reduction of τ_{eff} in laser treated silicon. The irradiation leads to an incorporation of the impurities oxygen, nitrogen and carbon into the silicon, and the magnitude of this incorporation correlates with the observed lifetime reduction. Furthermore, a conductivity type conversion of the processed surface layers points to the formation of laser induced donor-like defects. In spite of the extensive use of various characterization methods, the specific nature of these defects is not unveiled. However, it is probable, that oxygen plays a decisive role in their formation. Considering the low thickness $d <$ 1 μm of the laser treated layers, a low local defect lifetime $\tau_{SRH} <$ 10 ns is required to cause the observed reductions of the effective lifetime.

The study of laser treated, high efficiency phosphorous furnace diffused emitters shows that laser irradiation increases the recombination inside the emitters. A comparison of the measured emitter saturation current densities J_{oe} after irradiation, with theoretically calculated values $J_{oe,calc}$, taking into account laser induced defects, yields a lifetime range for these defects of 3 ns $< \tau_{SRH} <$ 7 ns, which matches the value found for the irradiated, undiffused silicon. However, choosing optimized laser parameters keeps the associated rise of the emitter saturation current density J_{0e} low. An examination of different liquid and sputtered Phosphorous doping precursors reveals that in the majority of cases the laser induced defects only have a minor impact on the recombination in laser diffused emitters. Simulating the performance of different emitters in the presence of defects shows, that the optimized emitter surface concentration C_s for the defect lifetime range determined in this thesis, is 2×10^{19} cm^{-3} $< C_s < 5 \times 10^{19}$ cm^{-3}. At the same time, maximum achievable open circuit voltages $V_{oc} \approx 680$ mV for solar cells with laser diffused emitters are predicted. A recent publication of subsequent work confirms this prediction.

Solar cells with laser diffused phosphorous emitters fabricated in the course of this thesis mostly suffer from unusually high ideality factors, which degrade their Fill Factors and open circuit voltages. Evaluating the measured quantum efficiency of selected cells shows that even the highest achieved $V_{oc} = 637$ mV is not limited by the laser emitter.

Additionally this thesis also examines the feasibility of aluminium as precursor for the fabrication of p-type emitters. The laser irradiation leads to a massive Al incorporation up to concentrations $C_{Al} > 10^{21}$ cm^{-3}. However, the dopant activation is low and most of the incorporated aluminium seems to form a very resistant surface layer, which withstands etch attack. Emitters fabricated with Al exhibit saturation current densities $J_{oe} >> 1$ pAcm^{-2}. Consequently solar cells with Al emitters only reach open circuit voltages $V_{oc} \approx 550$ mV and show low efficiencies $\eta \approx 7$ %.

In conclusion, this thesis shows that the defects which are generated by the *ipe* laser doping process, are not limiting the performance of solar cells fabricated with this process. Further, the simple experiments presented, allow for an assessment of the magnitude of lifetime reductions caused by using different types of laser systems for laser doping.

8.2 Outlook - Potentials and Limitations

Since the time I started this thesis, the photovoltaic industry has taken giant steps towards maturity and the prospect of "grid parity" for photovoltaics, which had been the dream of idealists just some years ago, is earnestly predicted for the very near future. In order to achieve this taks, "Euro per Watt" is the paramount driving factor, i.e. increasing the cell efficiency and at the same time lowering production cost. In order to do so, new production steps are necessary and laser doping can be a key process for some of them. Therefore and to conclude this work, I will take a glance at a number of new PV production processes and try to assess, which role laser doping can play in them.

8.2.1 Front Side Processes

Selective Emitter

The Selective Emitter (SE) concept has already been known for a long time [10]. Selective doping beneath the front contact gridlines allows for increasing the emitter sheet resistance between the contacts, thus allowing for a better blue response of the cell. At the same time, the contact resistance is enhanced and the local doping additionally reduces the contact recombination. At the moment there are several laser based, laser assisted or not laser assisted concepts being developed. However, introducing them into series production requires more or less costly modifications of the existing line concept.

Laser Based Concepts. The *ipe* SE concept [102, 103] requires the introduction of only one additional processing step into a standard cSi production line. Thus it is the simplest of the currently discussed concepts. An absolute efficiency gain $\Delta\eta \geq 0.4$ % has already been shown in an industrial environment [111]. Furthermore, laser systems allowing for high production cycle times are already commercially available[1]. A drawback is the necessity for exact alignment of the subsequent metallization step, as this process is not compatible with self aligned, plated metallization. In spite of this disadvantage the concept is most securely one of the most promising for fast industrialization and is currently being commercialized by the company Manz.

The Fraunhofer ISE together with the company Synova presented the so called "Laser Chemical Processing", which elegantly combines precursor application and laser doping in one step [7]. The succseful fabrication of high efficiency solar cells has already been reported [8]. However, no results from efficiency gain in an industrial environment are available, yet. Moreover, the technology is extremely complex and can only exploit its full potential in combination with self aligned metallization

---

[1] Estimation of necessary laser power: Assuming a solar cell with $N_{contact} = 80$ contact lines and a line width of $w_{contact} = 200\ \mu m$ yields an area $A = 25$ cm^{-2} to be processed. The laser power at a reasonable fluence $D_p = 3$ Jcm^{-2} and a cycle time $t_{cyc} = 1.5$ s amounts up to $P_{Laser} \approx 50$ W (without losses considered).

(direct plating on silicon), which requires a complete modification of the standard cSi production line concept.

The University of New South Wales [5,6] published an SE concept using a doping precursor (even if that is not explicitly said). Therefore most securely three additional processing steps (precursor application, laser, precursor cleaning) need to be introduced. Like the ISE/Synova concept, the process is most beneficial for self aligned metallization. In contrast to that concept, the need for separate precursor application and removal makes the UNSW approach more cumbersome at first sight. On the other hand, the high complexity of the Synova concept can be avoided. The necessary laser power is expected to be in the same range as for the *ipe* process.

Laser Assisted Concepts. Most laser assisted SE concept use the laser for structuring a diffusion barrier or masking layer, in order to define the heavily and lightly doped emitter areas(e.g. [145,146]). All of these concepts at least require three additional steps (mask application, structuring, mask removal), while some of them even work with two individual diffusion steps. While one of these approaches is currently being commercialized by the company Centrotherm [147] the others still seem to be in a laboratory phase.

Other Concepts. Most of the other SE concepts use printed barrier layers or etchants for the structuring of the diffusion barriers (e.g. [148]). Like the laser assisted concepts, they require several additional processing steps.

Full Area Front Side Emitter

In spite of the considerable effort spent on optimizing and characterizing completely laser doped front side emitters, it seems improbable that this process will be implemented. Although the inhomogeneity problems, as reported in [58, 99, 111] and also encountered in this thesis, can be overcome [72], the technological complexity to assure a perfectly tailored focus on the silicon surface, as well as the fact that the laser damages the light-trapping surface texture constitute severe problems. Moreover, a fast processing of full area emitters would require laser powers far in excess of the currently available systems.

8.2.2 Back Side Processes

Currently, the standard cSi solar cell features a screen printed aluminium back contact. However, as the substrate thickness reduces, the recombination at the back contact as well as the mediocre reflectivity of the AL-BSF increasingly limits the cell performance. Therefore mostly dielectrically passivated back surfaces are discussed [52]. A number of laser based or assisted processes have already been published in the context of advanced back contacts, such as Laser Fired Contacts [69] or local laser ablation [70]. Here, the application of the *ipe* laser doping process for creating local, highly doped regions could be imagined. However, the feasibility of possible dopants (Boron, Aluminium), as well of cell structures needs further research.

8.2.3 New Cell Structures

Apart from the above mentioned evolutionary improvements of the current industry standard, there also exist several approaches, which use completely different cell structures, mostly all back side contacted like "Interdigitated Back Contact" (IBC) [149], or "Emitter Wrap Through" (EWT) [150]. Above all for the IBC structure, laser doping could be an elegant way to realize the closely spaced, localized diffusions needed for high cell efficiencies. Such a process has already been tried at *ipe* [151]. One of the key problems for such a structure is again the alignment of diffused areas and the subsequent metallization.

8.2.4 Rating

The preceding overview shows, that for laser doping a huge and concrete potential exists in the realization of selectively doped structures on the solar cell front side. As the selective emitter will securely be one of the next improvements for cSi solar cells, the implementation of the *ipe* laser doping process is highly probable. An application beyond the SE will require more research regarding alternative doping precursors together with the development of corresponding solar cell structures.

Appendix A

Parametrizations for Auger recombination

In the literature there exist a number of slightly different parametrizations for the injection dependent Auger recombination. The most recent one is the parametrization of Kerr [32], which determines the Auger lifetime as

$$\tau_{Aug,Kerr} = \frac{\Delta n}{np\left(1.8 \times 10^{-24} n_0^{0.65} + 6 \times 10^{-25} p_0^{0.65} + 3 \times 10^{-27} \Delta n^{0.8}\right)} \tag{A.1}$$

However, as found in the thesis of Dauwe [152], as well as during the interpretation of measurement results of this thesis, the parametrization of Kerr sometimes yields too high values for the Auger lifetime. A different parametrization, is therefore used in this thesis. It was found by Glunz et.al. [31], and yields the Auger recombination rate as

$$\tau_{Aug,Glunz} = \frac{\Delta n}{C_n * \left(n^2 p - n_0^2 p_0\right) + C_p^* \left(np^2 - n_0 p_0^2\right)} \tag{A.2}$$

using

$$C_n^* = g_{eeh} C_n \left(\frac{n_0}{n_0 + \Delta n}\right) + \frac{C_a}{2}\left(\frac{\Delta n}{n_0 + \Delta n}\right) \tag{A.3}$$

and

$$C_p^* = g_{ehh} C_p \left(\frac{p_0}{p_0 + \Delta p}\right) + \frac{C_a}{2}\left(\frac{\Delta p}{p_0 + \Delta p}\right) \tag{A.4}$$

The quantities $C_n = 2.8 \times 10^{31}\ cm^6 s^{-1}$, $C_p = 9.9 \times 10^{-32}\ cm^6 s^{-1}$ and $C_a = 1.66 \times 10^{-30}\ cm^6 s{-}1$ denote the Auger coefficients. Further, the parametrization requires the so called "Coulomb enhancement coefficients"

$$g_{eeh} = 1 + 44\, 1 - \tanh\left[\left(\frac{N_D}{5 \times 10^{16}\ cm^{-3}}\right)^{0.34}\right] \tag{A.5}$$

and

$$g_{ehh} = 1 + 44\, 1 - \tanh\left[\left(\frac{N_A}{5 \times 10^{16}\ cm^{-3}}\right)^{0.29}\right] \tag{A.6}$$

Further comparison of different parametrizations is also found in [41].

Appendix B

Abbreviations

a-Si	Amorphous silicon
BGN	Band Gap Narrowing
BSF	Back Surface Field
CdTe	Cadmium Telluride
CIGS	Copper Indium Gallium Selenide
CIS	Copper Indium Sulfite
EWT	Emitter Wrap Through
FCA	Free Carrier Absorption
FZ	Float Zone
IBC	Interdigitated Back Contact
MOS	Metal Oxide Semiconductor
MPP	Maximum Power Point
MWT	Metal Wrap Through
QFN	Quasi Fermi Niveau
SE	Selective Emitter
SiN_x	Silicon Nitride
SiO_2	Silicon Dioxide
SRH	Shockley Read Hall
SRV	Surface Recombination Velocity

Appendix C

Physical Constants

c_0	Speed of light in vacuum	2.998×10^{8} ms^{-1}
h	Planck´s constant	6.634×10^{-34} Js
k_B	Boltzman´s constant	1.38×10^{-23} JK^{-1}
q	Elementary charge	1.602×10^{-19} As

Symbols

α_0	Band to band silicon absorption coefficient	cm^{-1}
α_{eff}	Effective absorption coefficient	cm^{-1}
α_{LHe}	Liquid helium temperature infrared absorption coefficient	cm^{-1}
α_{RT}	Room temperature infrared absorption coefficient	cm^{-1}
$\Delta\omega_{\mathrm{abs}}$	FWHM peak width of infrared absorption	nm^{-1}
ΔA_{s}	Surface area increase due to laser melting	
$\Delta E_{\mathrm{g}}^{app}$	Apparent band gap narrowing	eV
$\Delta n, \Delta p$	Excess electron / hole density	cm^{-3}
Δn_{avg}	Average excess charge carrier density	cm^{-3}
Δx	Distance between scanned columns during laser doping	μm
Δy	Distance between single laser pulses during laser doping	μm
Δz	Depth of focus	μm
η	Solar cell efficiency	
κ_{Si}	Thermal conductivity of silicon	$\mathrm{Wcm}^{-1}\mathrm{K}^{-1}$
λ	Wavelength	nm
λ^{-1}	Wavenumber	nm^{-1}
ν	Light frequency	Hz
A	Scaling / activation factor for doping profiles	

A_{abs}	Absorption	
A_{strike}	Surface area hit by gas molecules during laser melting	
B	Radiative recombination coefficient	$\mathrm{cm}^{-3}\mathrm{s}^{-1}$
C_0	Dopant solubility limit in thermodynamical equilibrium	cm^{-3}
C_{L}	Laser doping induced impurity concentration	cm^{-3}
$C_{\mathrm{n,p,a}}$	Auger coefficients	$\mathrm{cm}^{6}\mathrm{s}^{-1}$
$C_{\mathrm{O,max}}$	Maximum oxygen concentration	cm^{-3}
C_{s}	Surface doping concentration	cm^{-3}
d_{Al}	Thickness of aluminium doping precursor	nm
d_{etch}	Silicon etching depth	nm
D_{E}	Emitter minority carrier diffusion coefficient	$\mathrm{cm}^{2}\mathrm{s}^{-1}$
d_{e}	Emitter depth	nm
D_{it}	Surface interface trap density	cm^{-2}
d_{O}	Oxygen incorporation depth	nm
$D_{\mathrm{p,avg}}$	Effective average laser pulse energy density	Jcm^{-2}
$D_{\mathrm{p,circ}}$	Laser pulse energy density for circular beam	Jcm^{-2}
$D_{\mathrm{p,ell}}$	Laser pulse energy density for elliptical beam	Jcm^{-2}
$D_{\mathrm{p,max}}$	Maximum local pulse energy density in focus center	Jcm^{-2}
$D_{\mathrm{P,s}}, D_{\mathrm{P,l}}$	Phosphorous diffusion coefficient in solid / liquid state	$\mathrm{cm}^{2}\mathrm{s}^{-1}$
D_{part}	Effective fraction of laser pulse energy density	
D_{p}	Laser fluence or pulse energy density	Jcm^{-2}
$D_{\mathrm{th,prec}}$	Ablation threshold energy density for doping precursor	Jcm^{-2}
D_{therm}	Thermal diffusivity	$\mathrm{cm}^{2}\mathrm{s}^{-1}$

D_{th}	Melt threshold energy density	Jcm^{-2}
E	Laser pulse energy	J
$E_{\mathrm{C}}, E_{\mathrm{V}}$	Conduction / valence band energy level	eV
E_{g}	Band gap energy distance	eV
E_{i}	Intrinsic energy level	eV
E_{PL}	Photon energy	eV
E_{t}	Trap energy level	eV
f	Focal length	mm
f_{p}	Laser pulse repetition frequency	Hz
FF	Solar cell Fill Factor	
$FF_{0,\mathrm{n}}$	Ideality limited Fill Factor	
$FF_{\mathrm{s}}, FF_{\mathrm{p}}$	Fill Factor considering resistive losses	
G	Charge carrier generation rate	s^{-1}
G_{av}	Average charge carrier generation rate	s^{-1}
h_{s}	Height of laser induced surface structure	nm
I, I_0	Light intensity, incident intensity	Wcm^{-2}
J_{01}, J_{02}	Solar cell saturation current densities	Acm^{-2}
$J_{0\mathrm{b}}$	Bulk saturation current density	Acm^{-2}
$J_{0\mathrm{e,calc}}$	Calculated theoretical emitter saturation current density	Acm^{-2}
$J_{0\mathrm{e,meas}}$	Measured emitter saturation current density	Acm^{-2}
$J_{0\mathrm{e,ref}}$	Reference emitter saturation current density	Acm^{-2}
$J_{0\mathrm{e}}$	Emitter saturation current density	Acm^{-2}
J_{L}	Light generated current density	Acm^{-2}

J_{mpp}	Current density at MPP	Acm^{-2}
J_{rec}	Recombination current density	Acm^{-2}
J_{sc}	Short circuit current density	Acm^{-2}
k_0	Segregation coefficient in thermal equilibrium	
K_1	Constant for determination of band gap narrowing	meV
K_2	Constant for determination of band gap narrowing	cm^{-3}
k_{B}	8.617×10^{-5}	eV/K
k_{O}	Oxygen segregation coefficient	
l	Long axis (semimajor) of laser focus	μm
L_{α}	Absorption length	cm
L_{therm}	Thermal diffusion length	cm
l_{th}	Semimajor of laser melted surface area	μm
m	Atom / molecule mass	kg
n	Electron concentration	cm^{-3}
n_0	Equilibrium electron concentration	cm^{-3}
n_1, n_2	Ideality factors	
$N_{\mathrm{C}}, N_{\mathrm{V}}$	Effective density of states of conduction / valence band	cm^{-3}
N_{dop}	Doping concentration	cm^{-3}
N_{D}	Donor concentration	cm^{-3}
N_{fcc}	Concentration of free charge carriers	cm^{-3}
n_{i}	Intrinsic carrier concentration in silicon	cm^{-3}
n_{loc}	Local ideality factor	
N_{melt}	Number of melting cycles	

N_{O}	Number of incorporated oxygen atoms	
N_{p0}	Number of incident photons	
N_{strike}	Number of atoms / molecules striking the silicon surface during laser melting	
n_{s}	Electron surface concentration	cm^{-2}
O_{p}	Laser pulse overlap	%
P	Power	W
p	Hole concentration	cm^{-3}
p_0	Equilibrium hole concentration	cm^{-3}
p_{gas}	Gas pressure	bar
p_{s}	Hole surface concentration	cm^{-2}
q	1.6×10^{-19}	As
BPP	Beam Parameter Product	
EQE	External Quantum Efficiency	
IQE	Internal Quantum Efficiency	
M^2	Characteristic parameter for laser beam M^2	

List of Publications

1. M. Ametowobla, J.R. Köhler, A. Esturo-Bretón and J.H. Werner, *Proc. 22nd European Photovoltaic Solar Energy Conference*, edited by W. Palz, H. Ossenbrink, (WIP Munich, Germany, 2007), 1403
2. M. Ametowobla, J.R. Köhler, A. Esturo-Bretón and J.H. Werner, *Proc. 21st European Photovoltaic Solar Energy Conference*, edited by J. Poortmanns, H. Ossenbrink, E. Dunlop, P. Helm, (WIP Munich, Germany, 2006), 1440
3. M. Ametowobla, A. Esturo-Bretón, J.R. Köhler and J.H. Werner, *Proc. 31st IEEE Photovoltaic Specialists Conference*, (IEEE, Piscatway, USA, 2005), 1277
4. S. Eisele, T. Röder, M. Ametowobla, G. Bilger, J.R. Köhler, J.H. Werner, *Proc. 34th IEEE Photovoltaic Specialists Conference*, (IEEE, Piscatway, USA, 2009)
5. S. Eisele, M. Ametowobla, G. Bilger, J.R. Köhler, J.H. Werner, *Proc. 23rd European Photovoltaic Solar Energy Conference*, edited by D. Lincot, H. Ossenbrink, (WIP Munich, Germany, 2008), 1737
6. S. Eisele, G. Bilger, M. Ametowobla, J.R. Köhler, J.H. Werner, *Proc. 17th International Photovoltaic Science and Engineering Conference*, (Fukuoka, Japan, 2007)
7. C. Carlsson, A. Esturo-Bretón, M. Ametowobla, J.R. Köhler, and J.H. Werner, *Proc. 21st European Photovoltaic Solar Energy Conference*, edited by J. Poortmanns, H. Ossenbrink, E. Dunlop, P. Helm, (WIP Munich, Germany, 2006), 938
8. A. Esturo-Bretón, M. Ametowobla, C. Carlsson, J.R. Köhler, and J.H. Werner, *Proc. 21st European Photovoltaic Solar Energy Conference*, edited by J. Poort-

manns, H. Ossenbrink, E. Dunlop, P. Helm, (WIP Munich, Germany, 2006), 1247

9. A. Esturo-Bretón, M. Ametowobla, J.R. Köhler, and J.H. Werner, *Proc. 20th European Photovoltaic Solar Energy Conference*, edited by W. Palz, H. Ossenbrink, P. Helm, (WIP Munich, Germany, 2005), 851

10. J.R. Köhler, M. Ametowobla and A. Esturo-Bretón, *Proc. 20th European Photovoltaic Solar Energy Conference*, edited by W. Palz, H. Ossenbrink, P. Helm, (WIP Munich, Germany, 2005), 1162

Bibliography

[1] , European Photovoltaic Industry Association, Press Release (2009).

[2] A. Esturo-Bretón, J. Köhler, J. Werner, *Proc. 13th Workshop on Crystalline Silicon Solar Cell Materials and Processes* (NREL, Golden, Colorado, USA, 2003), 186.

[3] J. Köhler, M. Ametowobla, A. Esturo-Bretón, J. Werner, *Proc. 20th European Photovoltaic Solar Energy Conference*, edited by H. Ossenbrink (WIP Munich, 2005), 1162.

[4] T. Röder, P. Grabitz, S. Eisele, C. Carlsson, J. Köhler, J. Werner, *Proc. 34th IEEE Photovolt. Spec. Conf.* (IEEE, Piscatway, 2009).

[5] B. Tjahjono, J. Guo, Z. Hameiri, *Proc. 22nd European Photovoltaic Solar Energy Conference*, edited by W. Palz H. Ossenbrink (WIP Munich, Germany, 2007), 966.

[6] B. Tjahjono, S. Wang, A. Sugianto, *Proc. 23rd European Photovoltaic Solar Energy Conference*, edited by W. Palz H. Ossenbrink (WIP Munich, Germany, 2008), 1995.

[7] D. Kray, A. Fell, S. Hopmann, K. Mayer, M. Mesec, S. Glunz, G. Willeke, *Proc. 22nd European Photovoltaic Solar Energy Conference*, edited by W. Palz H. Ossenbrink (WIP Munich, Germany, 2007), 1227.

[8] D. Kray, M. Aleman, A. Fell, S. Hopmann, K. Mayer, M. Mesec, R. Müller, G. Willeke, S. Glunz, B. Bitnar, D.-H. Neuhaus, R. Lüdemann, T. Schlenker, D. Manz, A. Bentzen, E. Sauar, A. Pauchard, B. Richerzagen, *Proc. 33rd IEEE Photovolt. Spec. Conf.* (IEEE, Piscatway, 2008), 1.

[9] S. Sze, *Physics of Semiconductor Devices* (Wiley, Inc., 1983).

[10] M. Green, *High Efficiency Silicon Solar Cells* (Trans Tech Publications, Aedermannsdorf, 1987).

[11] P. Altermatt, J. Schumacher, A. Cuevas, M. Kerr, S. Glunz, R. King, G. Heiser, A. Schenk, J. Appl. Phys. **92**, 3187 (2002).

[12] D. Klaassen, J. Slotboom, H. de Graaff, Solid State Electron. **35**, 125 (1992).

[13] A. Cuevas, P. Basore, G. Giroult-Matlakowski, C. Dubois, J. Appl. Phys. **80**, 3370 (1996).

[14] P. Basore D. Clugston, *PC1D Version 5.9*, University of New South Wales, Sydney, Australia (2003).

[15] S. Swirhun, J. del Alamo, R. Swanson, IEEE Trans. El. Dev. **7**, 168 (1986).

[16] F. Lindholm, A. Neugroschel, C.-T. Sah, M. Godlewski, H. Brandhorst, IEEE Trans. El. Dev. **ED-24**, 402 (1977).

[17] M. Green, *Solar Cells* (Prentice Hall Inc., Englewood Cliffs, USA, 1982).

[18] *Properties of Silicon*, INSPEC, London (1988), EMIS Datareview Series No. 4.

[19] M. von Allmen, *Laser-Beam Interactions with Material* (Springer Verlag, 1987).

[20] M. von Allmen, *Laser Annealing of Semiconductors*, edited by J. M. Poate J. W. Mayer (Academic Press, 1982).

[21] W. Spitzer H. Fan, Phys. Rev. **108**, 268 (1957).

[22] S. Sze, *Physics of Semiconductor Devices* (Wiley, Inc., 1983).

[23] D. Bäuerle, *Laser Processing and Chemistry* (Springer, Berlin, Germany, 2000).

[24] R. Dassow, *Laserkristallisation von Silizium*, Phd thesis, Universität Stuttgart (2001).

[25] D. Schroder, IEEE Trans. El. Dev. **44**, 160 (1997).

[26] W. van Roosbroeck W. Shockley, Phys. Rev. **44**, 1558 (1954).

[27] H. Schlangenotto, H. Maeder, W. Gerlach, Phys. Stat. Sol. **21a**, 357 (1974).

[28] J. Dziewior W. Schmid, Appl. Phys. Lett. **31**, 346 (1977).

[29] A. Hangleiter R. Häcker, J. Appl. Phys. **75**, 7570 (1994).

[30] P. Altermatt, J. Schmid, G. Heiser, A. Aberle, J. Appl. Phys. **82**, 4938 (1997).

[31] S. Glunz, A. Sproul, W. Warta, W. Wettling, J. Appl. Phys **75**, 1611 (1994).

[32] M. Kerr A. Cuevas, J. Appl. Phys. **91**, 2473 (2002).

[33] W. Shockley W. Read, Phys. Rev. **87**, 835 (1952).

[34] R. Hall, Phys. Rev. **87**, 387 (1952).

[35] W. Shockley, Phys. Rev. **56**, 317 (1939).

[36] W. Mönch, *Semiconductor Surfaces and Interfaces* (Springer-Verlag, Berlin Heidelberg, 2001).

[37] J. G. Fossum M. A. Shibib, IEEE Trans. El. Dev. **ED-28**, 1018 (1981).

[38] D. Kane R. Swanson, Phys. Rev. **101**, 1264 (1956).

[39] S. Sze, *Physics of Semiconductor Devices* (Wiley, Inc., 1983).

[40] A. Cuevas, Sol. En. Mat. Sol. Cells **57**, 277 (1999).

[41] M. Kerr, *Surface, Emitter and Bulk Recombination in Silicon and Development of Silicon Nitride Passivated Solar Cells, p. 157*, Phd thesis, Australian National University, Canberra, Australia (2002).

[42] A. Sproul, J. Appl. Phys. **76**, 2851 (1994).

[43] J. Brody, A. Rohatgi, A. Ristow, Sol. En. Mat. Sol. Cells **77**, 293 (2003).

[44] H. Nagel, B. Lenkeit, R. Sinton, A. Metz, R. Hezel, *Proc. 16th European Photovoltaic Solar Energy Conference*, edited by W. Palz H. Ossenbrink (WIP Munich, 2000), 93.

[45] A. Cuevas, R. Merchan, J. Ramos, Trans. El. Dev. **40**, 1181 (1993).

[46] A. Cuevas M. Balbuena, Trans. El. Dev. **36**, 553 (1989).

[47] J. Del Alamo R. Swanson, IEEE Trans. El. Dev. **31**, 1878 (1984).

[48] M. Shibib, F. Lindholm, F. Therez, IEEE Trans. El. Dev. **26**, 959 (1979).

[49] F. Bisschop, L. Verhoef, W. Sinke, IEEE Trans. El. Dev. **37**, 358 (1990).

[50] J. Park, A. Neugroschel, F. Lindholm, IEEE Trans. El. Dev. **33**, 240 (1986).

[51] M. Green, *High Efficiency Silicon Solar Cells* (Trans Tech Publications, Aedermannsdorf, 1987).

[52] S. Glunz, Advances in OptoElectronics **2007**, ID 97370 (2007).

[53] M. Schöfthaler, R. Brendel, G. Langguth, J. Werner, *Proc. 1st IEEE World Conf. Photovolt. En. Conv.* (IEEE, Piscatway, 1994), 1509.

[54] J. H. Werner, *Photovoltaics*, Lecture notes, University of Stuttgart, Germany (2005).

[55] K. McIntosh, *Lumps, humps and bumps: Three detrimental effects in the current-voltage curve of silicon solar cells*, Phd thesis, University of New South Wales, Sydney, Australia (2001).

[56] O. Breitenstein, P. Altermatt, K. Ramspeck, A. Schenk, *Proc. 21st European Photovoltaic Solar Energy Conference*, edited by O. H. (WIP Munich, 2006), 625.

[57] O. Breitenstein, M. Langenkamp, J. Rakotoniaina, J. Zettner, *Proc. 17th European Photovoltaic Solar Energy Conference*, edited by O. H. (WIP Munich, 2001), 1499.

[58] A. Esturo-Bretón, M. Ametowobla, J. Köhler, J. Werner, *Proc. 20th European Photovoltaic Solar Energy Conference*, edited by H. Palz, H. Ossenbrink, P. Helm (WIP Munich, 2005), 851.

[59] K. McIntosh, *Lumps, humps and bumps: Three detrimental effects in the current-voltage curve of silicon solar cells*, Phd thesis, University of New South Wales, Sydney, Australia (2001).

[60] K. McIntosh, P. Altermatt, G. Heiser, *Proc. 16th European Photovoltaic Solar Energy Conference*, edited by W. Palz H. Ossenbrink (WIP Munich, 1996), 251.

[61] J. Werner, Appl. Phys. A **47**, 291 (1988).

[62] M. Green, *Solar Cells* (Prentice Hall Inc., Englewood Cliffs, USA, 1982).

[63] A. Mette, *New Concepts for Front Side Metallization of Industrial Solar Cells*, Phd thesis, University of Freiburg, Germany (2007).

[64] A. Aberle, S. Wenham, M. Green, *Proc. 23rd IEEE Photovolt. Spec. Conf.* (IEEE, Piscatway, 1993), 133.

[65] J. Dicker, *Analyse und Simulation von hocheffizienten Silizium-Solarzellenstrukturen für industrielle Fertigungstechniken*, Phd thesis, University of Konstanz, Germany (2003).

[66] A. Rohatgi, J. Davis, R. Hopkins, P. Rai-Choudhury, P. McMullin, J. McCormick, Sol. St. Electron. **23**, 415 (1980).

[67] P. Basore, IEEE Trans. El. Dev **ED-37**, 337 (1990).

[68] H. Hovel, *Semiconductors and Semimetals*, edited by R. Willardson A. Beer (Academic Press, New York, 1975).

[69] E. Schneiderlöchner, *Laserstrahlverfahren zur Fertigung kristalliner Silizium-Solarzellen*, Phd thesis, Universität Freiburg (2004).

[70] P. Engelhart, N.-P. Harder, T. Horstmann, Grischke, R. Meyer, R. Brendel, *Proc. 4th World Conference on Photovolt. Energy Conversion* (IEEE, Piscatway, 2006), 236.

[71] N. Mingirulli, S. Trittler, M. Bui, A. Grohe, D. Biro, R. Preu, S. Glunz, *Proc. 23rd European Photovoltaic Solar Energy Conference*, edited by W. Palz H. Ossenbrink (WIP Munich, 2008), 996.

[72] S. Eisele, T. Röder, M. Ametowobla, G. Bilger, J. Köhler, J. Werner, *Proc. 34th IEEE Photovolt. Spec. Conf.* (IEEE, Piscatway, 2009).

[73] H. Hügel, *Strahlwerkzeug Laser* (Teubner, 1992).

[74] F. Kneubühl M. Sigrist, *Laser* (Vieweg+Teubner, 2008).

[75] D. Meschede, *Optics, Light and Lasers* (Wiley, 2004).

[76] R. Sinton A. Cuevas, Appl. Phys. Lett. **69**, 2510 (1996).

[77] H. Nagel, C. Berge, A. Aberle, J. Appl. Phys. **86**, 6218 (1999).

[78] J. Brody, A. Rohatgi, A. Ristow, *Proc. 11th Workshop on Crystalline Silicon Solar Cell Materials and Processes* (NREL, Golden, Colorado USA, 2001), 163.

[79] H. Düsterhöft, M. Riedel, B.-K. Düsterhöft, *Einführung in die Sekundärionenmassenspektrometrie (SIMS)* (Teubner, Stuttgart, 2001).

[80] D. Schroder, *Semiconductor Material and Device Characterization* (Wiley, Inc., New York, 1998).

[81] P. Griffiths J. de Haseth, *Fourier Transform Infrared Spectrometry* (Wiley, New York, 2007).

[82] C. White, S. Wilson, B. Appleton, F. Young, J. Appl. Phys. **51**, 738 (1980).

[83] C. White, *Pulsed Laser Processing of Semiconductors*, edited by R. Beer C. Albert (Academic Press, New York, 1984).

[84] C. White, P. Pronko, S. Wilson, B. Appleton, J. Narayan, R. Young, J. Appl. Phys. **50**, 3261 (1979).

[85] R. Wood G. Giles, Phys. Rev. B **23**, 2923 (1981).

[86] R. Wood, J. Kirkpatrick, G. Giles, Phys. Rev. B **23**, 5555 (1981).

[87] R. Wood, Phys. Rev. B **25**, 2786 (1982).

[88] R. Wood, C. White, F. Young, *Semiconductors and Semimetals, Vol.23*, edited by R. Beer C. Albert (Academic Press, New York, 1984).

[89] J. Poate J. Mayer, *Laser Annealing of Semiconductors* (Academic Press, 1982).

[90] D. Debarre, K. G., T. Noguchi, J. Boulmer, IEICE Trans. Electron. **E85-C**, 1098 (2002).

[91] T. Deutsch, D. Ehrlich, D. Rathman, D. Silversmith, R. Osgood Jr., Appl. Phys. Lett. **39**, 825 (1981).

[92] E. Fogarassy, R. Stuck, J. Grob, P. Siffert, J. Appl. Phys. **52**, 1076 (1981).

[93] Y. Wong, X. Yang, P. Chan, K. Tong, Appl. Surf. Sci. **64**, 259 (1993).

[94] E. Fogarassy, D. Lowndes, J. Narayan, C. White, J. Appl. Phys. **58**, 2167 (1985).

[95] D. Bollmann, G. Neumayer, R. Buchner, K. Haberger, Appl. Surf. Sci. **69**, 249 (1993).

[96] G. Kerrien, J. Boulmer, D. Debarre, D. Bouchier, A. Grouillet, D. Lenoble, Appl. Surf. Sci. **186**, 45 (2002).

[97] G. Bentini, M. Bianconi, L. Correa, R. Nipoti, D. Patti, A. Gasparotto, Appl. Surf. Sci. **36**, 394 (1989).

[98] T. Deutsch, J. Fan, G. Turner, R. Chapman, D. Ehrlich, R. Osgood Jr., Appl. Phys. Lett. **38**, 144 (1981).

[99] A. Esturo-Bretón, M. Ametowobla, C. Carlsson, J. Köhler, J. Werner, *Proc. 21st European Photovoltaic Solar Energy Conference*, edited by H. Palz, H. Ossenbrink, P. Helm (WIP Munich, 2006), 1247.

[100] M. Ametowobla, A. Esturo-Bretón, J. Köhler, J. Werner, *Proc. 31st IEEE Photovolt. Spec. Conf.* (IEEE, Piscatway, 2005), 1277.

[101] M. Ametowobla, J. Köhler, A. Esturo-Bretón, J. Werner, *Proc. 22nd European Photovoltaic Solar Energy Conference*, edited by W. Palz H. Ossenbrink (WIP Munich, 2007), 1403.

[102] C. Carlsson, A. Esturo-Bretón, M. Ametowobla, J. Köhler, J. Werner, *Proc. 21st European Photovoltaic Solar Energy Conference*, edited by W. Palz H. Ossenbrink (WIP Munich, Germany, 2006), 938.

[103] J. Carlsson, C. Köhler J. Werner, *Proc. 17th IEEE Photovolt. Spec. Conf.* (IEEE, Piscatway, 2007), 538.

[104] J. R. Köhler (2007), Private communication.

[105] S. Sze, *Physics of Semiconductor Devices* (Wiley, Inc., 1983).

[106] H. Kodera, Jap. J. Appl. Phys. **2**, 212 (1963).

[107] T. Sameshima, H. Tomita, S. Usui, Jap. J. Appl. Phys. **27**, L1935 (1988).

[108] G. Bentini, M. Bianconi, L. Correra, R. Nipoti, D. Patti, A. Gasparotto, Appl. Surf. Sci. **36**, 394 (1989).

[109] G. Bentini, M. Berti, C. Cohen, A. Drigo, E. Iannitti, D. Probat, J. Siejka, Journal de Physique **C1**, 229 (1982).

[110] A. Esturo-Bretón, M. Ametowobla, C. Carlsson, J. Köhler, J. Werner, *Proc. 20th European Photovoltaic Solar Energy Conference*, edited by H. Ossenbrink (WIP Munich, 2005), 1133.

[111] T. Röder, A. Esturo-Bretón, S. Eisele, C. Carlsson, J. Köhler, J. Werner, *Proc. 23rd European Photovoltaic Solar Energy Conference*, edited by H. Ossenbrink (WIP Munich, 2008), 1133.

[112] G. Bilger, *Präparation und Dotierung von amorphen Silizium durch die Kathodenzerstäubung*, Phd thesis, Universität Stuttgart (1992).

[113] S. Eisele, M. Ametowobla, G. Bilger, J. Köhler, J. Werner, *Proc. 23rd European Photovoltaic Solar Energy Conference*, edited by H. Ossenbrink (WIP Munich, 2008), 1737.

[114] J. Klein, J. Schneider, M. Muske, S. Gall, W. Fuhs, Thin Solid Films **451**, 481 (2004).

[115] V. Deshmukh, H. Webber, D. McCaughan, Appl. Phys. Lett. **39**, 251 (1981).

[116] D. Parker, F. Lin, S. Zhu, D. Zhang, A. Porter, IEEE Trans. El. Dev. **ED-30**, 1322 (1983).

[117] D. Parker, W. Porter, S. Zhu, F. Lin, J. Appl. Phys **53**, 6246 (1982).

[118] H. Seidel, L. Csepregi, A. Heuberger, H. Baumgärtel, J. Electrochem. Soc. **137**, 3612 (1990).

[119] R. Köhler, Appl. Phys. A **58**, 149 (1994).

[120] J. Werner, P. Schalberger, M. Oehme, K. Lyutovich, E. Kasper, Thin Solid Films **50u**, 2006 (2006).

[121] K. Hoh, H. Koyama, K. Uda, Y. Miura, Jap. J. Appl. Phys **19**, L375 (1980).

[122] Y. Mada N. Inoue, Appl. Phys. Lett. **48**, 1205 (1986).

[123] Y. Yatsurugi, N. Akiyama, Y. Endo, J. Electrochem. Soc. **120**, 975 (1973).

[124] M. Berti, L. Donna dalle Rose, A. Drigo, C. Cohen, J. Siejka, B. Bentini, E. Jannitti, Phys. Rev. B **34**, 2346 (1986).

[125] P. Tipler, *Physics* (Trans Tech Publications, Aedermannsdorf, 1987).

[126] K. Thonke, G. Watkins, R. Sauer, Sol. St. Comm. **51**, 127 (1984).

[127] J. Weber, R. Davis, H.-U. Habermeier, W. Sawyer, M. Singh, Appl. Phys. A **41**, 175 (1986).

[128] W. Kürner, R. Sauer, A. Dörnen, K. Thonke, Phys. Rev. B **39**, 13327 (1989).

[129] M. Suezawa, K. Sumino, H. Harada, T. Abe, Jap. J. Appl. Phys. **25**, 859 (1986).

[130] S. Hahn, H. Stein, S. Shatas, F. Ponce, J. Appl. Phys. **72**, 1758 (1992).

[131] W. Götz, G. Pensl, W. Zulehner, Phys. Rev. B **46**, 4312 (1992).

[132] A. Borghesi, B. Pivac, A. Sassella, A. Stella, J. Appl. Phys. **77**, 4169 (1994).

[133] W. Kaiser, P. Keck, C. Lange, Phys. Rev. **101**, 1264 (1956).

[134] H. Hrostowski R. Kaiser, Phys. Rev. **107**, 966 (1957).

[135] H. Stein P. Peercy, *Mat. Res. Soc. Symp. Proc.* (Elsevier Science Publishing Co. Inc., 1983), 229.

[136] M. Allardt (2008), Private communication.

[137] S. Pizzini, M. Guzzi, E. Grilli, G. Borionetti, J. Phys.: Condens. Matter **12**, 10131 (2000).

[138] M. Tajima, A. Kanamori, T. Iitzuka, Jap. J. Appl. Phys. **18**, 1401 (1979).

[139] H. Nakayama, T. Nishino, Y. Hamakawa, Appl. Phys. Lett. **38**, 623 (1981).

[140] D. Karg, G. Pensl, M. Schulz, C. Hässler, W. Koch, Phys. Stat. Sol. (B) **222**, 379 (2000).

[141] C. Hässler, H.-U. Höfs, W. Koch, G. Stollwerck, A. Müller, D. Karg, G. Pensl, Mat. Sci. Eng. **B71**, 39 (2000).

[142] A. Cuevas, P. Basore, M. Giroult-Matlakowski, *Proc. 13th Europ. Photovolt. Sol. En. Conf.* (1995), 337.

[143] E. Schneideröchner, R. Preu, R. Lüdemann, S. Glunz, Progr. Photovolt. **10**, 29 (2002).

[144] F. Granek, M. Hermle, B. Fleischhauer, *Proc. 21st European Photovoltaic Solar Energy Conference*, edited by O. H. (WIP Munich, 2006).

[145] F. Book, B. Raabe, G. Hahn, *Proc. 23rd European Photovoltaic Solar Energy Conference*, edited by W. Palz H. Ossenbrink (WIP Munich, Germany, 2008), 1546.

[146] A. Grohe, T. Wütherich, A. Knorz, J. Nekarda, N. Mingirulli, C. Harmel, R. Preu, S. Glunz, *Proc. 22nd European Photovoltaic Solar Energy Conference*, edited by W. Palz H. Ossenbrink (WIP Munich, Germany, 2007), 1751.

[147] P. Fath, 4th PV Production Equipment Conference, Munich (2009), Photon International.

[148] H. Haverkamp C. Buchner, *A c-Si solar cell technology with selective emitters*, Photovoltaics World (2009).

[149] D. De Ceuster, P. Cousins, D. Rose, *Proc. 22nd European Photovoltaic Solar Energy Conference*, edited by W. Palz H. Ossenbrink (WIP Munich, Germany, 2007), 816.

[150] S. Herrmann, P. Engelhart, A. Merkle, *Proc. 22nd European Photovoltaic Solar Energy Conference*, edited by W. Palz H. Ossenbrink (WIP Munich, Germany, 2007), 970.

[151] S. Kebach, *Herstellung und Charakterisierung von einseitig kontaktierten Solarzellen*, Diploma Thesis (2007), University of Stuttgart.

[152] S. Dauwe, *Low-Temperature Surface Passivation of Crystalline Silicon and its Application to the Rear Side of Solar Cells*, Phd thesis, Universität Hannover (2004).

Curriculum Vitae

Persönliche Angaben

Name	Mawuli Francis Ametowobla
Geburtsdatum	20. April 1978
Geburtsort	Lahn-Gießen

Schulbildung und Zivildienst

1984-1987	Grundschule in Bissingen
1987-1996	Gymnasium Donauwörth
06/1996	Abitur, Gesamtnote 1.3
1996-1997	Zivildienst, Kreiskrankenhaus Donauwörth
1998	Auslandsaufenthalt an der Academía Málaga Plus, Málaga, Spanien

Studium und Promotion

1998-2004	Studium der Elektrotechnik an der Universität Stuttgart
2003-2004	Diplomarbeit, Thema "Kontaktierung und Dotierung von Silizium mit Hilfe von Sprühprozessen"
03/2004	Abschluss Diplom-Ingenieur, Gesamtnote "sehr gut"
2004-2008	Wissenschaftlicher Mitarbeiter am Institut für Physikalische Elektronik, Universität Stuttgart

Berufliche Tätigkeit

seit 2008	Entwicklungsingenieur bei der Manz Automation AG
seit 2009	Gruppenleiter Prozessentwicklung cSi

Danksagung

Die Danksagung in einer Dissertation ist gleichzeitig eine Rückschau auf eine lange Zeit. Mein Dank gilt als erstes Prof. Jürgen Werner, der mich mit einer interessanten Idee für eine Diplomarbeit auf diesen Weg gebracht und durch Höhen und Tiefen der Arbeit immer an ihr Gelingen geglaubt hat. Vor allem danke ich ihm auch für die Geduld, die er aufbrachte, als das "harte" Leben außerhalb des Instituts seinen zeitlichen Tribut forderte und ein geplanter Abgabetermin nach dem anderen obsolet wurde...

Als nächstes möchte ich Jürgen Köhler danken, der mich in die "Laserwelt" eingeführt hat und immer mit Tipps, Tricks und Ideen zur Seite stand. Genau so danke ich Ainhoa Esturo-Bretón, die mich während meiner Diplomarbeit unter ihre Fittiche nahm, mich danach als "Zuwachs" in die Lasergruppe aufnahm und jederzeit ein aufmunterndes "C...!" parat hatte. Caroline Carlsson war die angenehmste Zimmergenossin und Kollegin, die man sich vorstellen kann. Sie war fast immer gut gelaunt (auch wenn ihr gerade die mühselige Arbeit von zwei Wochen vom Tisch gefallen war...) und immer für einen lustigen Spruch zu haben. Später kamen Sebastian Eisele und Tobias Röder zur Lasergruppe dazu, brachten frischen Wind mit und haben die - anfangs manchmal verschlungenen Wege - der Lasergruppe eindrucksvoll zielstrebig fortgeführt. Danke und weiter so, Jungs!

Und noch immer bleiben so viele übrig, ohne deren Hilfe nichts aus dieser Arbeit geworden wäre, darum sei auch gedankt:

- Gerhard Bilger für ungezählte SIMS Messungen, Auswertungen und viele wissenschaftliche und auch unterhaltsame Diskussionen.

- Radovan Kopecek vom ISC in Konstanz, für ECV Messungen.

- Jörg Weber und Matthias Allardt von der Universität Dresden, für FTIR und PL Messungen und Hilfe bei ihrer Interpretation.

- Rolf Weber von der Humboldt Universität Berlin, für Röntgentopographie Messungen.
- Jens Werner vom IHT, fürs Defektätzen.
- Julian Mattheis, fürs Korrekturlesen, für gute Nachbarschaft, viele gute Abende und perfekte Zusammenarbeit beim Wiederbeleben von Kollegen...
- Tobias Röder und Michael Reuter fürs Korrekturlesen und die gute Zusammenarbeit.
- Isabell Kessler und Dr. Christine von Rekowski, dafür, dass sie sich jedes organisatorischen Problems mit einem Lächeln angenommen haben.
- Brigitte Lutz, Leo Bauer und Christiane Köhler, für die tatkräftige Hilfe im Labor.
- Hannes Rostan, fürs Überleben...
- Marc Sämann, Sebastian Eisele, Tobias Röder, Christian Ehling, Michael Reuter, Rainer Merz, für unzählige spannende Tischkickerspiele.
- Dem *ipe* mit allen seinen Mitarbeitern dafür, dass ich mich dort fast wie zuhause fühlen konnte. Ganz besonders dazu beigetragen haben auch zwei Kollegen, die ich noch nicht erwähnt habe: Werner Wille und Klaus Brenner. Ihr beide seid viel zu früh gegangen. Die dankbare Erinnerung an Euch wird bleiben.

Am Ende fehlen noch die wichtigsten Menschen in meinem Leben. Danke meinen Eltern und meiner Schwester für Eure Unterstützung und dafür, dass Ihr Euch mein Klagen darüber, dass es immer noch nicht fertig ist, angehört habt.
Danke, Hanna, für Dein Verständnis.
Danke, Linus, dafür dass Du zu uns auf diese Welt gekommen bist.

Erklärung

Hiermit erkläre ich, dass ich die vorliegende Dissertation "Characterization of a Laser Doping Process for Crystalline Silicon Solar Cells" selbständig verfasst und nur die angegebenen Hilfsmittel verwendet habe.
Stuttgart, den 04.01.2010

Mawuli Ametowobla